Università Statale degli Studi di Milano
Facoltà di Scienze e Tecnologie

Corso di laurea in Fisica

A tailored advanced Free Electron Laser source of coherent and high repetition rate X-rays for linear spectroscopy

Tesi di Laurea di:
Michele OPROMOLLA
Matr. Nr. 901745

Relatore: Vittoria PETRILLO
Correlatore: Luca SERAFINI

Anno Accademico 2017-2018

Contents

Abstract

Free-electron laser (FEL) facilities around the world provide scientists with ultra-short, transversely coherent and intense photon pulses with short wavelengths.
Most FELs work as an amplifier for the spontaneous radiation (SASE), and its stochastic behaviour is imprinted on the photon pulses, resulting in poor temporal coherence and large shot-to-shot fluctuations in wavelength, energy, and longitudinal pulse profile. It has been shown that different seeding schemes can enhance the spectral, temporal and coherence properties of the emitted radiation.

In the framework of the MariX project, an advanced combined Compton/FEL radiation source aimed at delivering ultra-brilliant and ultra-short pulses at high repetition rate in a wide range of energies, the possibility of generating seeded FEL radiation in the hard X-ray range is analyzed. The main project's aim is that of filling the gap in terms of average photon flux and time resolution between synchrotron light sources and current FELs, opening the way to new research applications in the field of linear spectroscopy and not only.
After the determination of an optimized electron beam for the two FEL lines operation, an optimal seeding scheme for the high energy photon line is studied, starting from the High-Gain Harmonic Generation (HGHG) approach. In this scheme, the electron beam energy is modulated by means of an external laser and an electromagnetic undulator. This energy modulation is then converted into a current density modulation which enhances the harmonic content of the electron bunch at the desired wavelength, which is then emitted.

The cascade scheme proposed is the following: we start from coherent radiation at about 13nm from laser high harmonic generation (HHG) in gases. It follows the injection in an undulator segment (first modulator) tuned at this frequency. One of the odd harmonics acts as seed for an undulator with a shorter period (second modulator) and finally a last undulator segment (the radiator) amplifies the harmonics of the radiation produced upstream.
In the present thesis the MariX FEL performances are simulated, some possible seeding schemes are also studied by means of start-to-end simulations and their feasibility is discussed, focusing on the main problems and possible solutions. Future outlooks are given in a final section, including the study of an FEL oscillator as seed to the cascade.

Chapter 1

Introduction

The basic understanding of life requires to study phenomena and processes occurring concurrently at many length and time scales, that need specific tools for investigation and modelization.
Analytical Research Infrastructures (ARIs) based on electron accelerators are at the basis of Photon Science that describes the multidisciplinary implementation of the analysis of matter, extending from the life sciences to materials science and physics [1]. This kind of fine analysis requires light sources at the proper wavelengths producing light pulses of minimal time duration in order to access the proper space and time scales, with the appropriate energy resolution. A worldwide effort in the development of such light sources has been pioneered 50 years ago and still it is in a very rapid expansion. Currently, synchrotron radiation (SR) sources based on low-emittance electron storage rings and Free Electron Lasers, based on linear electron accelerators (Linacs) and self-amplification of spontaneous emission (SASE), are the two main types of X-ray sources supporting the ARIs. Pioneering FEL sources have been operated at Stanford University (LCLS [2]) since 2009 and at Spring-8 (SACLA [3]) since 2011, and novel constructions are underway worldwide. FERMI@Elettra in Trieste [4] operates in the VUV-Soft X range at up to 50 Hz and is the only existing seeded FEL, amplifying a Ti:Sa seed pulse with negligible time jitter and minor pulse-to-pulse intensity fluctuations.

FEL sources are capable to provide extremely brilliant pulses of 10-100 fs duration within the UV-X spectral range, exceeding the peak brilliance of storage rings by more than 9 orders of magnitude, and reaching more than 10^{12} photons per pulse of < 100 fs duration to be used for various applications. For example these pulses can be used in experiments to probe matter in a highly excited state, dominated by non-linear response, or to probe before destroying individual objects, like macromolecules, thus replacing crystallography with single object imaging. FEL-based experiments have been successfully focused on the study of the internal structure or ordering of materials (solids, molecules, atoms), thanks to their compatibility with single pulse detection.

Time resolution of 10-100 fs has revealed itself as a need of fine analysis also in spectroscopy, that requires photon excitation density to remain within the limit of linear response. The understanding of the ground state of complex matter, like materials with high electron correlation, can be achieved through the observation of the competition between transient configurations of excited matter (for example photo-excited by tunable fs laser pulses). This study of metastable states of matter can be ideally performed with ultra-short (order 10 fs) soft and hard X-ray pulses with about 10^8 photons/pulse, used to probe the electronic and magnetic structure after an initial pump has perturbed the ground state. Moreover, spectroscopic probes, suitable to study magnetic and electronic structures, are harder to implement at low repetition rates due to the higher demand in terms of average photon flux on the sample. Currently this time domain is covered by fs laser optical spectroscopy as well as by photoelectric effect spectroscopy as excited by 10-100 fs laser driven High Harmonic Generation (HHG) sources, reaching energies of the order of 0.1 keV and repetition rates of several 100 kHz. Further development of laser based sources is foreseen, but nowadays adequate intensities (number of photons per pulse) and repetition rates (number of pulses per second) can be realized only by electron-accelerator based FELs. Pump probe photoemission experiments of high scientific impact in atomic, molecular, nanoparticle and solid state physics ideally require a source of ultra-short photon pulses (order 10 fs) with about 10^8 photons/pulse to remain in the linear or near-linear response regime that allows spectroscopy to be interpreted within perturbative approaches, and repetition rates as high as possible (MHz range) for collecting adequate statistics in short times. MHz repetition rates are adequate to pump-probe experiments as ultra-short IR or tunable HHG pump sources can be employed to prepare the excited state and microsecond intervals between subsequent experiments are sufficient to reproduce the initial ground state of the sample.

Currently available FEL sources are far from being ideal for spectroscopy, as the number of photons per pulse exceeds by 2-4 orders of magnitude the one compatible with the linear response regime: severe attenuation of the pulses is therefore required for photoemission or X-ray absorption spectroscopy (XAS) and X-ray Magnetic circular dichroism (XMCD) experiments and this wastes an astounding fraction of the operating energy of the FEL. The warm Linacs are limited to few tens of Hz repetition rate, up to 100/120 Hz, which is definitely non ideal for collecting adequate statistics in high resolution spectroscopy. The good performances of the EU-XFEL (2700 micropulses at 4.5 MHz in 10 macropulses per second) are also non ideal: attenuation is needed and the repetition rate of the micropulses is so high that it overruns the present capabilities of detectors and of possible pump-probe set-up operation.

SASE fluctuations are another severe limitation to spectroscopy with FELs at X-rays. True seeding, as successfully done by FERMI, should be ideally extended to X-ray energies. There is clearly the scientific need of a new source capable of pro-

viding 10 fs pulses of 10^8 photons at 1-2 MHz, bridging between the most advanced SR and the current FEL sources. The former are aiming, in the future years, at few-ps pulses at up to 500 MHz (current pulses are in the few tens of ps range), thus 10^8 pulses/s with typically $10^5 - 10^6$ photons/pulse; the latter are yielding 10-100 fs pulses at $10^1 - 10^4$ pulses/s with 10^{12} photons/pulse.
These demanding requests of pulse structure, intensity, repetition rate, reduced jitter and true coherence, able to fill up the evident gap in timing resolution and average photon flux between SR and current FELs, are addressed by conceiving a tailored source based on a seeded FEL driven by a Super Conducting linac, providing $10^8 - 10^{10}$ coherent photons at 2-5 keV till at least 500 kHz.

The present thesis deals with the study and feasibility analysis of such an X-ray FEL source as part of the *Multi-disciplinary Advanced Research Infra-structure for the generation and application of X-rays* (MariX) project in Milan, Italy, a combined FEL/Compton radiation source presently under design at the Milan Expo area with unique unprecedented expected performances of tailored coherent, ultra-high flux, femto-second-class X-rays in a wide range of photon energy spanning from 200eV to 180keV.
The production of coherent radiation in the X-rays range is a very stimulating research field, and it's the main object of the work presented here. In the seeded amplifier configuration, the radiation phase and amplification is not started from the electron shot noise, but is forced by an external coherent source, which enables to reach a higher degree of temporal coherence within a shorter distance. However, direct seeding is not possible in the soft-hard X-rays range due to the lack of a coherent seed at these wavelengths, so that other seeding schemes are analyzed and taken into account. HHG sources have been developed in laboratories as well as in pioneering user facilities, with 100 fs range pulses of 10^7 photons/pulse at some 10^5 pulses/s, but are currently limited at energies below 100 eV. Shorter, sub-fs pulses are generated by HHG, but at kHz repetition rate at most. Higher photon energies have been demonstrated but currently with a low number of photons per pulse, which is unsuitable for fine analysis experiments.
The implementation of High Gain Harmonic Generation (HGHG) multi-stage cascades seeded by harmonics in crystals of an IR laser, realized at SPARC in the optical-UV range [5] and demonstrated at FERMI up to few nm of wavelengths [4], is studied up to the hard X-rays range, that can be also reached with the technique of the EEHG [6]. Partial longitudinal coherence can be obtained in the single spike SASE mode or by means of self-seeding processes [7]. FEL oscillators or regenerative amplifier [8] have been proposed as direct source of X-rays (XFELO) [9, 10] or as source of seed for a subsequent cascade [11], but the operational scenario proposed so far with electrons at several GeVs sets strict limits on this option.

The MariX complex will deliver these pulses to a multi-instrument suite (beamlines) for research in many diverse science domains and applications. Besides tailoring the FEL and ICS sources for science, the environment of a science campus in the outskirts of Milano will also play a role in obtaining an overall original configuration where all key operational buildings for the source services and experimental hall are located next to each other, thanks to the two-way operation of the superconducting Linac accelerator.

In the following, an outline of the thesis' chapters is presented: Chapter 2 describes the most significant and successfully tested schemes for seeding an FEL source as well as their benefits and limits, particularly regarding their use in the hard X-rays range. Space requirements and other physical reasons led to the proposal of an High Gain Harmonic Generation (HGHG) scheme for the generation of coherent soft and hard X-rays, which is analyzed in a more quantitative way in a section of this chapter, together with some theory on electron bunching and its use for enhancing the radiation amplification
Chapter 3 discusses the MariX project hosting the FEL source as final radiator, including its innovative layout and its basic working points. The last section is dedicated to the design and main characteristics of the FEL X-ray source. Then, Chapter 4 focuses on the start-to-end FEL simulations and their main results, with the machine's tolerance and performance studies related to its working points. This chapter also deals with the study of an optimal scheme for seeding the FEL at MariX, and the results supporting the proposed configuration. A discussion on future outlooks and upgrades, including new possible seeding schemes and FEL configurations is given in the last section.
Finally, Chapter 5 summarizes the most significant results obtained in Chapter 4 and gives the concluding remarks.

As an appendix, the interested reader can find an introduction on the scientific development towards modern radiation sources and their importance in scientific research, a theoretical description about FELs, including the low and high gain regimes and 3D effects (focusing on important differences between SASE and seeded FELs), and a last part about the FEL code GENESIS 1.3 used for the simulations.

Chapter 2

Free Electron Laser Seeding Schemes

2.1 Basic Scaling laws

This section summarizes the most important scaling laws regarding the basic Free Electron Laser (FEL) mechanism, which are derived in Appendix B.
The FEL radiation mechanism (see section B.1.1 for more details) is basically the synchrotron radiation emission by accelerated relativistic charged particles due to the transverse periodic magnetic field $B_y(z, x = 0, y = 0) = B_0 \cos(k_w z)$ of bending magnets or undulators. The induced transverse sinusoidal oscillation (wiggle) makes the electrons emitting synchrotron radiation at each bend of their trajectory, allowing an energy exchange with the copropagating electric field of the radiation. Depending on the phase of this exchange, electrons gain or loose energy for the benefit of the radiation field. By reducing the mean longitudinal velocity $\beta_z = 1 - \frac{1+a_w^2}{2\gamma^2}$ of the bunch[1], the transverse undulations thereby enhance the rate at which the emitted radiation slips past the electrons in the bunch. If the radiation slips one optical wavelength per undulator wavelength (if the optical wavelength λ is such that $\lambda = \lambda_w(1 - \beta_z)$), then interference takes place and the electrons will oscillate in phase with the field, continually losing energy. The rate of the electron energy loss grows as the field grows. The energy modulation induced by the radiation field is then converted into a spatial modulation of the electrons, the *electron bunching*, with the periodicity of the radiation wavelength [12]. The electrons are then concentrated in regions where the transfer efficiency from particle to field is maximized: in these regions, the radiation becomes coherently amplified.

[1]For a given electron beam $\gamma = 1/\sqrt{1-\beta^2} = E/mc^2$ is the Lorentz factor, with the normalized velocity $\beta = v/c$, the beam energy E, the electron mass m and the speed of light c.
The undulator parameter, considering the case of planar undulator, is defined as $a_w = eB_0/\sqrt{2}mck_w$, where e represents the electron charge, B_0 the undulator peak magnetic field and $k_w = 2\pi/\lambda_w$ the undulator wave number, with the period of longitudinal variation of the on-axis magnetic field λ_w. In practical units $a_w = 6.57x10^{-2}\lambda_w(mm)B(T)$.

2.1.1 Fundamental frequency

For a single electron of given energy, the resonance condition for the wavelength of the emitted radiation, in a planar undulator, is

$$\lambda = \frac{\lambda_w}{2\gamma^2}(1 + a_w^2) \ . \tag{2.1}$$

The efficiency of energy transfer and the gain of the process are summarized by the FEL or Pierce parameter

$$\rho = \frac{1}{4\pi\gamma}\sqrt[3]{2\pi\frac{J}{I_A}\left(JJ\lambda_w a_w\right)^2} \tag{2.2}$$

where $JJ(\chi) = J_0(\chi) - J_1(\chi)$ is the planar undulator Bessel correction factor, of argument $\chi = \frac{a_w^2}{4+2a_w^2}$ and $I_A \sim 17$kA the Alven current.

The current density J is given by

$$J\left[\frac{A}{m^2}\right] = \frac{I[A]}{2\pi\sigma_x[m]\sigma_y[m]}$$

where σ_x and σ_y are the rms transverse dimensions of the electron beam (Eq. (B.84), $\Sigma_b \sim \pi\sigma_x\sigma_y$ is the beam cross section), and the current I[A] can, in turn, be expressed in terms of the bunch rms (root mean squared) time duration $\sigma_\tau[s]$ and of the bunch charge Q as

$$I[A] = \frac{Q[C]}{\sqrt{2\pi}\sigma_\tau[s]}$$

The gain length, determining the FEL Self Amplified Spontaneous Emission (SASE) growth rate, can be expressed in terms of ρ as follows:

$$L_g = \frac{\lambda_w}{4\pi\sqrt{3}\rho} \ . \tag{2.3}$$

Following the model described in Appendix B.4, the power growth is fitted by the logistic equation, which can be written in the simplified form:

$$P(z) = \frac{P_0}{9}\frac{\exp(z/L_g)}{1 + \frac{P_0}{9P_{sat}}\exp(z/L_g)} \tag{2.4}$$

where P_0 is the input seed power, z the longitudinal undulator coordinate and $P_{sat} \cong \sqrt{2}\rho P_{beam}$ the power at saturation, where $P_{beam} = mc^2\gamma I_p$ is the power carried by the electron beam of peak current I_p.
The saturation length, namely the length necessary to reach the power P_{sat}, is

$$L_{sat} = 1.066 L_g ln\left(\frac{9P_{sat}}{P_0}\right) \ . \tag{2.5}$$

The Pierce parameter gives an estimate of both the power at saturation and the natural bandwidth of the FEL

$$\frac{\Delta\omega}{\omega} \cong \rho \tag{2.6}$$

as well as of the energy conversion and FEL process efficiency (Eq. (B.68) in Appendix B). The gain deterioration due to non ideal electron beam qualities (non negligible energy spread and emittance), can be embedded in the previous formulas as discussed in Appendix B.5.

The number of photons emitted per pulse can be estimated as

$$N_{ph}/pulse = \frac{P_{sat}}{\hbar\omega}\sigma_{ph} \tag{2.7}$$

where σ_{ph} is the photon pulse time duration.

2.1.2 Radiation on harmonics

An FEL process, similar to the one described in Appendix B and summarized by the scaling laws of the previous section, is also valid for the harmonics of the fundamental wavelength (2.1)

$$\lambda_n = \frac{\lambda_w}{2\gamma^2 n}(1 + a_w^2) \tag{2.8}$$

where for a planar undulator n is an odd integer. Planar undulators in fact allow a resonant on-axis FEL interaction with odd harmonics of the fundamental resonant field, so that the FEL equations can thus be extended to the odd harmonics in this case. The power growth along the longitudinal coordinate becomes [12]

$$P_n(z) = \Lambda_n(z) + \Pi_n(z) \tag{2.9}$$

where the first term represents the linear part of the coherent harmonic lasing, namely

$$\Lambda_n(z) = P_{0,n}A_n(z)$$

with $A_n(z) \propto P(z) \sim e^{z/L_g}$ as in Eq. (2.4), while the non-linear harmonics contribution is provided by

$$\Pi_n(z) \propto \frac{\exp\left(\frac{nz}{L_g}\right)}{1 + \frac{1}{P_{sat,n}}\left[\exp\left(\frac{nz}{L_g}\right) - 1\right]} \; .$$

The Pierce parameter of the harmonics is

$$\rho_n = \rho\left[\frac{JJ_n}{JJ_1}\right]^{\frac{2}{3}} \rightarrow L_{g,n} = \frac{\lambda_w}{4\pi\sqrt{3}\rho_n} \tag{2.10}$$

with $JJ_n = J_{\frac{n-1}{2}}(n\chi) - J_{\frac{n+1}{2}}(n\chi)$. The harmonics' power at saturation is

$$P_{sat,n} = \frac{1}{\sqrt{n}}\left(\frac{JJ_n}{nJJ}\right)^2 P_{sat} \; .$$

The number of photons emitted at the n^{th} harmonic is given by

$$N_{ph,n} = \frac{P_{sat,n}}{n\hbar\omega}\sigma_{ph} = \chi_n N_{ph} \text{ with } \chi_n = \frac{1}{n\sqrt{n}}\left(\frac{JJ_n}{nJJ}\right)^2 \frac{\sigma_{ph,n}}{\sigma_{ph}} . \tag{2.11}$$

The parameter χ_n represents the harmonic conversion efficiency (which for the third harmonic is around 0.1%).
The radiated spectrum is composed by a series of square sinc functions, centered on odd harmonics [13]. Referring to the case of a single electron, the relative linewidth of the harmonics is given by $\Delta\lambda/\lambda_n = 1/(nN_w)$ where N_w represents the number of undulator magnetic periods. The emission is narrow in the frequency domain, even if undulator line broadening may result from the electron beam energy spread, size and divergence [13].

2.2 SASE vs Seeding

One of the biggest advantages of FELs compared to Synchrotron based light sources is their degree of longitudinal coherence, which is achieved by phasing the emitting electrons.
The conventional self-amplified spontaneous emission (SASE) FEL radiation mode presents an ample and solid experimental validation in all the domain of wavelengths from optical [14] to X-rays [2]. SASE FELs operated down to Angstrom regime open up new horizons for photon science (see section A.2.2), and harmonic lasing is a possible way to extend their operating range further. FELs working in this regime, where the signal starts from the electron beam noise and the emission between different trains of bunches is not correlated, feature quite high transverse but low longitudinal coherence: in the first part of the amplification many transverse modes are excited, but by the end of the exponential growth only the highest growth rate mode dominates; as regards the longitudinal coherence, the SASE radiation exhibits a sequence of M uncorrelated temporal spikes, whose mutual distance is $2\pi L_c$ where the cooperation or coherence length is defined as

$$L_c = \frac{\lambda}{2\pi\rho} \tag{2.12}$$

and

$$M = \frac{L_{beam}}{2\pi L_c} . \tag{2.13}$$

Also the frequency spectrum of the emitted radiation corresponds to the white noise associated to the initial electron random distribution, filtered by the FEL gain bandwidth.
A simple way to improve the longitudinal coherence of a SASE FEL can be to create electron bunches short enough ($L_{beam} < 2\pi L_c$) to confine all electron that contribute to lasing within one cooperation length [15]. This technique leads to one single longitudinal mode in the temporal distribution of the FEL radiation, as well as to a

single spiked spectral distribution (”single spike regime”). However, radiation power and pulse energy are limited by the practical limits for the charge density of the electron bunches. Another important disadvantage of single-spike operation is the 100% shot-to-shot fluctuations of the photon pulse energy due to the stochastic behaviour of the SASE radiation and this method only offers longitudinal coherence [15]. This regime also permits operation at low charge, with good control of emittance and energy spread. Therefore, a substantial coherence in each single radiation shot is achieved, but with very low shot to shot stability. Due to the slippage, saturation is reached quite early. This can be compensated by chirping the electron beam and tapering the undulator.
For a general bunch, the average number of spikes in the spectrum ('longitudinal modes') is given by the number M of Eq. (2.2) which can also be written as

$$M = \frac{T_{bunch}}{\tau_c} \tag{2.14}$$

where the coherence time is a function of the spectral bandwidth σ_ω [16]

$$\begin{aligned} \tau_c &= \int \left(\exp\left(-\frac{\sigma_\omega(z)^2 t^2}{2}) \right) \right)^2 \mathrm{d}t \\ &\approx \frac{\sqrt{\pi}}{\sigma_\omega(z)} \; . \end{aligned} \tag{2.15}$$

The SASE mode, where the electron beam is directly coupled to the undulator, can be upgraded with various other modes that improve the quality of the radiation or increase the radiation frequency.
There are two basic mechanism able to create coherent microbunching at harmonic frequencies in FELs: nonlinear harmonic generation (NLHG) and harmonic lasing.
The former method is driven by the fundamental interaction in the vicinity of saturation, when the electron density modulation becomes nonlinear. For a planar undulator, this harmonic microbunching regards the odd harmonics generated in the forward direction. Since even harmonics can only be emitted off-axis for aligned electron beams, their coherent radiation is largely suppressed: for example, the 2nd harmonic content is expected to be $\sim 10^{-4}$ compared to the fundamental power level. The microbunching of the electron beam on the 3rd harmonics can also be exploited by tuning the last part of the undulator on the third harmonics. The relative spectral bandwidth of the harmonic radiation is similar to that of the fundamental, but harmonics intensity is tipically at a level of a percent and weaker of the fundamental frequency intensity and is more strongly subjected to shot-to-shot fluctuations [17–21].

Harmonic lasing was first proposed and experimentally demonstrated for FEL oscillators [22–24]. It is an FEL instability developing independently from lasing at the fundamental wavelength, whose advantages over NLHG might include much higher power, better stability, smaller bandwidth and no necessity in filters, provided that

lasing at the fundamental frequency is suppressed.
In this method, the SASE amplifier is interrupted when the bunching is maximum, at roughly 80% of saturation, and the bunched beam current containing large Fourier components at the harmonics of the SASE fundamental frequency is injected into a radiator (called afterburner undulator) tuned at one of the harmonics.
Other possibilities to suppress the fundamental harmonic without affecting the harmonic lasing use phase shifters between undulator modules (iSASE) [25, 26], or a spectral filter in a intra-undulator chicane (similar to the one used in the self seeding scheme described in section 2.5).

To improve the limited degree of coherence typical of SASE FELs as single-pass FELs, several techniques were developed and applied in the experimental research [13, 15, 27–30]. The purpose of seeding for FELs is threefold [15]: improving the longitudinal coherence of a SASE FEL configuration (and simultaneously increasing its brilliance), synchronizing the FEL signal with an external signal for pump-probe experiments and improving the stability of the FEL power from shot-to-shot by introducing a well-defined seed signal. The seeded operation allows to obtain a nearly fully coherent radiation beam in both spatial and temporal domains, whose temporal coherence can be of the order of tens of fs. Nevertheless, as pointed out in next section, the limitation for direct seeding to go towards the X-ray range comes from the wavelength of the seed laser.

High gain FELs operated in seeded mode are often referred to as 5^{th} generation light sources; next sections will address different seeding techniques.
In a seeding configuration the FEL acts as an amplifier of an initial seed, increasing the emitted peak power to approximately the same value characteristic of SASE saturation: an external laser pulse is injected and superimposed to the electron beam, providing an efficient bunching of the electrons and imprinting the coherence of the seed to the electron modulation, which can then radiate coherently in the following sections of undulator at the undulator resonance and its higher order harmonics [31].
"Direct seeding" refers to any methods where the seed signal has the same wavelength as the resonance wavelength (see Eq. (2.1)) of the FEL, with a power level above the shot noise power but below the FEL saturation power.
Wavelength tuning of a seeded FEL can be achieved by simultaneously changing the seed wavelength and the undulator gap or by applying a chirp on the modulated electron bunch. FEL pulse spectral and temporal distributions are cleaned from the typical SASE multiple spikes by the seed itself, but may be altered by the FEL saturation process. The radiation field indeed moves faster and slips over the electron beam along the undulator and enters earlier in saturation, and the so-called slippage length L_s is the path difference at the end of the undulator.
Depending on the seed pulse duration with respect to the slippage length, different regimes can occur [13]. When $L_s \ll L_{pulse}$, the intensity at the peak of the pulse suddenly drops at saturation, leading to a pulse splitting regime [13, 32]. The local heating of the electrons induced by saturation leads to the separation of the pulse in

two branches. This regime is deeply used for pump-probe two-color experiments. When $L_s \sim L_{pulse}$, the FEL dynamics enters a strongly nonlinear superradiant regime, with pulse duration narrowing and simultaneous emission of harmonics up to the 11th order, as observed at SPARC [33].

Any seeding source needs to fulfill few important conditions: first, it has to exhibit the same tuning ability of the FEL itself; second, it has to overcome the shot noise power of the electron beam, cause seeding with a power below the power level of the spontaneous radiation would result in SASE performance [15, 27].
To estimate the relation between the electron shot noise at the resonant frequency, source for the SASE FEL process, and the intensity of the associated input field to be effective, it is convenient to focus on the small signal-regime [13, 27] in the case of a long bunch where the FEL dynamics is well described by the integral equation [34]

$$\begin{aligned}\frac{\mathrm{d}}{\mathrm{d}\tau}a = -2\pi g_0 b_1 e^{-i\nu_0\tau} + i\pi g_0 \int_0^{\tau} \tau' e^{-i\nu_0\tau'} a(\tau-\tau')\mathrm{d}\tau' \\ + i\pi g_0 b_2 e^{-2i\nu_0\tau} \int_0^{\tau} \tau' e^{i\nu_0\tau'} a^*(\tau-\tau')\mathrm{d}\tau'\end{aligned} \tag{2.16}$$

in terms of the dimensionless Colson field strength (B.44) (see the last part of Appendix B.3 for more details about its derivation), also including the presence of prebunching and shot noise. Eq. (2.16) describes the FEL instability starting from a seed $a(0) \neq 0$ or from a modulated beam $b_{1,2} \neq 0$ (with b_2 accounting for prebunched beams injected in a radiator with a pre-existing laser field 2). Electron bunching coefficient is generally indicated as b_n for any integer n, and is essentially the Fourier coefficient of the electron beam density distribution $\rho_e(\theta)$

$$\rho_e(\theta) = \frac{1}{n_e}\sum_{i=1}^{n_e}\delta(\theta-\theta_i) \rightarrow b_n = \frac{1}{\lambda}\int_0^{\lambda}\rho_e(\theta)e^{-i2\pi n\theta/\lambda}\mathrm{d}\theta \tag{2.17}$$

where θ is the longitudinal coordinate along the electron bunch, and $\rho_e(\theta)$ the normalized electron beam longitudinal current density, with λ the resonant wavelength. In section B.4 of the Appendix B, the different evolution of the FEL interaction initiated by an input seed a_0 (see section B.4.1) or by a pre-bunched beam $b_1 \neq 0$ (see section B.4.2) is described. Starting from a pre-bunched beam, and assuming $a(0) = 0$, the coherent spontaneous emission power growth is quadratic (Eq. (B.77)) with the longitudinal position, while it becomes exponential (Eq. (B.78)) when the seed strength gets larger than the bunching term. The equivalent seed intensity associated to a given beam prebunching (see Eq. (B.79)) is obtained by setting the magnitude of the field associated to the exponentially growing root, namely $a(\tau) = a_0/3\exp[-i/2(1+i\sqrt{3})\tau]$, equal to the threshold value of the field at the transition between quadratic and exponential growth $a(\tau_{th}) = -2(\pi g_0)^{2/3}b_1$ (Eq. (B.79)) corresponding to the position $z_{th} = \sqrt{3}L_g$

$$|a_{0_{eq}}| = 6(\pi g_0)^{2/3}e^{-\frac{\sqrt{3}}{2}}|b_1| \rightarrow I_{0_{eq}} = 9e^{-\sqrt{3}}\frac{P_{beam}}{\sigma_{beam}}\rho|b_1|^2 \ . \tag{2.18}$$

The minimum necessary seed intensity is derived by calculating the bunching coefficient b_1 for a discrete number n_e of electrons at the random longitudinal positions θ_i, characterized by the longitudinal distribution (2.17). The corresponding bunching coefficient is

$$b_1 = \frac{1}{n_e}\sum_{i=1}^{n_e} e^{-i2\pi n\theta_i/\lambda} \simeq O\left(\frac{1}{\sqrt{n_e}}\right) . \tag{2.19}$$

The microscopic electron distribution is not a periodic function of the longitudinal coordinate, so that the average in the Fourier coefficient (2.19) has to be calculated over a length larger than one period of λ_0, this way accounting for the interference of the fields from electrons separated by more than a wavelength. The ideal electron distribution in Eq. (2.17) has a white-noise spectral distribution, while a real FEL amplifier has a relative amplification bandwidth of the order of ρ and only the noise in this spectral range is amplified. We need to calculate the fluctuations in a frequency range $\Delta\omega \sim \rho\omega$, considering a portion of the beam of the order of the cooperation length (2.12) .
The number of electrons in one cooperation length is

$$n_{ec} = I_{peak} L_c / c . \tag{2.20}$$

The shot noise intensity is estimated by combining Eqs. (2.17, 2.19 and 2.20) as

$$I_{sn} \sim \omega_0 \rho^2 \gamma m c^2 / \Sigma_b \tag{2.21}$$

being proportional to the square of the FEL parameter and growing linearly with the resonant frequency and the electron beam energy [13, 15]. Given Eq. (2.2) and considering typical values for the main parameters, it is possible to evaluate the shot noise power in terms of the emission wavelength. As a reference, considering beam parameters with the target in the VUV at $\lambda = 20$nm one has a shot noise intensity of the order of $I_{sn} \sim 10^6 W/cm^2$, while in the hard X-regime at $\lambda = 0.1$nm one has $I_{sn} \sim 10^9 W/cm^2$ [27].
It is reasonable to desire a contrast ratio of $10 - 10^2$ between the seed and the background noise [13], or even higher in other cases (see next section for example). This requirement puts a limit on the shortest wavelength: while seeding sources tipically have lower efficiency in terms of output power at shorter wavelengths, the shot noise power grows as Eq. (2.21) making seeding a non trivial problem in the hard-X spectral range.
Moreover, the 1D theory (see Appendix B.4) puts a limit on how much seed power can be coupled to the exponentially growing mode: for seeded FELs only 1/9th of the power is amplified and it requires about two gain lengths (see Eq. (2.3)) till any change in the radiation power becomes measurable, overcoming the lethargy regime of a seeded FEL [15, 27, 35] (see Figure B.6 in Appendix B). The coupling efficiency is further reduced in the 3D model because some mode matching between the seed mode and the fundamental FEL eigenmode is required [15]: an optimum case would have about 50% coupling efficiency. For an improved signal-to-noise ratio, the seeding power has to exceed the shot noise power by a wide range (10-100 times).

Even the bandwidths have to be matched. If the seed signal has a bandwidth larger than the FEL bandwidth (for instance by seeding with a pulse length shorter than the coherence length of the FEL) only a fraction is picked up and amplified; in this case the peak brightness of the FEL output is not improved with respect to a SASE FEL because the entire FEL bandwidth is excited [15].

Depending on the source of the external seed, there is a variety of names to direct seeding. There are three common and successfully demonstrated approaches [13,15, 16,27,36]: direct seeding with High Harmonic Generation (HHG), induced bunching with High-Gain Harmonic Generation (HGHG) or Echo-Enabled Harmonic Generation (EEHG) as well as self-seeding. Towards shorter wavelength, High Harmonic Generation (HHG) in noble gases is the most promising seed source and, for this reason, is analyzed in more details in next section.

2.3 Seeding with High Harmonic Generation in gas

Typical lasers used to seed FELs are the Ti:Sa with second (SHG) or third (THG) harmonic generation, thanks to their characteristics in terms of energy and pulse duration (fs-class). However these lasers do not give radiation below 120 nm of wavelength. For shorter wavelengths of operation, in the soft and hard-X range, a direct seeding configuration is not possible.

The limitation of direct seeding for going towards the X-ray range comes from the wavelength of the seed laser, restricted to UV for commercial tunable laser sources. The lack of a sufficiently high-power, narrow-bandwidth laser below 200nm has driven scientists to look at other possible seeds and advanced schemes [27], and the developments in femtosecond laser technology are making the direct seeding of a FEL amplifier in the VUV-EUV a viable solution [13]. One possibility is to seed the FEL amplifier with a high-order harmonic generation (HHG) laser source.
The generation of harmonics in gas is one of the promising methods to generate ultrashort pulses of coherent radiation in the XUV (30-300 eV) - soft X (300-3000 eV) region of the spectrum [12,13,16,27,37,38]. The high-order harmonics result from the strong nonlinear polarization induced on rare gas atoms, such as Ar, Xe, Ne, and He, by the focused intense electromagnetic field of a "pump" laser at $10^{14} - 10^{15} W/\text{cm}^2$, typically a titanium-sapphire laser system with the main resonance at 800nm and pulse energy ranging from a few to hundreds of mJ. The most important characteristics of the production of a seed pulse in a high-harmonics generation target are qualitatively given by the three-step semi-classical model by Corkum et al. [39–41] illustrated in Figure 2.1.

As the external electromagnetic field intensity becomes comparable to the Coulomb potential V_c of the atom (thus to its internal static field) in the interaction region

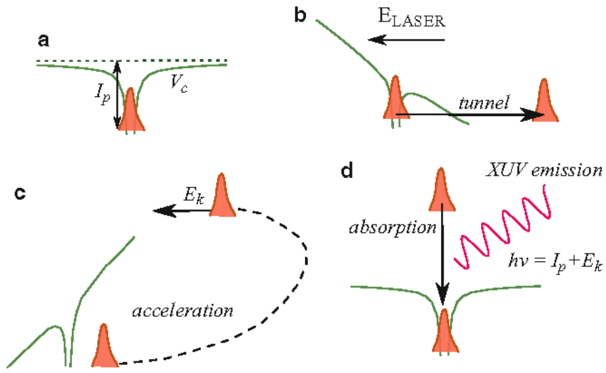

Figure 2.1: Sketch of the atom interaction with a strong e.m. field, according to the three-step model: a) initial state of the gas atom b) electron tunnelling c) gain of kinetic energy d) electron absorption and photon emission. I_p is the gas medium ionization potential

close to the laser focus, the laser field bends the atomic potential (Figure 2.1a) and electrons are stripped off from the atom by tunnel ionization (Figure 2.1b). The ejected free electrons, far from the core, are then accelerated in the external laser electric field and gain a kinetic energy E_k (Figure 2.1c). Those which are driven back close to the core can either be scattered or recombine to the ground state emitting a burst of XUV photons every half-optical cycle, with an energy defined by the kinetic energy of the electrons, much higher than the drive laser but phase locked (Figure 2.1d) [16, 27].

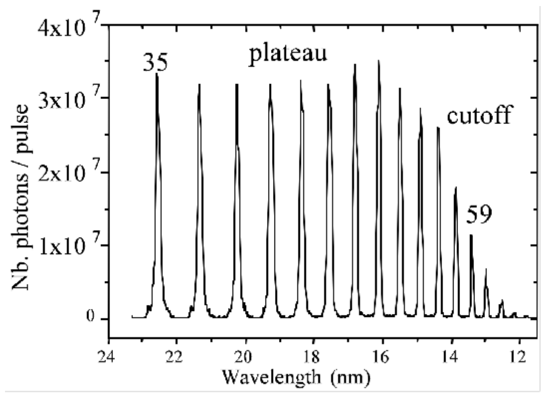

Figure 2.2: Typical harmonics spectrum produced in a Neon jet, from [31]

A typical spectrum of harmonics generated in gas (see Figure 2.2) consists of a train of XUV bursts, superposition of the high-order odd harmonics of the fundamental laser frequency, separated by twice the fundamental energy and reaching into the VUV region. The characteristic distribution of intensities is almost constant with harmonic order in the "plateau" region where, depending on the generating gas, the conversion efficiency varies in the range $10^{-4} - 10^{-7}$. For higher orders, the conversion efficiency decreases rapidly in the "cutoff" region [13, 31]. The cut-off energy giving the upper spectral limit is $E_{cutoff} = I_p + 3.2U_p$ where I_p is the gas ionization energy, $U_p \propto I_{pump}\lambda^2_{pump}$ is the ponderomotive potential, with I_{pump} the focused pump intensity and 3.2 the maximum kinetic energy E_k [13, 31].

Light gases, such as Ne and He, present a high ionization potential, allowing short wavelengths to be radiated. According to the "cut-off law", the lighter is the gas (the higher is the ionization energy and the laser intensity which can be applied without ionizing the atom) the higher is the cut-off energy [13].
A complete quantum mechanical approach to HHG allows to predict phase information of the harmonic radiation, which depends on the drive laser phase and the phase of the recombining electron. Besides, the extracted electron can follow two different paths, named "short" and "long" path and characterized by the time spent by the electron in the continuum of energy states, to recombine with the parent ion. For the short path, the time is shorter than half the optical period, while for the long one it is of the order of the laser period [13]. The superposition of their contributions generates two attosecond pulses for each half optical cycle of the driving field. In order to emit the n^{th} harmonic, constructive interference between the drive laser field and the radiation emitted in the HHG process needs to take place [15, 16]. The coherent interference of the radiation emitted by different atoms leads to different phase-matching conditions. The phase difference is defined by the dispersion of the medium and the electrons, the focusing geometry and the single-atom phases. The laser intensity, divergence and waist size as well as the geometry of the gas target, its type and pressure can be exploited to control the phase matching [15, 16].

To ensure fully coherent beams, one needs to control the contributions of the electrons' trajectories [16], basically changing the relative position of the gas jet with respect to the laser focus. Placing the gas jet right after the laser focus [42] one can select the contribution of the short path, leading to one XUV pulse for each half-cycle of the laser. With the gas jet before the laser focus, the long path contribution increases leading to a more complex time-structure of the generated radiation field. Another solution is to separate the harmonic production process and the phase matching process by alternatingly adding passive areas and harmonic generation areas (one half period long) driven by one single laser, using a so-called quasi-phase matched target [16].
For direct seeding, one would optimize an HHG source in terms of the highest possible photon number on the desired harmonic and a bandwidth as small as possible because many users request small-bandwidth, Fourier-limited coherent photon pulses. In addition, the divergence has to be kept small enough (1 to 10mrad with respect to the axis of laser propagation) to overlap the harmonic radiation with the FEL electrons in the undulator for a sufficiently long distance. The harmonics waist w_{harm} and divergence div_{harm} are related to the laser's one according to $w_{harm} = q^{-1/2}w_{las}$,$\mathrm{div}_{harm} = q\mathrm{div}_{las}$ where $n = 2q + 1$ is the harmonic number [31].
Long transport lines should be avoided, since transport, as well as matching lines, are critical in the case of HHG sources: losses transporting and matching the beam

to the electrons were estimated at 50% [13]; besides, another order of magnitude in loss is added because of the matching between the bandwidth of harmonics generated in gas (10^{-2}) and of the FEL (10^{-3}) in the spectral domain. For these reasons, the contrast ratio between seed and shot noise intensity levels should be of the order of $10^3 - 10^4$.

The implementation of HHG seeding in FELs involves the use of several chambers, whose role is to separate the region hosting the gas interaction region from the high vacuum required by the accelerator.
High order harmonics are linearly polarized sources between 100 and 3 nm, with a high degree of temporal and spatial coherence [13, 31] emitting < 100fs pulses with up to few kHz repetition rate. The HHG process preserves the transverse coherence properties of the drive laser though the ongoing ionization of the noble gas by electrons, which are not recombined, makes the phase matching between the drive laser and the emitted photons difficult. In reality only short pulses of a few tens of fs can be achieved with enough spectral purity in the harmonics to be suitable for seeding [16]. The first theoretical work on this field was done by Li-Hua Yu et al. [43–45] and a demonstration in the UV was shown by the same group at Brookhaven National Lab (BNL) [46]. The first attempts to seed an FEL amplifier with HHG radiation were done in the UV at SCSS[2] [13, 38, 47, 48] and at SPARC [49–52] with a seeding between 260 and 89 nm. An experiment at the Spring-8 SCCS facility successfully used HHG radiation as an FEL seed down to 61nm wavelength [53], the 13th harmonic of the original Ti:Sa drive laser. A more challenging 38-nm wavelength HHG seeding experiment at the FLASH facility[3] has shown some FEL amplification but at power levels only an order of magnitude above the incoherent, larger-bandwidth spontaneous emission [54]. HHG was also considered for SPARXINO [55], an extension of SPARC towards shorter wavelengths. However it became apparent that towards shorter wavelength the HHG sources need to deliver much more spectral power to overcome the shot noise limit of the electron beam. Seed pulses with sufficient power are only available at low repetition rates, mainly due to the unavailability of suited laser systems in terms of power output and possibility to be synchronized to external sources [15]. The low peak-power levels of present-day HHG sources for $\lambda \leq 10$nm and the significant technological challenges of transporting and focusing such short-wavelength radiation suggest the difficulty of having a robust HHG source at wavelengths at or below the carbon K-edge ($\lambda \sim 4 - 2$nm) with the needed MW-power levels to dominate SASE at an undulator entrance [**?**, 27].

[2]They used a Ti:Sa pump laser having 800nm wavelength, 20mJ energy at 10Hz focused on a 9mm-long Xenon gas cell, generating 3rd-21st harmonics. They used the 5th harmonic (160nm) as seed. Amplification is observed when the seed energy is larger than 1.4pJ, but the spiky SASE structure in the spectrum is suppressed only when the seed energy is about one order of magnitude larger. That energy corresponds to a seed peak power about one order of magnitude larger than the shot noise.

[3]The seed wavelength of 38nm is the 21st harmonic of the 800nm Ti:Sa drive laser, generated by injecting up to 50mJ of infrared light in a gas-filled capillary. This is the shortes wavelength where harmonics generated in gas have been amplified in a single-pass FEL.

HHG sources are in fact inherently inefficient, and suitable techniques to boost the XUV emission to the required peak powers are required. In this respect, methods with corrugated capillaries coupled to the drive laser [56, 57], the use of two-colour laser pulses [58] and of mixed gases as target [30] or interference of counter propagating laser pulses [59], as well as the spatial and temporal optimization of the drive laser by suitable optical shapers can reduce the limitation by the phase mismatch, while longer drive wavelength can reach harmonics at shorter wavelengths [16].

Figure 2.3 shows the energy per pulse obtained with the HHG technique as a function of the wavelength [12]. The peak power can be estimated by considering that the harmonics are generated with laser pulse durations of ∼50 fs. The dashed line represents the beam shot-noise-associated energy (multiplied by 10^4), obtained by assuming the same pulse duration and constant a_w, period and ρ. According to Eq. (2.20), the FEL shot noise power rapidly grows with decreasing wavelength, thus an ever higher seed energy is required. The numerical factor 10^4 is the result of an estimate of the losses due to transport optics to the undulator (x5), the matching with the electron beam (x2), the frequency matching (x10) and the contrast ratio (x 10^2).

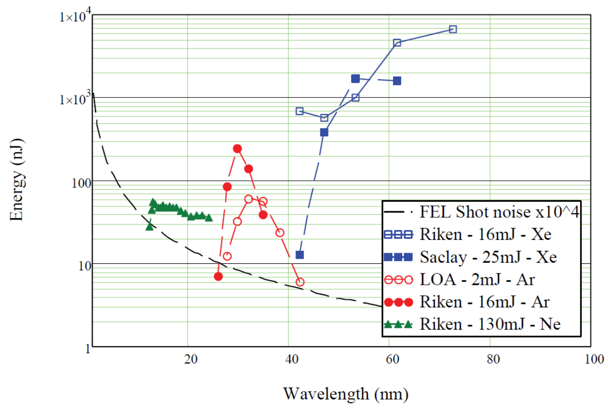

Figure 2.3: Energy per pulse (typical laser pulse duration 50 fs) obtained from HHG sources vs. wavelength compared to electron beam shot noise energy x 10^4 (black dashed line) [12, 60]

Only few experiments have been done up to now with HHG sources as seeding for FEL. Some generation of HHG at 3 nm [61] have been done but with insufficient value of energy per pulse for FEL experiments. In order to reach 3 nm and less, a cascade scheme should be provided starting from a seed wavelength as close as possible to the desired one.

The possibility of having radiation at around 13 nm, starting from a Ti:Sa laser at 800 nm, emerges from various studies. Two methods, in particular, can be considered: the first [62] allows to have radiation at 13.11 nm or 12.69 nm, corresponding to H61 and H63 respectively, the second one [63] is based on the two-color HHG technique and provides a 12.9 nm seed corresponding to H62. Results of such studies are reported in Figure 2.4.

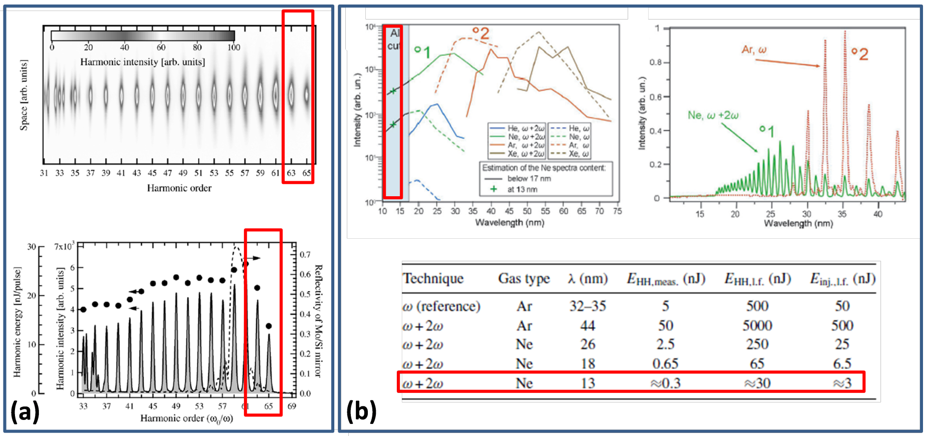

Figure 2.4: Experimental data of the production of HHG from a 800nm Ti:Sa laser. Plots refers to two different techniques: the first one [62] (a) generates the odd harmonics and gives 13.11 nm at H61 or 12.69 nm at H63 obtained in Ne gas; the second (b) [63] generates also the even harmonics by using the two-color HHG and gives 12.9 nm on H62 again in Ne gas. Both methods allow to reach energy of 3-5 nJ in few fs

The energy levels in both schemes are around 3-5 nJ and the time lengths of the single radiation pulse are tens of femtoseconds. These values, if reproducible, could be of interest to assess the feasibility of a seeding scheme with HHG on MariX (see Chapter 4 for the results).
Next section will address one important method to amplify an external seed different from the direct seeding and amplification of an external source.

2.4 High-Gain Harmonic Generation

As an alternative single-pass FEL approach to SASE and instead of directly amplifying an external seed in an FEL, harmonic upshift schemes capable to transfer the coherence properties of a (relatively) long-wavelength laser seed to a much shorter-wavelength FEL output pulse were proposed [38, 64, 65]. The upshift process (see Figure 2.5 in next page) starts with the seed interacting with the electron beam in a short undulator (called the "modulator") to induce a temporally periodic energy modulation on the beam. The electrons then pass through a chromatic dispersion section (generally a four-dipole chicane) that converts the energy modulation into a current density modulation, whose fundamental wavelength is that of the input seed laser but also having significant harmonic content at shorter wavelengths. At this point the electron beam enters a much longer undulator (the "radiator") with period λ_w whose magnetic strength a_w is tuned such that the kinematic FEL resonant

wavelength Eq. (2.1) is identical to that of a specific higher harmonic n of the seed laser (third or fifth tipically) [27].
In the high-gain harmonic generation scheme (HGHG) of Yu [43, 65], the radiator is many exponential gain lengths long, and coherent radiation initiated by the microbunching at $\lambda_R = \lambda_{seed}/n$ grows reaching saturation levels.

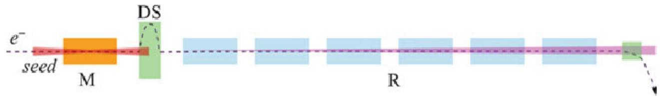

Figure 2.5: Schematic layout of an FEL in the high-gain harmonic generation configuration. The electron beam is energy modulated in the modulator (M) by an external seed laser. The energy modulation is converted into a density modulation by the dispersive section (DS) and the harmonic component resonant in the radiator (R) is amplified, from [27]

Proof-of-principle experiments, conducted at Brookhaven, convincingly demonstrated the HGHG process at infrared [43] and UV wavelengths [65] employing harmonic upshift ratios of three. More recent demonstrations at the Synchrotron Trieste FERMI FEL-1 facility [4], the only existing seeded FEL user facility, have extended the output wavelength range down to the XUV regime with power saturation for harmonic ratios $n \geq 13$. At FERMI, the seed laser is based on an optical parametric amplifier tunable in the range 230-260nm and delivering pulses of few tens of mJ. All these experiments have shown the advantages of HGHG seeding over the SASE configuration, such as improved output pulse energy and central wavelength stability, reduced spectral line-width, and a larger longitudinal coherence length that can be a large fraction of the seed duration. Besides providing the intensity amd spatial coherence of SASE FELs, the output radiation features temporal coherence and the saturation length is reduced, leading to a more compact system [27]. In fact, high-peak power output pulses of a few femtoseconds are possible with chirped pulse amplification (CPA) [16].
Moreover, tunability can be obtained by means of frequency mixing techniques applied on the pump laser or combining a chirp on both electron beam and laser pulse [31]. The HGHG output radiation has a Fourier transform limited spectral bandwidth, a single phase determined by the seed laser and its properties are a map of the characteristics of the high-quality seed laser.

Nonetheless, the HGHG approach have some limitations, basically related to its sensitivity to the electron beam's energy spread [15]. The electron beams incoherent energy spread σ_E at the modulator together with the chromatic dispersion in the radiator limits the maximum practical harmonic upshift ratio n for which reasonable microbunching values can be maintained over multiple radiators in a single-stage, HGHG configuration [27]. To the lowest order, the magnitude of σ_E scales directly with the longitudinal bunch compression and thus the electron beam current. Since both FEL gain and power are sensitive to the electron beam and undulator parameters (as current, σ_E, a_w), for a given situation there will be a maximum n for which the HGHG output power can approach reasonably large saturation levels. Beyond this maximum, the saturated power generally decreases exponentially with increasing n. In order to circumvent this limitation and to extend the useful operating range of HGHG to short wavelengths, multistage harmonic cascades in which the microbunching (and associated harmonic content) or output radiation from one stage is used to seed a following stage whose radiator is resonant at an integral harmonic of the previous one, were proposed. Thus, in a two-stage example, if the harmonic upshift ratio in the first stage is n_1 and that of the second stage is n_2, the final output wavelength is $\lambda_{seed}/(n_1 n_2)$. In its simplest form, a two-stage cascade can be configured by splitting the radiator of a nominally one-stage cascade into two consecutive sections, with the first resonant at λ_{seed}/n_1 and the second at $\lambda_{seed}/(n_1 n_2)$. This is the so-called "whole-bunch" approach [27] that, in principle, allows the entire electron beam pulse to take part in the FEL interaction, presuming the first stage was seeded by a sufficiently long laser pulse. Experimentally, two-stage, whole-bunch harmonic cascades have been studied at the Frascati SPARC facility, starting with an HHG source as a seed [5, 48, 66] and FERMI [67] for which the net harmonic upshift value $n_1 n_2$ has been as large as 65.

In the whole-bunch approach, the main problem is the accumulated energy spread for each stage, which can degrade the performance of the final radiator. In addition the shot noise is amplified with the harmonic conversion and even a strong input signal can get lost in the noise of the final radiator. The FEL gain and final saturation power in the second stage are significantly degraded by the large energy spread induced by both the laser seed and the FEL gain interaction in the first-stage modulator and radiator, respectively [27]. There is a short temporal region toward the head side of the seeded portion of the electron beam where electrons not strongly energy modulated by the seed can be reached by the radiation "slipping" forward. While this region can produce quite high peak power in the form of ultrashort pulses, the radiation here preserves neither the temporal nor spectral properties of the external seed, resulting in a degradation of the longitudinal coherence.

Coherence can be preserved in the "fresh-bunch" two-stage cascading scheme [27,68–70] where the initial radiation seed duration τ_{seed} is much shorter than the electron beam pulse duration and the second stage is separated from the first by a strong chicane that delays the electron beam by an amount $\tau_d \geq \tau_{seed}$. As shown in Figure 2.6, this temporal delay permits radiation from the first stage (which can be run into full FEL saturation if desired) to seed a "virgin" electron beam region that has been unaffected by FEL interaction in the first stage (with the exception of low-level SASE growth) and for which the energy spread has not been heated by the previous light-electron interaction.

As shown in Figure 2.6 (see next page) [27], the FEL is composed of two stages, operating with a single electron bunch, with the first stage seeded by an external laser (seed), modulating the electrons in modulator M1 and generating the seed (seed 2)

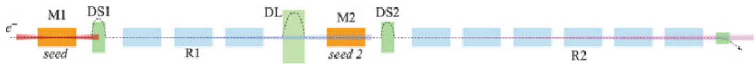

Figure 2.6: Schematic layout of an FEL in the fresh-bunch high-gain harmonic generation configuration. The first stage (M1-DS1-R1) is analogous to the high-gain harmonic generation scheme shown in Fig. 2.2. The second stage (M2-DS2-R2) is based on the same concept, but the seed is the radiation produced in the first stage. The two stages are separated by a delay line (DL) which lengthens the electron path with respect to the radiation (straight) path allowing to seed a "fresh" portion of the electron beam

for the second stage, in the first-stage radiator R1. The two stages are separated by the delay line DL, which retards by few hundreds of fs the electron bunch relative to the seed2 radiation, exposing a fresh part of it to the new seed in the second-stage modulator. The result is that in the final radiator harmonic conversion factors up to 56 of the first stage seed can be generated, providing a significant shortening of the final wavelength.
In principle, this process can be repeated several times in a cascade configuration with a multiplicative upshifting of the final photon energy from that of the initial seed. In practice, however, the number of stages and final wavelength is believed to be limited by either phase noise amplification problems, insufficient FEL gain at very short wavelengths where the resonant undulator strength parameter a_w is significantly less than 1, or a finite electron beam pulse length that can support only a moderate number of individual stages. Furthermore, this fresh bunch cascade requires that the entire process operates only locally with a slice of the bunch moving slowly from the tail to the head of the bunch for each cascading step. Thus the amount of electrons contributing to lasing in the final radiator is small and the overall pulse energy is smaller than in SASE operation. This penalty gets larger the more cascading stages are needed, and so far only two stage cascades have been operated successfully.
HGHG made tremendous progress towards shorter wavelength down to 5nm with a fresh bunch technique in a cascade configuration. Shorter wavelengths seem feasible, but they operate with long bunches and lower current as compared to SASE FELs at the same wavelength. The fresh-bunch injection technique has been demonstrated at SDUV-FEL [13] and at FERMI [71], where conversion factors corresponding to the 65th harmonic of the seed were reached.

2.4.1 HGHG theory

In this section we extend the simple formalism introduced in the case of a FEL amplifier (see appendix B) to the case of a FEL operating in a high-gain harmonic generation configuration.
The emission at higher harmonics of the resonant wavelength during the FEL interaction is a direct consequence of the periodic modulation of the electron beam

at the emission wavelength [27]. As it will be clarified in this section, the emission mechanism is an interplay between harmonic bunching, gain and saturation.

As anticipated, due to the difficulty to reach a ratio of 10^3 between the seed intensity and the shot noise equivalent intensity in the hard-X regime, a successful strategy is that of seeding the FEL in a more accessible spectral range and then exploit the higher harmonic bunching generation process to extend this modulation to shorter wavelengths.
Assuming a linearly polarized laser, the saturation intensity in a planar undulator can be defined as

$$I_{s,mod} = \frac{1}{2g_{0,mod}N_{mod}}\frac{P_{beam}}{\sigma_{beam}} \tag{2.22}$$

where $g_{0,mod}$ and N_{mod} are, respectively, the coupling coefficient (see Eq. (B.46)) and the number of periods of the modulator. The interaction with the seed of intensity I_L induces the initial energy modulation $\Delta\gamma$, depending on the laser power and transverse size, as well as on the undulator length and strength.

$$\frac{\Delta\gamma}{\gamma} = \frac{1}{\sqrt{2}N_{mod}}\sqrt{\frac{I_L}{I_{s,mod}}} \ . \tag{2.23}$$

The beam then transverses a dispersive chicane where the path length $\Delta\zeta$ is inversely proportional to the particles energy and proportional to the dispersion R_{56}

$$\Delta\zeta = R_{56}\frac{\Delta\gamma}{\gamma} \ . \tag{2.24}$$

We assume a Gaussian initial electron energy distribution $\propto \exp(-\gamma^2/2\sigma_\gamma^2)$, independent of the longitudinal direction. The harmonic current generated from the HGHG process can be characterized by calculating the bunching factor at a certain harmonic n of the seeding laser [27]. After the dispersion, the bunching factor at the n^{th} harmonic, resulting from the energy modulation $\Delta\gamma$ and the dispersion R_{56}, can be expressed as [27, 72]

$$b_n = \exp\left[-\frac{1}{2}\left(\frac{2\pi n}{\lambda_L}\right)^2\left(\frac{\sigma_\gamma}{\gamma}\right)^2 R_{56}^2\right] J_n\left(\frac{2\pi n}{\lambda_L}\frac{\Delta\gamma}{\gamma}R_{56}\right) \tag{2.25}$$

where λ_L is the seed wavelength, which is also the resonant wavelength in the modulator, with $\lambda_0 = \lambda_L/n$ the resonance in the amplifier. Eq. (2.24) is derived considering a Gaussian energy spread distribution with standard deviation σ_γ, an infinitely long laser and electron beam, thus in the limit $L_{beam} \gg \lambda_L$, and using Eq. (B.24).
The decaying exponential function in the first term accounts for the effect of the pre-existing beam energy spread that becomes more critical at high harmonic conversion orders. The Bessel function of the first kind appearing in the second term is maximized for a specific value of its argument $X_M = \frac{2\pi n}{\lambda_L}\frac{\Delta\gamma}{\gamma}R_{56}$. When

$$\frac{1}{\lambda_L}\frac{\Delta\gamma}{\gamma}R_{56} \simeq \frac{X_M(n)}{2\pi n} \tag{2.26}$$

the bunching coefficient at the n^{th} harmonic, at the entrance of the final amplifier, is maximum. Assuming that we tune the dispersion to maximize the bunching factor, we may write it as a function of the harmonic number n and of the ratio between the induced modulation and the intrinsic energy spread. The condition (2.25) at a given n draws a hyperbole in the space $(\Delta\gamma, R_{56})$. Thus, for a given seed wavelength and harmonic conversion factor, the lower is the energy modulation $\Delta\gamma$ the larger has to be the dispersion R_{56}.
On one hand, the presence of R_{56} in the decaying exponential imposes a low value of the dispersion when the initial energy spread is large. On the other hand, an increase of the energy spread required to induce the density modulation will affect the exponential growth in the final amplifier, according to the gain/saturation power scaling relations. For this reason the optimum condition is generally the one where the induced energy spread is the minimum required to generate "sufficient" bunching [27]. This qualitative assertion can be turned into a quantitative calculation by combining the induced bunching in Eq. (2.24) with the scaling relations of the exponential growth

$$P(z) = P_{th}\left[\frac{\frac{1}{3}\left(\frac{z}{L_g}\right)^2}{1+\frac{1}{3}\left(\frac{z}{L_g}\right)^2} + \frac{\frac{1}{2}\mathrm{exp}\left[\frac{z}{L_g}-\sqrt{3}\right]}{1+\frac{P_{th}}{2P^*_{sat}}\mathrm{exp}\left[\frac{z}{L_g}-\sqrt{3}\right]}\right] \tag{2.27}$$

with $P_{sat} \sim 1.6\rho P_{beam}$.

In the following analysis, we assume not to be limited by the seed laser input power and the value of the dispersion at the exit of the dispersive section, which is generally true when a single-stage high-gain harmonic generation FEL is seeded at visible/UV wavelengths [27]. The efficient energy extraction is obtained when saturation is reached. We may therefore impose the condition that the amplification leads to reach the power ΓP_{sat}, at the end of the amplifier (the condition with $\Gamma = 1$ is reached only asymptotically at $z \to \infty$). Inverting Eq. (2.26) we obtain the bunching factor required to reach the power ΓP_{sat}

$$|b_n|^2 = \frac{\Gamma}{0.8}\left[\frac{\frac{1}{3}(z/L_g)^2}{1+\frac{1}{3}(z/L_g)^2} + \frac{\frac{1}{2}\mathrm{exp}\left[z/L_g-\sqrt{3}\right]}{1+\frac{P_{th}}{2P^*_{sat}}\mathrm{exp}\left[z/L_g-\sqrt{3}\right]}\right]^{-1} . \tag{2.28}$$

Replacing z with the undulator length L_w and considering the 3D beam quality effects (see section B.5), we obtain an identity representing an implicit equation for $|b_1|^2$ which should be solved numerically [27]. A simplified solution is obtained by suppressing the saturation effect in the second term of Eq. (2.27)

$$|b_n|^2 \sim B(L_w, L_{g,3d}) = \frac{\Gamma}{0.8}\left[\frac{\frac{1}{3}(L_w/L_{g,3d})^2}{1+\frac{1}{3}(L_w/L_{g,3d})^2} + \frac{1}{2}\mathrm{exp}\left[L_w/L_{g,3d}-\sqrt{3}\right]\right]^{-1} . \tag{2.29}$$

The function $B(L_w, L_{g,3d})$ is plotted in Figure 2.7 (see next page) as a function of $L_w/L_{g,3d}$, which shows that the presence of the bunching allows to reach saturation

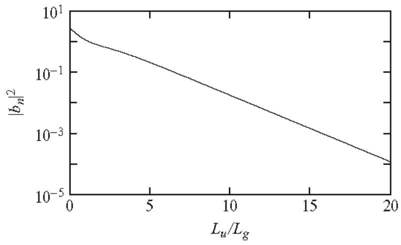

Figure 2.7: Bunching factor required to reach the power ΓP_{fin} (with $\Gamma = 0.5$) as a function of the undulator length (in gain length units), from [27]

even with a very short undulator, only few gain lengths long. The bunching factor (2.7) cannot exceed the unity by definition, and in general its maximum at saturation is of the order of ~ 0.7. From Figure 2.7 it can also be noted that about two gain lengths are always required to reach the saturation power even starting with such a large bunching factor [27]. On the other side, with an undulator length $L_w \gg 20L_g$ the bunching factor becomes comparable to that associated to the electron beam shot noise, and the seed is not effective any more in preparing the pre-bunched beam, with the conclusion that the FEL will operate in SASE.

At a given undulator length, the bunching factor required for saturation (2.28) depends on the FEL gain length $L_{g,3d}$, and the first step to generate a bunched beam is indeed that of inducing a sinusoidal energy modulation of amplitude $\Delta\gamma$ [27]. By so doing, we are also inducing an r.m.s. energy spread $\Delta\gamma/\sqrt{2}$ that will affect the exponential growth in the final amplifier, so that the effective energy spread after modulation will be

$$\sigma_\gamma^{tot}(\sigma_\gamma, \Delta\gamma) = \sqrt{\sigma_\gamma^2 + \frac{\Delta\gamma^2}{2}} \ . \tag{2.30}$$

Assuming another time to tune the dispersion after the modulator to maximize the bunching (2.24) with the longitudinal periodicity $\lambda_0 = \lambda_L/n$, we may write the bunching factor b_n in terms of the harmonic number n and of the ratio between the induced modulation and the intrinsic energy spread

$$b_n\left(n, \frac{\sigma_\gamma}{\Delta\gamma}\right) = \exp\left[-\frac{1}{2}\left(\frac{\sigma_\gamma}{\Delta\gamma}\right)^2 X_M^2(n)\right] J_n\left(X_M(n)\right) \tag{2.31}$$

and the condition for saturation can be written in the form

$$b_n\left(n, \frac{\sigma_\gamma}{\Delta\gamma}\right) = B(n, L_w, L_{g,3d}(\sigma_\gamma^{tot})) \tag{2.32}$$

having the dependence of the gain length on the total energy spread (2.29). This equation can be solved numerically to find the minimum induced energy spread required to reach saturation or, in case saturation cannot be reached because $L_w < 2L_g$, the maximum possible achievable bunching factor [27].

In general saturation is intended as the condition where the power growth is suppressed by secondary effects (see section B.4.1). Given the assumption that we are not limited by the maximum seed power in the modulator, saturation as the one due to the interaction with the field resonant at λ_L/n is always reached.

As suggested in Ref. [27], by plotting the minimum necessary energy spread and the best bunching factor as a function of the harmonic order, one sees that the higher is the harmonic order, the larger is the required energy modulation. The transition between the condition where the bunching factor is large enough to reach saturation at the end of the final amplifier, and the region where the increased gain length due to the shorter wavelength and the higher induced energy spread prevents for reaching saturation may be obtained by calculating the expected output power. Taking as example a seed ultraviolet wavelength, in the region where saturation is reached, the power decreases slowly with the harmonic order, according to the increase of the induced energy spread and reduced FEL parameter. At larger harmonic orders, the power decays faster because saturation is not reached, and any increase of the gain length leads to an exponential decay of the output power.

2.4.2 Seeding by electron beam manipulation

A coherent bunching at the resonant wavelength can be used to seed the FEL. As already pointed out earlier about HGHG cascades, the limiting factor is the induced energy modulation $\Delta\gamma$. In the beginning of the FEL the beam will emit coherently and the power will grow linearly till the FEL amplification process starts after a few gain lengths. The induced bunching must be significantly above the shot noise level [15].
The maximum bunching at the nth harmonic is given by $b_n = \exp(-(n\sigma_\gamma/\Delta\gamma)^2/2)$ and drops quickly when the energy modulation gets smaller than the product of intrinsic energy spread σ_γ and harmonic number [15]. Therefore high harmonic conversions require large energy modulations.

On the other hand the final energy spread still has to fulfill the requirement $\sigma_\gamma/\gamma_0 \ll \rho$, where ρ is the FEL parameter (2.2). If the condition is violated the beam will emit partially coherently in the radiator but will not drive the FEL to saturation.
It follows the need to operate these FELs with a much smaller energy spread than comparable SASE FELs and therefore a restricted use of laser heater to preserve the beam transport from the electron source to the undulator, including acceleration and compression [15]. The required degree of energy modulation can be supplied either directly by a high power seed laser or a FEL process in the modulator, which is stopped at the optimum energy level.

2.5 Echo-enabled Harmonic Generation

Echo-enabled harmonic generation (EEHG) was first proposed by G. Stupakov [28, 36] in 2009 as a means to overcome the limitations in the standard HGHG scheme posed by incoherent energy spread[4] in reaching extremely high harmonic numbers ($n > 100$) for generation of soft X-ray radiation when starting from the radiation from an external, ultraviolet seed laser. It is a more complex configuration which relies upon multiple seed lasers, dispersive sections, and modulator and radiator undulator sections to first produce a coherent "shearing" of the longitudinal phase space followed by subsequent modulation that, via an echo-like effect, leads to a coherent density bunching that far exceeds the incoherent shot-noise background [27].

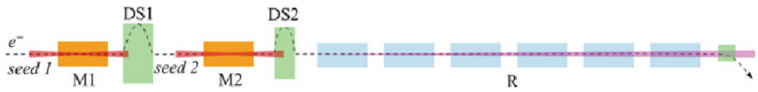

Figure 2.8: Schematic layout of an FEL in the echo-enabled harmonic generation configuration. The scheme consists in a double modulation dispersion stages (M1-DS1-M2-DS2) generating the density modulation at the desired wavelength via a harmonic frequency mixing of the two fields seed 1 and seed 2

At the beginning, a strong seed laser (seed 1) at wavelength λ_1 together with a short modulator induces a moderate ($\Delta\gamma \sim 0.5\sigma_\gamma$), coherent energy modulation on the input electron beam. The dispersive section that follows is sufficiently strong such that $R_{56}\frac{\sigma_\gamma}{\gamma} \gg \lambda_1$, thus shearing the longitudinal phase space and, at a given phase, leading to multiple, alternating narrow bands of large and small density as a function of the energy. The purpose of the first part of the EEHG configuration is to over-compress the energy modulation well beyond maximum bunching with a strong magnetic chicane, rather than optimizing its harmonic content as in HGHG [27]. The second part is the same of an HGHG configured FEL, generating a current spike for each band: the electron beam passes into a second modulator section where it interacts with a second seed laser (whose wavelength λ_2 may or may not equal λ_1) producing new energy modulation of amplitude $\Delta\gamma_2 \sim \sigma_\gamma$ on top of the sheared bands produced in the first section. A second chromatic dispersion is then tuned in strength to rotate these ripples by approximately $\pi/2$ in longitudinal phase. The resultant phase space is rich in harmonic content and, for appropriate choices of seed laser and dispersion section strength, can be tuned to produce an echo effect whose maximum bunching appears at a net harmonic $n \gg 1$ relative to the initial seed wavelength (see Figure 2.8).

[4]In contrast to HGHG scheme that for high harmonic number n has the coherent bunching fraction b_n decaying exponentially as n^2 presuming a Gaussian distribution for the incoherent energy spread, EEHG has b_n decaying only as $n^{1/3}$ in the absence of other effects such as incoherent intrabeam scattering.

To achieve maximum bunching, the current spikes of all energy bands need to be spaced at the final radiation wavelength to add up coherently.

The advantage of the EEHG compared to the HGHG is that the first stage artificially reduces the intrinsic energy spread per band due to the strong overcompression, which allows much higher harmonic conversion in the HGHG stage at the cost of a slight increase in the energy spread [6, 15].
In theory it is possible to achieve very high harmonics with a bunching efficiency of up to $b_n = 0.39/n^{1/3}$ [73]. Experimentally, the scheme has been investigated and confirmed from the optical to vacuum ultraviolet regions ($\lambda \sim 160$nm) at harmonic numbers as high as 15 [74–77]. It still remains to be shown that another order of magnitude in harmonic number is possible in the EEHG approach [27]; if so, this would permit reaching the soft X-ray region at $\sim$ 1nm from an original seed laser operating at $\lambda \sim 200$nm. Its potential for achieving very high numbers makes it an attractive alternative to HGHG methods, despite its intrinsic and complex coupling of two energy modulation and two chicane strengths.
The limiting factor is the ability to preserve the energy bands throughout the seeding line and avoiding any blurring effects. There are two sources of degradation [15]: the quantum fluctuation in the emission of photons of the incoherent synchrotron and undulator radiation, and intra-beam scattering While the first can be mitigated with gentle bending angles and long chicanes, the latter requires a layout as compact as possible. Both limits the practical use of EEHG for wavelengths exceeding $1nm$.

2.6 Self-seeding

All the previous methods require an external signal synchronized to the beam arrival time at the undulator location [16]. To avoid shots with no overlap, the stability of the jitter in the seed signal and the beam arrival time needs to be less than the bunch length. Therefore most externally seeded FELs foresee a lower current to relax the arrival tolerance. As a result the FEL parameter and the power at saturation are reduced. In addition the lower FEL bandwidth restricts the amount of energy modulation of the seeding schemes reducing the ability to scale to very short wavelength in the 1nm range [15].

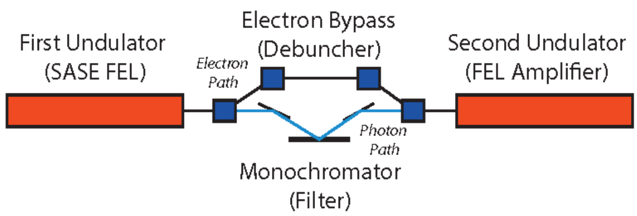

Figure 2.9: Schematic layout for a self-seeding configuration, from [15]

If the requirement for an externally locked FEL pulse is given up, the seed signal can be derived from the same bunch in a two stage configuration [7] (see Figure 2.9). The first stage of the self-seeding configuration operates as a SASE FEL but stops before saturation. In this way the beam preserves the ability to amplify an external signal to full saturation. Following the SASE FEL, the electron beam and radiation field are separated and the radiation is filtered by a monochromator which transmits only a narrow frequency band, confining the radiation in a small spectral bandwidth. The filtered signal is then recombined with the electron beam and injected into the second stage of the FEL, operating as an FEL amplifier. The electron bypass has two purposes [15, 16]: primarily, to match the arrival time of the beam with the monochromatized signal and, secondarily, to remove the induced bunching by the momentum compaction factor of the chicane.

Although the process is internally synchronized, it is not stabilized to an external device, such as a pump-probe laser for example. In addition the intensity fluctuations of the FEL radiation increase cause, by selecting a single spike of the SASE spectrum, the amplification process in the second undulator starts with a huge power fluctuation of the initial radiation. The advantage of this technique is that it produces a single-mode FEL radiation pulse and therefore a significantly increased peak brilliance [15].

The initial idea was proposed for the soft X-ray range by Feldhaus et al. [78] and a technical design report on the possible implementation at FLASH was finished in 2003 [16, 79]. It had the conceptual difficulties that the delay in the photon path way would require a long electron bypass line, where the transport needs to be controlled by a lot of quadrupole and sextuple magnets to preserve the electron beam properties, and was not realized.
For the hard X-ray regime, a novel concept was proposed by Saldin et al. [80] using features in the transmission around the stop band of a Bragg reflection [15]. The transition between total Bragg reflection to almost full transmission has frequency components which are significantly delayed by the crystal. The electron bunch is delayed and overlaps with the trailing signal, which is the interference of the two edge frequencies of the stop band. For photon energies around 8keV the seed signal has still a large amplitude well above the shot noise level. The attractive feature of this method is that the overall delay is of the order of a few tens of fs and that a small chicane can easily be integrated in the undulator line.

The method has been successfully demonstrated at LCLS [81, 82]. A narrowing of the FEL bandwidth by a factor 50 has been measured though the system has become inherently sensitive to the jitter in the electron beam energy, dominating the 100% intensity fluctuation by the missing overlap between the central FEL wavelength and the fixed seed wavelength of the diamond crystal of the Bragg reflector from shot to shot [16].
One inherent problem with Bragg and the similar Laue diffraction is that the delayed part of the transmitted field, which is seeding the second stage, exhibits a transverse

shift in the position due to the effective index of diffraction around the Bragg stop band [15]. This effect is mitigated for near perpendicular incident angles. Therefore the Bragg diffraction has to be optimized for the different wavelengths, using various planes of the crystal lattice. Recently a more compact design of a soft X-ray self-seeding chicane was found with a length less than 4m [83].

A narrow-bandwidth filter of the self-seeding schemes stretches the short SASE spikes with a coherence length typically smaller than the bunch length to a coherence length much longer than the bunch length so that in the second stage a well-defined radiation phase is spread over the entire bunch. This effect can also be achieved if the slippage is increased to cover the entire bunch. In SASE FELs the slippage is one radiation wavelength per undulator period and the characteristic cooperation length gets shorter for shorter wavelength λ assuming an overall constant gain length L_g. There are several methods proposed [84] to artificially increase the slippage per gain length by either breaking up the undulator and interleaving the modules with small chicanes delaying the bunch or by operating on a sub-harmonic of the FEL, where the slippage is increased by the harmonic number.
All methods reduce the FEL bandwidth up to a point where the bunch length is limiting the spectral width. At this point these methods are equivalent to self-seeding methods except that they avoid filters intercepting the radiation [15]. These are attractive alternatives if the heat load on the monochromator, mirrors or crystal is an issue. Similar to these slippage enhancing methods is the feedback of a fraction of the FEL signal to the succeeding bunch in a high repetition machine. The slippage is accumulated over many turns, defining the regenerative amplifier FEL (RAFEL) [85].

The record for the shortest wavelength was done at LCLS at a wavelength of $1.5\mathring{A}$ with self-seeding [16]. No apparent limitations occur in self-seeding schemes, which can be extrapolated to very short wavelength in the $\mathring{A}$ regime, assuming a sufficient filter exists to clean up the spectrum. The electron beam parameters are the same as for SASE operation and an increase in the FEL brilliance is achieved [15].

Chapter 3

MariX project

This Chapter gives an overview of the design project hosting the seeded X-FEL in object. MariX is a multi-purpose infrastructure constituted by two different X-ray sources exploiting different sections of the accelerator chain: an Inverse Compton Scattering source (ICS) and a Free-Electron Laser (FEL) with properties that contribute to define the next generation X-ray sources tailored to linear ultrafast spectroscopy and imaging.

The conceived radiation source represents a new generation of X-ray sources, bridging between the so called 3rd generation, represented by Synchrotron light sources, and 4th generation based on Free Electron Lasers (a brief history of light sources from SR sources to FELs is given in section A.1 of Appendix A). In fact, MariX multiple scientific mission will be pursued by marrying these two cutting-edge techniques for ultra-high brilliance X-ray generation into a single machine. The use of Super-Conducting Linear Accelerators (SC-Linacs) and advanced photoinjectors able to deliver in Continuous-Wave mode (CW) high brightness FEL-grade electron beams, and the technology of Fabry-Prot optical cavities and fiber lasers to sustain MW-class laser beams will allow MariX to generate ultrabright, coherent ultrashort photon pulses in CW at very high repetition rate (in the $1-100$MHz range) through its associated X-ray radiators.
The FEL (discussed in section 3.5) will produce photon pulses of energy between 200 eV to 8 keV at 1-2 MHz, and intense X-ray beams of energy up to 180 keV will be generated by the ICS section at up to 100 MHz.

3.1 Machine Layout

The concept of a novel combination of accelerators and laser sources, capable of serving the ambitious scientific mission was developed, whilst being compatible with the constraints imposed by real estate availability and sustainable construction and operation costs. The compactness of the design of accelerator and undulators (less than 500 m) reduces the overall size of the complex allowing integration in highly urbanized areas or university campuses. On the contrary, the X-ray conventional FEL accelerators in operation (as EuXFEL [86]) or under construction (as LCLS-II [87]) are few km long, with key services and experimental halls at the opposite ends (see Figure 3.1).

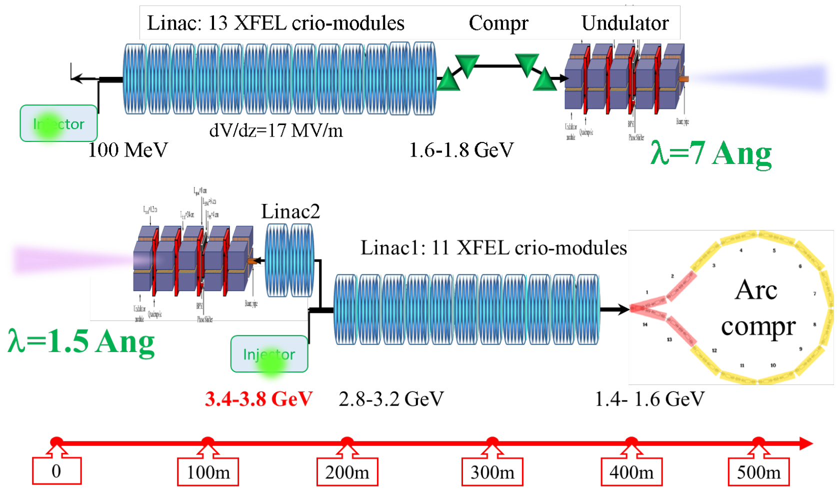

Figure 3.1: Conventional layout of an X-ray FEL accelerator (on top) and MariX layout (at the bottom)

Furthermore, most operational FELs are injected by warm Linacs and support at maximum 100 Hz operation. MariX ultrahigh flux and compact construction come from the use of SC-Linacs supporting the CW mode. By exploiting the specific capability of the SC Radiofrequency cavities of accelerating in both directions, the electron beam can double its energy after being re-injected into the accelerator itself.

The innovative MariX layout, developed directly from Beam Dynamics simulation results and site constraints, is illustrated in Figure 3.2 (see next page).
The MariX project is split in two main parts, named BriXS and MariX itself, working in series and sharing a common acceleration line. The early electron beam acceleration section of MariX includes an energy recovery scheme based on a modified folded push-pull CW-SC twin Linac ensemble (ERL1 and ERL2). The system allows to handle very large beam powers (in the MW range) by smartly recovering most of the active power and reducing significantly its impact on electrical power consumption and radio-protection issues inherent with GeV-class high average current electron beams (just about one hundred kW active power dissipation/consumption). It is then exploited for a Bright and Compact X-ray Source (BriXS), depicted in the enlarged box at the bottom of Figure 3.2 and delivering a twin CW 100MHz 100MeV electron beam at the collision points of ICS for scattering the photons of optical laser pulses in two specular Fabry-Prot cavities (marked as FP1 and FP2 in the bottom part of Figure 3.2).

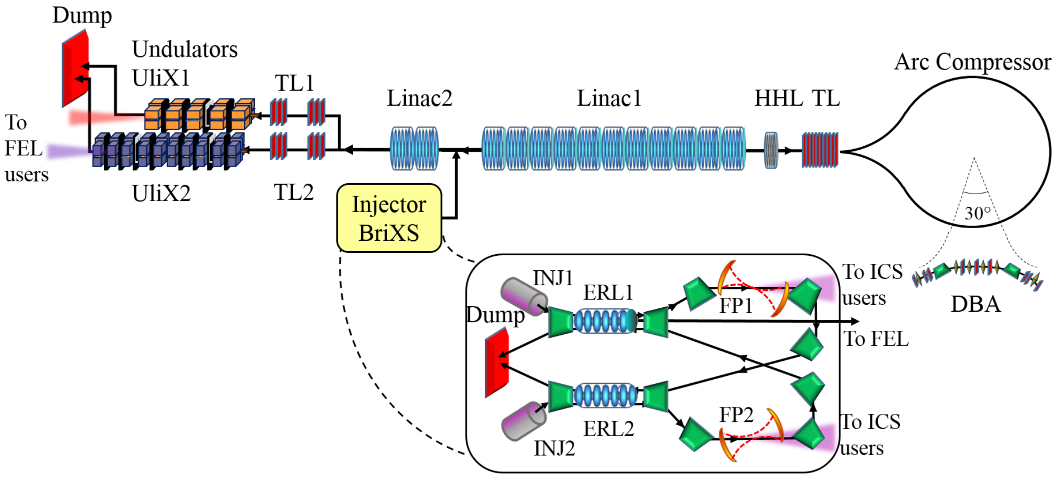

Figure 3.2: Conceptual lay-out for MariX, based on a two-pass CW Super-Conducting CW GeV-class Linac driven by a folded push-pull Energy Recovery 100 MeV Linac. BriXS: injector. L1 and L2: superconducting Linacs. HHL: high harmonic cavity. AC: arc compressor, DBA: double bend achromat. TL: transfer lines, UliX1 and UliX2: undulators, from [1]

The concept of the ICS high-flux Compton Source is to enable advanced radiological imaging applications to be conducted with mono-chromatic X-rays. These range from higher sensitivity in mammography to higher contrast in edge enhancement base radio-imaging with phase contrast, to selective radio-therapy with Auger electrons triggered inside tumoral cells by mono-chromatic photon beams, which are made possible only when the flux of ICS source reaches 10^{13} photons/s as expected in MariX/BriXS. While feeding hard X-ray beamlines for imaging, BriXS constitutes the injector for the downstream FEL.

The second block of MariX accelerator complex, sharing with BriXS the injector and the first cryomodule that brings the electrons to the energy of 100 MeV, is a two-pass recirculated Linac (Linac1 in Figure 3.2) equipped with a bubble-arc compressor (AC) similar to a conventional Double Bending Achromat (DBA) magnetic lattice of a storage ring (e.g. Elettra-like [88]). A high harmonic cavity and a dedicated transfer line are placed between Linac1 and the arc for chirping and optimizing the matching of the electron beam to the compressor. The arc compressor is composed by 14 DBAs, 10 with positive and 4 with negative curvature radius for a smooth matching to the Linac. It is indeed able to re-inject the electron beam leaving the Linac after being accelerated once, so to get boosted twice in energy in the second pass, being the first pass left-to-right (referring to the position of the elements of the line in Figure 3.2) and the second pass right-to-left.
At the same time, the combination of the dispersive strength of the ring with a suitable electron energy longitudinal chirp permits the arc to act as compressor with compression factors of the order of 100, thus preparing an ultra-short and high-

current electron beam suitable for FEL operation.

After a second short Linac devoted to fine tuning of the energy (Linac2, at the left side of Figure 3.2), the electron beam reaches a maximum 3.8 GeV energy, therefore allowing the FEL to radiate up to 8 keV actually operating only a 1.5 GeV Linac (that also includes the BriXS ERL delivering the initial 0.1 GeV injection energy). The undulators UliX1 (with period $\lambda_w = 2.8$cm, generating radiation from 200 eV to 4 keV) and UliX2 ($\lambda_w = 1.2$cm, delivering 2-8 keV) with their matching lines close the device. An important characteristics of the device is that the FEL and ICS experimental halls are contiguous permitting a possible mutual interaction.
Figure 3.3 gives a perspective view of the buildings hosting the infrastructure [1].

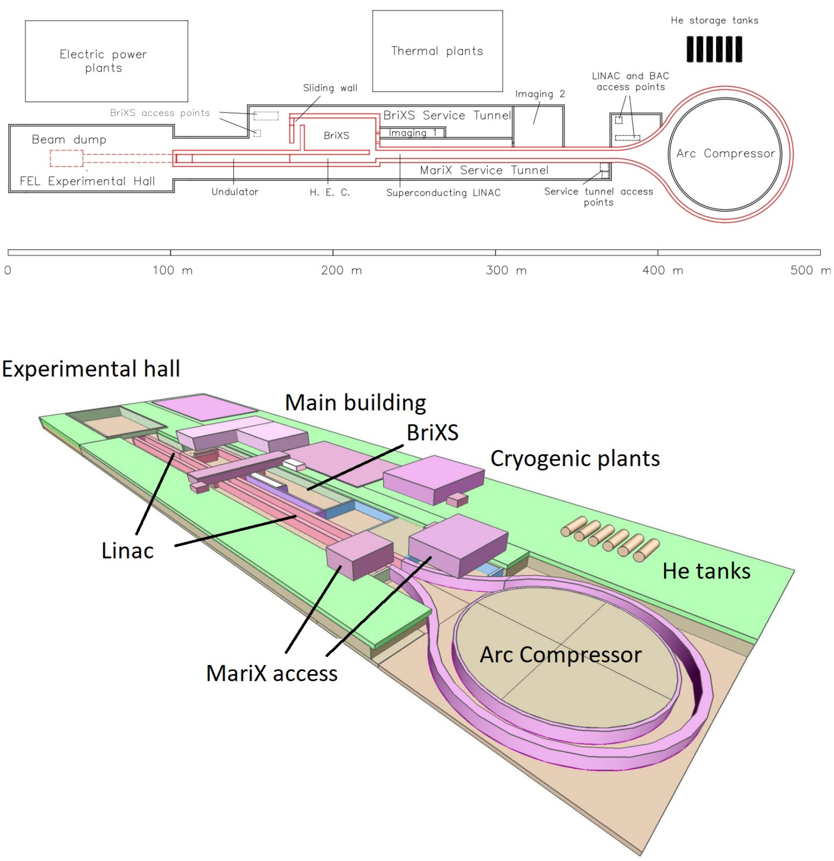

Figure 3.3: Schematic perspective representation of the buildings hosting the infrastructure, from [1]. Upper window: projected view, bottom window: perspective view

3.2 Motivation, Challenges and Goals

The most peculiar characteristic of the project is the high repetition rate of the two radiators: around 93MHz at high charge (200 pC) for the ICS and almost 1MHz at low charge (50 pC) for the FEL [89]. Two different working points are therefore defined (reported in Table 3.1) for the two light sources.

Table 3.1: ICS and FEL working points (WPs)

Source	Q (pC)	E (GeV)	$\Delta E/E$	ϵ (mm mrad)	I_{peak} (A)	Rep. rate (MHz)
ICS	200	0.1	1.6x10^{-4}	0.7-0.8	20	100
FEL	50	3.2	2.8x10^{-4}	0.3-0.4	1600	1

The main motivation behind the project design is to enable fundamental and applied research with non-receding photon beam performances tailored to linear spectroscopy and imaging experiments.
Two are the key aspects of MariX X-ray beams:

- operation in CW mode at very high repetition rate, spanning the 1MHz to 100MHz range;
- the marriage between two different (but related) X-ray production mechanisms: high gain Free Electron Laser with GeV-class ultra-bright electron beams, covering the 0.3 keV to 10 keV photon energy range, and Compton back-scattering of very large average power lasers (MW-class) by high average current electron beams (tens of mA), spanning from 20 keV up to 180 keV.

The rationale for such a marriage is based on a common feature requested by the two radiation sources: advanced capabilities to generate, accelerate, control, diagnose and deliver to the proper radiator client an electron beam with ultra-high phase space density, which in turns implies kA-class peak currents, very small transverse and longitudinal emittances, ultra low energy spreads, at an electron bunch charge in the tens to a few hundred pC range, operated in CW mode. Because of such tight requirements, we opted for a Linac based scenario for MariX, operating with Superconducting Radio Frequency (RF) Cavities and a two-fold Energy Recovery scheme, in order to fulfill the CW operation requirement as well as the handling of large electron beam power.
As anticipated in the introduction (Chapter 1), the main fields of research that can be explored by MariX are: imaging of proteins and nano-objects with nano-metric resolution, linear time-resolved femtosecond spectroscopy, new radiotherapy techniques that harness monochromatic hard X-rays, advanced multi-color X-ray based imaging. Thus the MariX science case almost coincides with that of LCLS-II and LCLS-II HE, but is achieved with a much more compact (and less costly) facility. The ultimate goal is the generation of less intense pulses, fully suitable for time-resolved experiments but not for multi-photon techniques, thus skipping the less interesting tender X-ray range and pointing at the soft and hard X-ray ranges only.

The techniques enabled by this kind of radiation are those exploiting the elastic and inelastic X-rays scattering, with fixed incident photon energy and efficient collection of the emitted photons. Also, the lower number of photons per pulse would greatly mitigate the risk of space-charge effects distorting the spectra in high energy photoemission spectroscopy. Time-resolved diffraction, spectroscopy and imaging obtained at MariX would provide new tools to chemistry, materials science, applied physics, catalysis and surface science, structural biology, quantum materials.
MariX is designed to be tuned for time-resolved experiments, ideally extending the capabilities of FERMI@ELETTRA in terms of energy range, and of the European XFEL, with a higher repetition rate and spectral stability. MariX has to be seen as the European answer to LCLS-II, at a fraction of the cost.

BriXS introduces technological challenges related to the high repetition rate (100 MHz) applied to energy recovery mechanisms, and the need to provide two beams of different characteristics and with different repetition rates for the two sources. An important challenge for the FEL is to achieve competitive FEL performance with those of the main operating machines and in the design phase (LCLS-II, EuXFEL). A further challenge of MariX's design study is set by the imposed constraints of the real estate availabilities at the Expo area, limiting the foot-print of the whole MariX machine to a total length smaller than about 500m as shown in Figure 3.2. As a matter of fact, Linacs driving X-ray FELs operating down to $1\AA$ radiation wavelength (thus 12 keV photon energy) are typically based on multi-GeV (10-20) Linacs which are multi km-long.

MariX comes out to be a real bridge between different generations of light sources, sharing with them common technologies (Linacs, undulators, optimized beam optics lattices, very high power lasers) but marrying them into a new form of synergy, represented by its unique and unprecedented layout blending energy recovery Linacs with arc compressors and recirculated acceleration.
The goal of the MariX FEL project is to radiate with continuity in a wavelength range between about 10nm and $1.5\AA$.
The next sections describe the components of the machine, namely the Inverse Compton Scattering source and the CW SuperConducting Linac with the bubble arc compressor preceeding the FEL lines, as well as their importance and novelty features with respect to existing machines. A brief description of the FEL source setup and undulators is contained in the last section.

3.3 BriXS, an ICS X-ray source

BriXS constitutes the first block of the MariX accelerator complex and works as injector for the second block, It is designed as a compact machine to produce Compton beams of high brilliance mono-chromatic tunable X-rays with an energy in the range from 20 to 180 keV.

3.3.1 Scientific Background for ICS sources

The primary aim of the BriXS project is to propose a unique facility, with performances comparable to those of modern synchrotron light sources but at costs and dimensions reduced by at least one order of magnitude, making it compatible with locations inside a university campus, a large hospital, a museum or a mid-size research infrastructure.

Enabled applications by such a machine are medical oriented research, mainly in the radio-diagnostics and radio-therapy fields as well as material studies, crystallography and museology for cultural heritage investigations. Mono-chromatic bright X-rays have been already proven to be suitable for advanced imaging at the sub $100\mu m$ resolution scale, with important reduction in the radiation dose to tissues joined to an upgraded signal-to-noise ratio and visibility enhancement via phase contrast imaging. Moreover there is an ongoing transition from R-D and demonstrative machines towards effective user facilities, based on Thomson/Compton back-scattering X/gamma-ray Sources, also known as Inverse Compton Scattering sources (ICS) [90]. Experiments on the source characterization [91], on imaging, K-edge techniques and computed microtomography with keV range X-rays have been already successfully performed. Compact sources like BriXS could exploit methods like diffraction, absorption, diffusion, imaging, spectroscopy currently used at synchrotrons and implement them in a laboratory size environment. In particular a machine like BriXS may offer the opportunity to take the machine into the hospital and treat patients in place.

3.3.2 Layout and important parameters

The BriXS layout (see Figure 3.4 in next page) consists of two symmetric beam lines, fed by two independent RF photoinjectors, where two equal and coupled Energy Recovery Linacs (ERL) accelerate the electron beams.

Electron bunches are extracted from the photocathodes (Inj1 and Inj2 at the left side of Figure 3.3) and are accelerated in the Gun RF structure to reach about 800 keV in a few centimeters. Downstream the Gun, a 4-meters long low energy acceleration follows for emittance compensation, energy spread damping and bunch compression. This low energy line accelerates the electrons up to 6.5MeV and brings the bunch in to the first dogleg, which is 1.5m long and offsets the beam transversally by 0.5m to join the ERL orbit.

The two ERLs (named ERL1 and ERL2 in Figure 3.4) accelerate (up to 100MeV) and decelerate the electrons. Bunches from Guns and traveling right away in the Figure are accelerated, those coming back from the IPs are decelerated during the energy recovery phase and brought simultaneously to a single beam-dump (push-and-pull coupled scheme). In this un-conventional scheme, each Linac is therefore traversed by two counter-propagating trains of electron beams, both gaining and yielding energy. This permits to drive two Compton X-ray sources with the same degrees of freedom of a Linac-driven source, in terms of energy and electron beam quality, resulting in a more stable scheme. Downstream the ERL a second dogleg

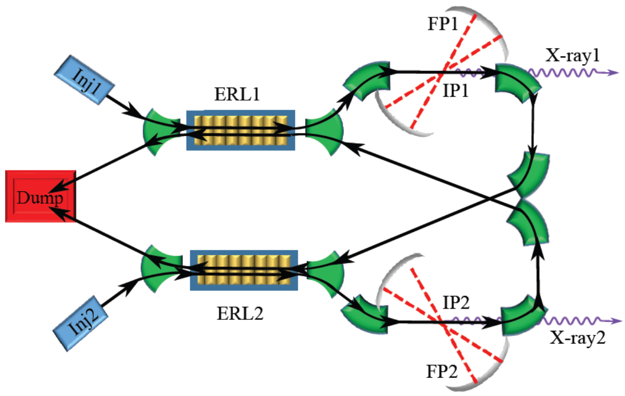

Figure 3.4: Pictorial view of the BriXS layout: From left: Inj1 and Inj2: photocathodes. ERL1 and ERL2: Superconducting linacs. FP1 and FP2: Fabri-Prot cavities. IP1 and IP2: interaction points. X-ray1 and X-ray2: X rays beams, going towards Compton users. The long side of this machine has a length of about 40 m.

takes the beam to the BriXS interaction point (IP) region. At the end of this second dogleg, the low and high charge bunches, associated to the two working points, are separated by a fast kicker, whose position represents the end of the common acceleration line.

Due to the superconducting technology of the Linacs, the infrastructure works at a repetition rate of 100MHz, corresponding to average currents up to 20mA. However, CW electron Guns capable to produce such an average beam current are not yet state of the art. Partial modifications of the beam lines to host additional Compton interaction points are under study.

Table 3.2: Electron beam parameters at the Linac exit

Electron beam	Units	
Average Energy	MeV	30 - 100
Bunch Charge	pC	100 - 200
Norm. emittances	mm mrad	0.6 - 1.5
Relative Energy spread	%	$10^{-2} - 10^{-1}$
rms Bunch Length	μm	400 -900
Repetition Rate	MHz	100

Typical electron beam parameters at the exit of the ERLs are collected in Table 3.2. The main electron beam parameters at the Compton interaction points are collected in Table 3.3.
The main features characterizing the Compton X-ray beams produced by BriXS are summarized in Table 3.4.

Table 3.3: Electron beam parameters at the Compton IP

Electron beam	Units	
Average Energy	MeV	100
Bunch Charge	pC	200
Norm. emittances	mm mrad	1.2
Relative Energy spread	%	$1.6x10^{-2}$
rms Bunch Length	μm	440
Focal spot size	μm %	19.4-23.4

Table 3.4: Summary of BriXS Compton X-ray beam specifications

Output beam	Units	
Photon energy	keV	20 - 180
Bandwidth	%	1 - 10
# photons per shot within FWHM bw		0.05-1 x 10^5
# photons/sec within FWHM bw		$0.05 - 1x10^{13}$
Photon beam spot size (FWHM)	cm	40 - 4
Peak Brilliance	Photons/s/mm^2/mrad^2/bw	$10^{18} - 10^{19}$
Radiation pulse length	ps	0.7 - 1.5
Repetition rate	MHz	100
Pulse-to-pulse separation	ns	10

3.4 The CW SC Linac with folding Arc Compressor

As already commented in the previous section, both radiators (named BriXS and MariX itself, the low and high energy lines respectively) are fed by a common acceleration line, ending with the ERL, where the electron energy reaches about 100MeV.

3.4.1 Fast Kicker and Booster

After the common acceleration line, the bunches are then separated via a fast kicker: one bunch (50pC at 1MHz) out of 100 is sent to the high energy (HE) MariX line where it is accelerated to about 3 GeV and compressed to 1.5-2kA range peak current. The undeflected bunches (200pC at about 100MHz) travel to the ICS Interaction Point. The main ingredient of the scheme is the photocathode laser, locked to the fast kicker: the interleaved scheme of the two working points of Table 3.1 is obtained injecting the low rep. rate bunches in the free RF buckets between the high rep. rate bunches at 93MHz.

The High Energy MariX section starts at the entrance of the main Linac (Linac1 in Figure 3.2), where the electrons are injected by a dedicated transfer line. The electron bunches must be taken from the 100MeV operating energy of BriXS up to

the operational energy of the 3.2 GeV FEL, maintaining a low normalized emittance ($\epsilon_{x,y} = 0.4 - 0.5$ mm mrad) and showing high peak current (I_p =1.6 kA). The HE MariX line dedicated to the main acceleration consists of a SC-Linac booster, composed of 11 cryomodules with 11 Tesla-like standing-wave (SW) cavities accelerating the beam in the 0.9-1.8 GeV energy range, followed by few higher-harmonic SC Tesla cavities (giving the 20m long HHL linearizer) to pre-correct the longitudinal phase space shape, which give an extra acceleration of about 50-100MeV. This pre-correction compensates the arc-compressor coherent synchrotron radiation (CSR) effects (see next section). Thanks to the SW operation of the booster, it is possible to accelerate electron bunches with an appropriate injection in both directions without the need to modify the cavity feed.
Considering an electron bunch with charge Q=50pC, peak current of 16A, longitudinal dimension of $\sigma_z = 360\mu m$, the beam dynamics before the arc (AC in Figure 3.2) is depicted in Figure 3.5.

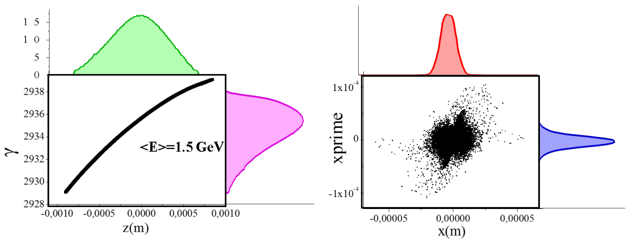

Figure 3.5: Longitudinal (left) and Transverse (right) phase space of the electron beam before entering the arc compressor

The electron beam here has an average energy of 1.5GeV, relative energy spread of 7x10^{-4}, transverse size of $\sigma_x = 6\mu m$ and normalized emittance of $\epsilon_n = 0.2\mu m$ in x,y directions.

3.4.2 The Arc Compressor

The arc compressors are tipically used in FELs (see Figure A.3 in Appendix A) to raise the peak current of the electron bunches, simultaneously compressing them, as they pass through dispersive paths characterized by the presence of numerous bending magnets.
The booster and the AC are designed such to avoid head-on collisions with counter propagating bunches. Thanks to this peculiar scheme, the total dimension of the booster (long less than 140m) is virtually doubled making it possible to accelerate the beam from 100 MeV up to 3.2 GeV and to compress it without the use of magnetic chicanes. The 1.8 GeV beam exiting the booster is then injected into a single-pass bubble arc [92] with the task of applying a 180 net deflection to the beam while increasing the bunches peak current by a factor close to 100. The arc compressor (AC) is composed by a series of achromatic cells and it allows to deflect the beam by large angles performing a bunch length compression without spoiling the

beam quality, as well as to control the emittance degradation by CSR effects (with an estimated final degradation of order 0.1mm mrad). In our case, such a device can be used to take a beam in a precise point of the line, deviate its path of 420 and bring it back to the starting point with inverted propagation direction. The beam thus traces back the booster doubling the energy gain (3.6 GeV).
The MariX AC is based on the arc described in Ref. [93] which uses the arc cells of the Elettra storage ring at Sincrotrone Trieste. The AC consists of 12 achromatic cells, called Double Bend Achromat (DBA) and often referred to as Chasman-Green lattice, repeated in series.

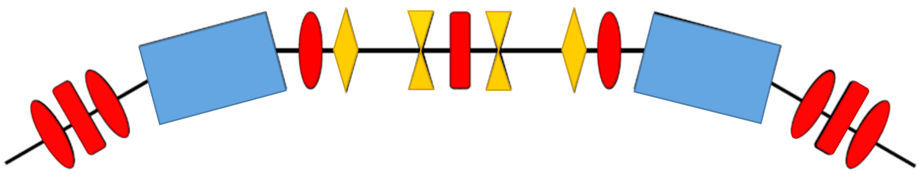

Figure 3.6: The DBA scheme or Chasman-Green lattice, is composed of 2 bending magnets (in blue) 9 quadrupoles (in red) and 4 sextupoles (in yellow), from [89]

The DBA cell (shown in Figure 3.6) bends the beam by 30 and is composed by: 2 bending magnets, which deviate the beam by 15 each and are responsible for opening and closing the dispersion in the line, 9 quadrupole magnets, used to control the transverse dimensions of the beam and to invert the dispersion trend, and 6 sextupole magnets, used to compensate for the chromatic aberrations introduced by the quadrupoles due to the beam's energy spread. Figure 3.7 shows how DBAs are used in the Elettra storage ring and in MariX. In the Arc lattice, the cell with inverted concavity (in red in Figure) serves to bend the beam in the opposite direction.

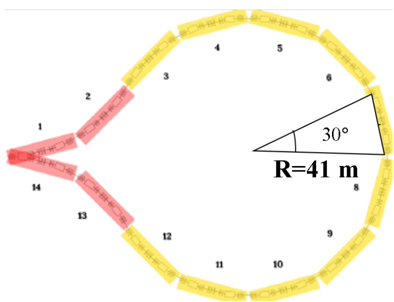

Figure 3.7: The AC layout. It is composed by 2 DBAs that fold the beam to the left (in red), 10 DBAs that bend to the right (in yellow) and finally 2 DBAs that bend it left again bringing it back to the starting point (in red)

Therefore it must be built with magnets fed by inverted currents, and the generated

reverse magnetic field opens the dispersion in the opposite direction, so that the less energetic particles are curved with a greater angle but this time to the left. The quadrupoles apply a restoring force towards the propagation trajectory of the centroid of the beam focusing on the horizontal axis, whereas sextupoles apply a dipolar kick which grows symmetrically as electrons move from the propagation axis.
When a bunch of high current passes through a bending magnet it emits Coherent Synchrotron Radiation (CSR), a collective radiation emission phenomena by neighbouring particles responsible for the degradation of transverse emittance of the beam [marcello], whose power scales as

$$P_{CSR}[W] = 2.42x10^{-20} \frac{N^2}{\sqrt[3]{r^2[m]\sigma_z^4[m]}} \tag{3.1}$$

where N is the number of emitters, r the bending radius and σ_z the rms bunch length. As we see, shorter bunches (therefore higher peak currents) emit the greater power. In the case of MariX, beam power losses are negligible and the problem may arise from the influence of the CSR emitted by the bunch tail on the upstream particles, introducing microbunching instability. This leads the energy spread to rise, that is then translated into transverse emittance dilution in the subsequent bending magnets. Moreover, the CSR can limit the compression factor by deforming the longitudinal phase space of the bunch due to non-uniform local energy losses.
CSR emission (3.1) is strictly related to the the bunch length, thus the most of the detrimental effect in MariX takes place mostly in the last 2 DBA since the peak current grows hyperbolically during the compression mechanics. As anticipated before, a CSR pre-correction is given by a third harmonic accelerating cryomodule, exploiting only the cavities gradient, while sextupole magnets along the arc may also be used to correct high order correlations in the longitudinal phase space.
Thanks to the MariX arc compressor, it is possible to extract the bunch at maximum peak current gain, meaning a multiplication factor of about 100, going from 16A up to more that 1.5 kA.

Considering now an electron bunch with charge Q=50pC, peak current of 1.6kA, longitudinal dimension of $\sigma_z = 20\mu m$ as the one obtained with the arc operation, the beam dynamics after the arc is depicted in Figure 3.8.

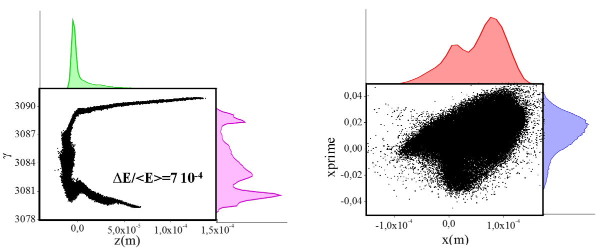

Figure 3.8: Longitudinal (left) and Transverse (right) phase space of the electron beam after the arc compressor

The electron beam here has an average energy of 3.2 GeV, relative energy spread of 7x10^{-4}, transverse dimensions of $\sigma_x = 52\mu m$, $\sigma_y = 14.5\mu m$ and normalized emittances of $\epsilon_{n,x} = 1\mu m$, $\epsilon_{n,y} = 0.2\mu m$ in x,y directions.
Two extra cryomodules, constituting the 30m long Linac2 in Figure 3.2, are installed between the energy-doubling booster and the FEL undulators to tune the final energy of the beam[1] (±300 MeV).

3.5 The FEL X-ray source

The parameters of the electron beam at the exit of the acceleration stage, before entering the photon machine, are summarized in Table 3.5.

Table 3.5: Nominal electron beam parameters for FEL operation

Electron beam	Units	
Energy E_e	GeV	1.6 - 3.8
Charge Q	pC	8 - 50
Peak current I_p	kA	1.5 - 1.8
Norm. rms emittance ϵ (slice)	mm mrad	0.4 - 0.6
Energy spread $\Delta E/E_e$ (slice)	10^{-4}	2 - 4
rms pulse duration	fs	1.5 - 16

The requirements on beam parameters such as emittance (see Eq. (B.85-B.86) in Appendix B), peak current and energy spread need to be satisfied in the longitudinal portion of the electron beam where lasing is desired. The term *slice* is associated with a portion of the "lasing" part of the beam, while the term *projected* refers to a property of the whole beam.
We couldnt exceed 50 pC electron charge for energy dump need.

3.5.1 Introduction and layout

At this point of the machine, the FEL electron beam has reached a maximum 3.8GeV energy, therefore allowing the FEL to radiate up to 8keV actually operating only a 1.5 GeV Linac (including also the BriXS ERL delivering the initial 0.1 GeV injection energy). After the acceleration stage, the electron beam enters the photon machine area, constituted in sequence by undulators (UliX1 and UliX2, see next section for more details), radiation diagnostics and photon beamlines.

[1]In order to suppress the microbunching instability and its negative effects on the higher harmonic lasing in the FEL seeded operation, an upgrade of the layout may also include a laser heater (LH) after the cathode, used to induce a uniform heating of the electron beam, or a collimation system after these last cryomodules and before the FEL undulators. The LH can use the chirped pulse beating technique, where the intensity modulated LH pulse is produced by the interference between two chirped laser pulses, temporally separated. This leads to an output envelope of the laser pulse with a quasi-periodic modulation at a beating frequency proportional to the delay.

The layout of the Free-Electron laser X-ray source at MariX, main object of this study and second radiator of the complex, is shown in the upper-left part of the entire complex in Figure 3.2, and it is preceeded by a couple of transport and matching lines (TL1 and TL2). Each of these lines consists in a couple of quadrupole triplets separated by a long drift, and it has been conceived to match bunches entering the undulators with a wide range of energies.
The matching (see section 4.1) is performed imposing the periodicity of the Twiss functions ($\alpha(z)$ and $\beta(z)$)[2], and the existence of the solution of this problem depends on beam parameters, such as average beam energy and normalized transverse emittance, and on the emitted radiation wavelength too. The quadrupoles and the drifts are described by their associated transfer matrix, like lenses in optics, and the product between the 6D vector associated with the beam $X = (x; p_x; y; p_y; \Delta z; \delta)^T$ and these matrices gives the transferred beam vector after the propagation. From the transfer line equivalent matrix, obtained multiplying all the matrices associated with the optic elements, one can obtain the transfer matrix for the Twiss parameters and figure out how to design the TL.

3.5.2 Characteristics and Working point definition

The selection of the best FEL parameters has been done by considering the following guidelines, already used in the definition of the electron machine [89]:

- minimizing the dimension of the device to remain within the bunker allocated dimensions and containing the overall price of the structure,
- maximizing the performance of the FEL in terms of versatility, power, coherence, stability, in order to satisfy the widest range of users,
- using technologies and techniques at the limit or just beyond the state of the art, in order to balance risks and competitiveness.

Figure 3.9 (see next page) shows the radiation wavelength mapped onto the undulator period and the electron energy for the undulator maximum magnetic field at $B = 1$T, for low (left panel) and high (right panel) photon energies according to Eq. (2.1).

In the low photon energy regime (left panel), that is for radiation wavelength in the nanometric range, there is a wide range of options regarding the determination of undulator period and type, all well within the limits of the state of the art.
Undulators with short periods ($2 - 2.5$cm) are efficient at lower wavelengths of order of 1nm, while on the contrary, larger undulator periods ($3.5 - 5$cm) allow radiation at large wavelengths. An undulator with period $\lambda_w = 2.8$cm allows the MariX electron beam to emit from 1nm to more than 12nm with a magnetic field of 1T (corresponding to a value of the undulator parameter $a_w = 1.9$) and to extend the

[2] A general treatment of the transverse dynamics of an electron beam and the Twiss parametrization can be found in Ref. [94]

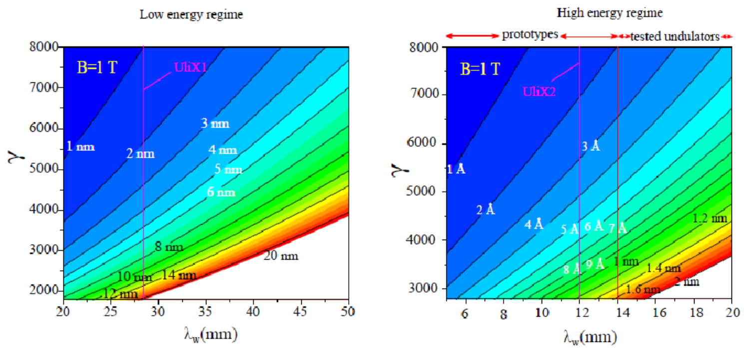

Figure 3.9: Radiation wavelength λ mapped onto the undulator period λ_w and the electron Lorentz factor γ for the undulator peak magnetic field in two different regimes, low (left panel) and high (right panel) photon energies, from [89]

range towards $\lambda = 0.5$nm by lowering the magnetic field, although with less efficiency.

The definition of a second undulator device for high photon energy radiation is more difficult. As shown in the right panel of Figure 3.9, for a permanent magnet undulator (PM undulator), the shorter period undulator device has $\lambda_w = 1.4$cm, which is a joint KYMA-ENEA project commissioned and tested at SPARC LAB in the INFN National Laboratory of Frascati [95]. This value is close to that (1.5cm) used by the SwissFEL undulators at PSI [96] and prototypes at 8mm and 4mm are under study. A brief digression on different types of undulator technology is given later in section 3.5.3.
Figure 3.9 also shows that the objective of radiating at $1.5\mathring{A}$ with the MariX electron beam can be attained only with undulator periods close or less than 1.2cm. In this way, considering a magnetic field of about 1T and varying the electron energy, the wavelength domain of the high photon energy line ranges between $1 - 1.5$nm and $1.5\mathring{A}$.

Table 3.6: Undulator parameters

Parameter	**UliX1**	**UliX2**
Type	pern. mag.	perm.mag perm. mag. segmented
Radiation mode	SASE	SASE Seeded-Cascade
Period λ_w	2.8cm	1.2cm
a_w	< 2.5	< 0.8
Length L_w	$30 - 35$m	≈ 60m total ≈ 70m
Wavelength range	$11\text{nm} - 8\mathring{A}$	$9 - 1.5\mathring{A}$ $9 - 2.5\mathring{A}$
Polarization	linear	linear

The undulators for MariX, whose parameters are summarized in Table 3.6, are supposed to be two: a first undulator UliX1 (Undulator Light Infrastructure for X-rays 1) with undulator period $\lambda_w = 2.8$cm and strength up to $a_w = 2.5$, 30m long[3]; and a second one, UliX2, with $\lambda_w = 1.2$cm and strength up to $a_w = 0.75$ with length of about 60m. The radiation domain from about 1.5$\mathring{A}$ to more than 10nm is covered. In the last column of Table 3.6, the second line refers to a possible sequence of modulators for the seeded-cascaded FEL option, operated with the UliX2 undulator as radiator (see section 4.2.2).

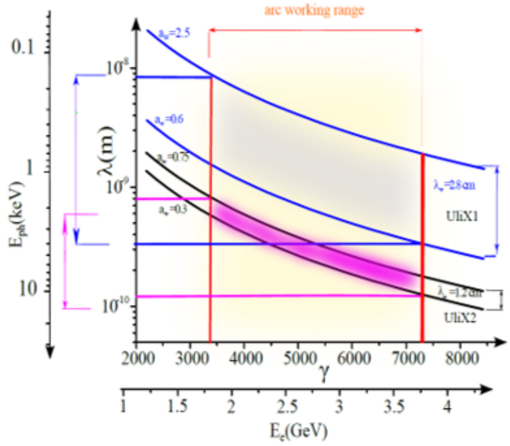

Figure 3.10: Wavelength (photon energy) vs electron Lorentz factor (electron energy) for the two undulators ULIX1 and ULIX2

Figure 3.10 shows a plot of the wavelength and photon energy domain covered by the two undulators UliX1 and UliX2 (in the not-segmented version) as function of the electron beam energy [89]. The yellow area delimits the wavelength domain (from 100eV to 4keV, soft X-ray range) produced in the undulator UliX1. The red area, instead, is relevant to UliX2 (from 2keV to 8keV, tender-to-hard X-ray regime). In principle, the arc compressor could work between 0.8 GeV and the maximum energy of 1.9 GeV attainable after the first round in the Linac, permitting the energy at the entrance of the undulator to span from 1.6 GeV and 3.8 GeV($\gamma \in [3200, 7400]$). Given this interval for the electron beam energy, the radiation should range from about 10 nm to 1.5$\mathring{A}$ (0.1-8.3 keV) with continuity.

An estimate of the required dimensions of the two undulators (see Table 3.6) can be obtained using the Ming Xie formulas for gain and saturation lengths, reported in section B.5, and using the fact that $L_{sat} \approx 20L_g$.

3.5.3 Undulator technology

In the range of periods from 1 to 2 cm, the state of the art permits a significant number of options, which are summarized in Figure 3.11, where the peak magnetic

[3]The undulator length is defined as $L_w = N_w\lambda_w$ where N_w represents the number of periods.

field versus the gap to period ratio g/λ_w is reported for various magnet types and for the different polarizations:

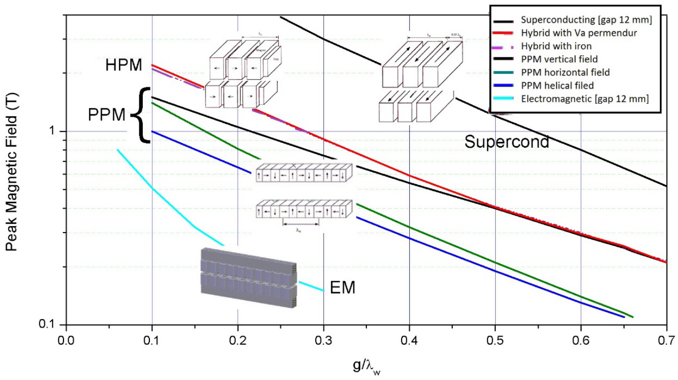

Figure 3.11: Undulator Technology status. Peak magnetic field as function of the gap to period ratio. g is the gap and λ_w the undulator wavelength

We can distinguish:

- The conventional Halbach schemes (Pure Permanent Magnets PPM)
- The Hybrid Permanent Magnets (HBM)
- The Super conducting (SC)
- The Electromagnetic Undulators

We will exclude this last choice because it is a technology with limited performances in terms of magnetic field vs. gap to period ratio. A peak magnetic field of 1T guarantees the MariX FEL operation in most cases both for low and high photon energy emission.
The superconducting technology seems to be the most efficient, permitting to produce fields in excess of 1T also with g/λ_w of the order of 0.5. It however involves complex cryogenic and mechanical structures, so that supercunducting undulators are not used for routinely operations. The Pure Permanent Magnet Undulator technology is until now the most used in most FEL facilities and seems to be the most practical solution for every requested period. These devices operate without a cooling system and they can be used both in vacuum (the undulator magnets are in a vacuum chamber) or in air. In this last case, a waveguide has to be installated between the two magnets bars to allow the electrons to move under vacuum.
The newest generation of undulators with 2.8cm period (as the one requested for UliX1) presents variable gaps, accurate field uniformity, easy movimentation, total accessibility, control of the polarization. They can be implemented both in-air and in-vacuum.
In-vacuum undulator (such as for instance the Cornell Synchrotron Undulator [97], $\lambda_w = 2.4$cm shown in Figure 3.12) permits to accost vertically the gaps without constraints and to reach a higher magnetic field than the in-air undulators, where the

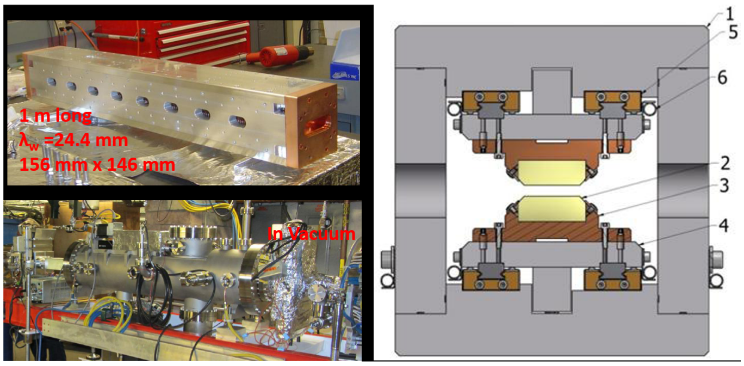

Figure 3.12: CHESS Compact Undulator for the Cornell High Energy Synchrotron [1]. 1) Aluminium plates. 2) Permanent magnet blocks.3) Copper holders 4) Base plates holding PM block/holder assemblies. 5) Miniature rails. 6) Cooling lines

inter-magnet gap is limited by the dimension of the electron pipe, typically of several millimeters. The Apple undulators designed for the Athos beam line of SwissFEL at PSI [2] (foreseen at $\lambda_w = 4$cm, see Figure 3.13) are based on a modular structure[4] made by four independent sectors, that can be conceived with various shapes, for instance rectangular (Apple II) or triangular (Apple III).

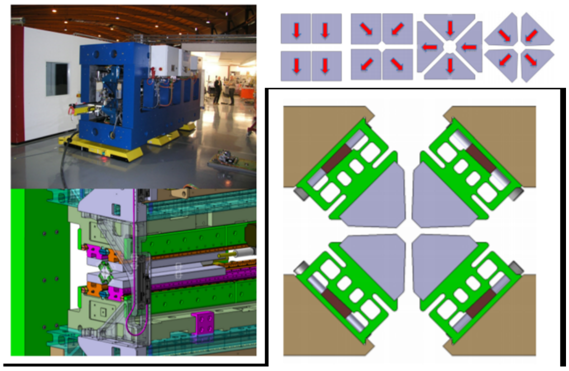

Figure 3.13: Apple undulator scheme of the undulator of the Athos line at SwissFEL [2]. Left: images of the structure. Right top: various possible magnet configurations APPLE Designs: APPLE II, APPLE III, DELTA, proposed SwissFEL UE40. Right bottom: actual magnet scheme of the Radia model of UE40 magnet structure

In all versions, the room for a round vacuum chamber of 5-7mm is allocated in the center, while the magnets delimit the vacuum chamber with room (2.5mm) only for magnetic measurements. This design increases the field and can be implemented also with shorter period, in particular with the UliX1 period at $\lambda_w = 2.8$cm.
As already mentioned, the state of the art of short period undulators actually tested in FEL experiments is represented by the Kyma-ENEA [3] quadrefoil prototype

[4]The modularity of the magnet structure permits to shift them longitudinally. Shifting two adjoining magnets with respect to each other allows to vary the field intensity, while shifting alternate magnets permits to change the polarization from linear to circular.

present at SPARC LAB, with period 1.4cm and peak field of about 0.6T. The quadrefoil shape guarantees compactness of the structure and smaller transverse dimensions. It moreover facilitates the positioning of a beam pipe, whose external and internal dimensions are respectively 5 and 4mm, large enough to allow an easy control of the electron beam.
Other undulators of similar period ($\lambda_w = 1.5$cm) are implemented at the Aramis line at the SwissFEL. They are arrays of planar undulators, made by a new type of permanent magnet, mounted in vacuum tanks. The inter-magnet gap is about 4.5mm. In addition, these undulators are operated at room temperature, so expensive and demanding cooling systems are avoided. The present technologies make possible to foresee undulators of period 15% less than the actual prototypes in few years' time. Other 'exotic' solutions can be adopted for some parts of the undulators for eventual upgrades/tapering. A very interesting option is that of using High Temperature Superconductors (HTS) composed by Rare Earth, Barium-Copper-Oxide.

A general undulator magnetic channel is made by several undulator modules whose total length covers the distance required to reach the saturation in the FEL. A single undulator (with no segmentation), tens of meters long, presents difficulties both from the point of view of the construction and of the transport of the electron beam along it. The magnetic field of the single undulator module is in fact not able to impart a significant focusing effect to a 1GeV energy electron beam passing through it, so that the undulator is almost equivalent to a long drift section, which will make the beam diverging during propagation. The undulator is thus divided in sections with some Focusing-Drift-Defocusing-Drift (FODO) cells with alternate gradient quadrupoles. A sketched out picture of the undulator system is presented in Figure 4.3 of Chapter 4 for example.

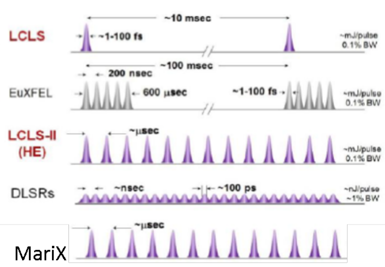

FEL	Pulse per second
LCLS	120 Hz
SACLA	30-60 Hz
FERMI	10-50 Hz
PAL	30-60 Hz
PSI	100 Hz
EuXFEL	27 kHz
LCLS II	1 MHz
MariX	1MHz

Figure 3.14: Temporal pulse structure achieved by MariX compared to other facilities

The FEL lines are able to provide coherent X-rays with individual pulses not exceeding the linear response regime and space charge effects, tailored for time-resolved spectroscopies. This implies a number of photons of 10^8 per 10 fs-long pulses, 3-4 orders of magnitude lower than the individual peak intensity of the current X-FELS. However the 4-5 orders of magnitude gain in repetition rate allowed by MariX restores the high flux per second of the most advanced synchrotron sources, still having ultrashort pulses suitable for time resolved pump-probe methods in photoelectric effect and inelastic X scattering experiments (see Figure 3.14).

With the current FEL technology, the applied attenuation of X-ray beams (as at SACLA), in order to measure an undistorted core level spectrum, limits the statistics of these measurements to a lower time integrated flux per second with respect to MariX. Moreover, the high longitudinal coherence of the beams will enable pump-probe methods at 10-100fs accuracy and with high statistics.

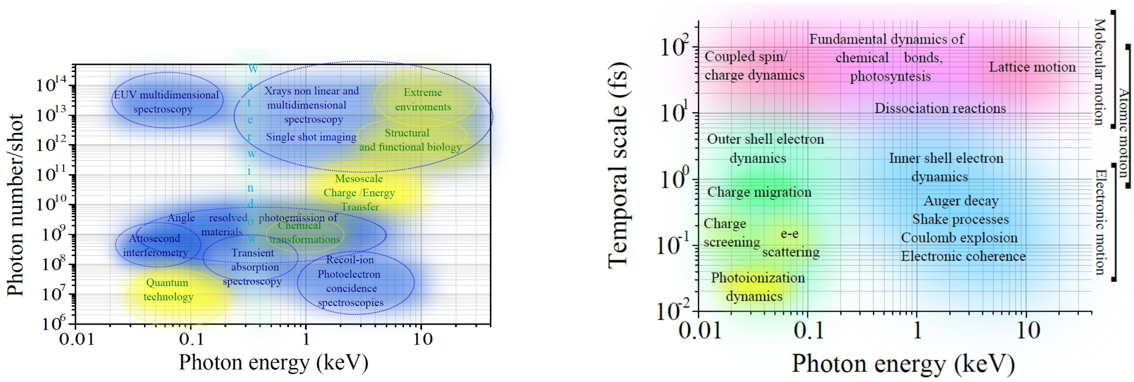

Figure 3.15: Techniques (in blue) and research areas (in yellow) mapped vs photon energy and number of photons per shot (left panel), Molecular, atomic and electronic phenomena mapped vs their photon energies and temporal duration (right panel), from [89]

Figure 3.15 (left panel) shows the most important application techniques (in blue) and the research areas (in yellow) mapped onto photon energy and number of photons per shot of the radiation. Particularly interesting energies in the soft X-ray range are the carbon K-edge (280 eV, 4.4 nm) and the domain of the water window (around ∼415 eV, 3 nm), investigated by the MariX low energy photon line. Going toward higher energies, the oxygen (∼500 eV) and the silicon (1.8 keV) K-edges follow. The access of the high energy line to energies above 5keV allows the analysis of key earth-abundant chemical elements and provides atomic resolution[5]. The availability of wavelengths approaching or exceeding the $\mathring{A}$ range (∼10 keV) provides novel fundamental discovery capabilities for science.

Soft X-FELs cover the up-right quadrant of Figure 3.15, with energies typically ranging between 100 eV up to more than 20 keV and photon numbers per shot in excess of 10^{14} for the lowest energies and decreasing progressively down to 10^{10} for

[5]This last regime encompasses the K-edges of elements necessary for the large-scale development of photocatalysts involved in the electricity and fuel production, as well as the biologically important selenium, used for protein crystallography. Studies of spin-orbit coupling which is at the basis of many aspects of solid state quantum mechanics can be also performed in this regime.

energies exceeding 12keV.
Another demanding request of the X radiation is the ultra-short duration of the pulses (femtoseconds or even less), that allows to probe the domain of the electronic dynamics. Figure 3.15 (right panel) presents the molecular, atomic and electronic phenomena mapped onto their photon energies and temporal duration. The dynamics of molecular and atomic phenomena can be detected by soft X-rays with pulse length of 10-100fs, whereas the electronic processes involving outer and inner shells develop on atto/femto-second scale and need therefore probes and methodologies in this duration range. Furthermore, since high intensity X-rays result in strong radiation damage of the samples, X-ray exposure shorter than the explosion time-scale of biological samples is needed [89] (diffraction before destruction).
The trend for newest and future set-ups is that of increasing by orders of magnitude the repetition rate with respect to the 10-100Hz available in most present FELs (see Figure 3.14). A continuous time distribution of the pulses should be moreover suitable. A high repetition rate of 1MHz and an uniform time structure should provide the possibility to collect more than 10^8 scattering patterns (or spectra) per day with sample replacement between pulses, enabling methodologies as the serial crystallography and the multidimensional X-ray spectroscopy. Regarding spatial coherence, the availability of a high average coherent power in the soft-hard X-ray range, combined with programmable pulses at high repetition rate, will enable studies of spontaneous ground-state fluctuations and heterogeneity at the atomic scale from micrometric and femtosecond scales using powerful time domain approaches such as the X-ray photon correlation spectroscopy (XPCS). These capabilities will further provide a qualitative advance for understanding non-equilibrium dynamics and fluctuations via time-domain inelastic X-ray scattering (FT-IXS) and X-ray Fourier-transform spectroscopy approaches using Bragg crystal interferometers. The present scientific impact of inelastic X-ray scattering and spectroscopy in the hard X-ray range (RIXS and IXS) suffers for the lack of large spectral flux from temporally incoherent synchrotron sources. New generation X-ray FELs will provide an increased average spectral flux compared to synchrotron sources, opening new areas of science and exploiting high energy resolution and dynamics near the Fourier transform limit.

The peculiarity of MariX is the extremely large repetition rate, positioning it among the sources with largest average flux worldwide. Moreover, the 200 fs down to 10 fs pulse durations coupled to the capability for double pulses with independent control of energy, bandwidth and timing open up experimental opportunities that are simply not possible on non-laser sources.

Chapter 4

Results of start-to-end FEL simulations

The previous Chapter introduced the two MariX FEL lines, named UliX1 and UliX2. This Chapter focuses on the analysis of their performances and presents the main results obtained. Start-to-end FEL simulations have been carried out using the three-dimensional FEL code GENESIS 1.3 (see appendix C) in time-dependent mode.

As reported in section 4.1 of this Chapter, the study initially considered a pseudo-ideal electron beam. Thanks to the wide range of electron beam parameters allowed by the MariX injector and accelerator, two different radiation ways, corresponding to long multiple spiked and short single spiked X-ray signals, can be defined as FEL standard operation modes and are reported in Table 4.1. The two beams present quite similar slice characteristics, but different charge and rms bunch lengths. The long signal case will be indicated with a prime in the following sections.

Table 4.1: Standard operation modes of the MariX FEL, here reported for a peak current of $I_p = 1.6$kA. The longitudinal extension of the current profile σ_I and the peak current are related to the bunch charge Q by the relation $Q = \frac{I_p \sigma_I}{c}$ where c is the speed of light

Parameter	**Short signal**	**Long signal**
Charge Q (pC)	8	50
Peak current I_p (kA)	1.6	1.6
Beam rms length σ_I (μm)	1.5	9.4
Output pulse shape	single spiked	multiple spiked

Starting from section 4.3, the real MariX beam produced by the upstream acceleration stage is introduced, discussing its matching to the undulator lines together with the main results and differences with the pseudo-ideal beam.

4.1 Simulations with the ideal beams

In this section, simulation results with ideal beams are shown to test and describe the MariX FEL performances' range.
A pseudo-ideal electron beam with the nominal properties of the machine beam[1] (listed in Table 3.5) but with a Gaussian shape of the longitudinal current profile (see Figure 4.1) is considered, while the beam energetic and transverse distributions are automatically set by some parameters in the code input file (see section C.4 of Appendix C).

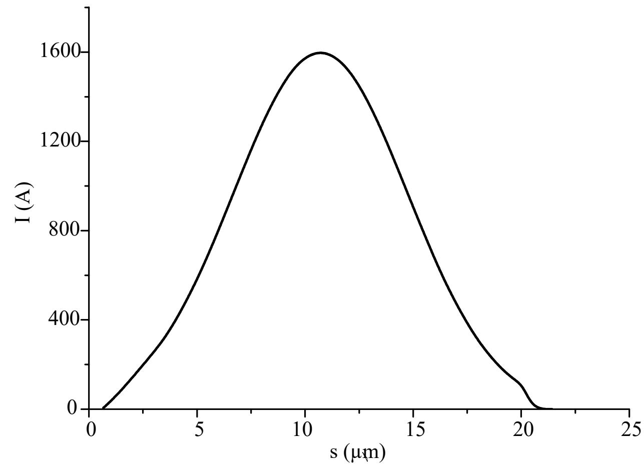

Figure 4.1: Pseudo-ideal electron beam. In this example its longitudinal current profile for a peak current of 1.6kA and a charge of 50pC (second column of Table 4.1) is considered

The undulators' structure and the need of matching the beams in general come from the fact that the trajectory of a given electron bunch within an undulator is unstable, because of the quadrupolar components of the undulator magnetic field, characterized by a strong vertical focusing effect and a weak horizontal defocusing effect on the electron beam. For this reason, the undulators are normally divided in modules separated by magnetic quadrupoles that compensate for the undulator quadrupole effect.
To perform the matching inside the undulator, one has to impose the periodicity of the Twiss functions (α(z) and β(z)) all over the periodic module of the lattice (see Figure 4.2), always crosschecking the quadrupole strength needed to compensate the undulator unwanted effects and the spot size of the beam in the quadrupole bore.

[1]For ideal beams, properties such as energy spread and emittance are assumed to be constant over the beam, so that slice and projected properties are the same. In section 4.2 the real beam is introduced, and in that case the beam distribution is given so that slice and projected properties do not coincide.

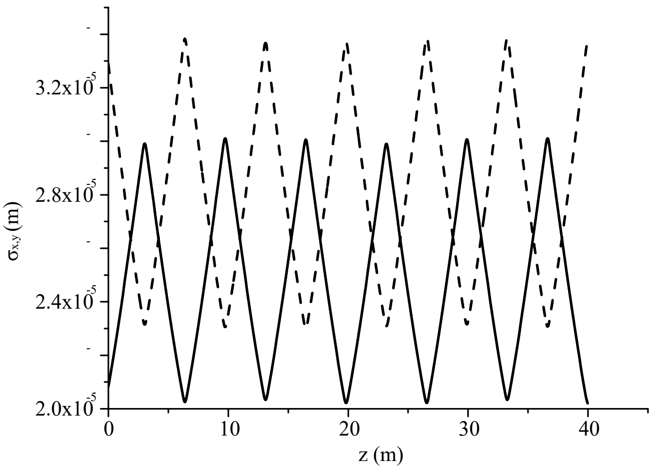

Figure 4.2: Beam dimension $\sigma \propto \beta$ (σ_x dashed, σ_y solid) for $\lambda = 3$nm and $G =$ 10T/m

We define the average transverse Twiss parameters of the electron beam in the undulator as:

$$\langle \beta_{x,y} \rangle = \frac{1}{L_{w1}} \int_0^{L_{w1}} \beta_{\mathrm{x,y}}(z)\mathrm{dz} + \frac{1}{L_{w2}} \int_{L_{w1}+L_{w2}+L_d}^{L_{w1}+L_d} \beta_{\mathrm{x,y}}(z)\mathrm{dz} \tag{4.1}$$

where L_{w1}, L_{w2} and L_d are the length of the two undulator modules in the FODO elements, and L_d the drift space between them; $\beta_{x,y} = \sigma_{x,y}^2 \gamma / \varepsilon_{x,y}$ ($\varepsilon_{x,y}$ being the normalized emittance respectively in the x,y direction and $\sigma_{x,y}$ the transverse dimensions of the electron beam).
The beta average parameters in the two planes are required to be equal in the two sections and the matching is therefore performed by minimizing the difference $| \langle \beta_x \rangle - \langle \beta_y \rangle | = \mathrm{min}$. The beta function depends on the undulator strength a_w and on the beam energy, that can both be varied in order to tune the radiation wavelength. In Figure 4.2, the variation of the beam dimensions (thus indicating a variation of the beta function) within the undulator is shown for a case with $\lambda = 3$nm and $G = 10$T/m.

4.1.1 Low energy photon line

We first analyze the low energy FEL line, named Undulator light infrastructure for X-rays 1 (UliX1), considering as basic option the conventional FEL SASE radiation mode (discussed in section 2.1 and in Appendix B.4) for the two different operation modes listed in Table 4.1.
In addition to variation of the electron bunch charge, duration and of the energy chirp profile, the use of variable gap undulators and the optional integration of magnetic chicanes between two consecutive undulator modules allow a full set of different

upgraded SASE operation regimes, as the chirp and taper technique [98,99], the purified SASE [100], the optical klystron operation [89].

As previously described and summarized in Table 3.6, the undulator UliX1 has period $\lambda_w = 2.8$cm, strength up to $a_w = 2.5$ and is about 30 meters long. A sketched out picture of the module of periodicity of the undulator system is presented in Figure 4.3, while Figure 4.4 depicts an example of the undulator sections and quadrupole positions in z (for a length z=40m).

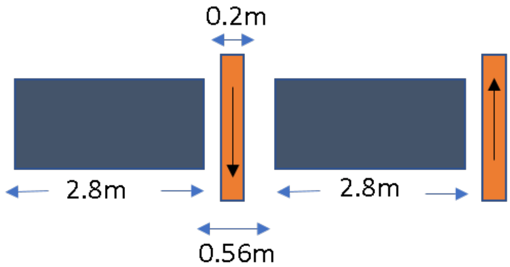

Figure 4.3: Scheme of a single module of the undulator UliX1. The blue boxes represent the undulator modules ($L_{mod} = 2.8m$), separated by a 20cm long quadrupole. The extra drift space between the modules can be filled in with radiation diagnostics such as beam position monitors (BPM) or phase shifters

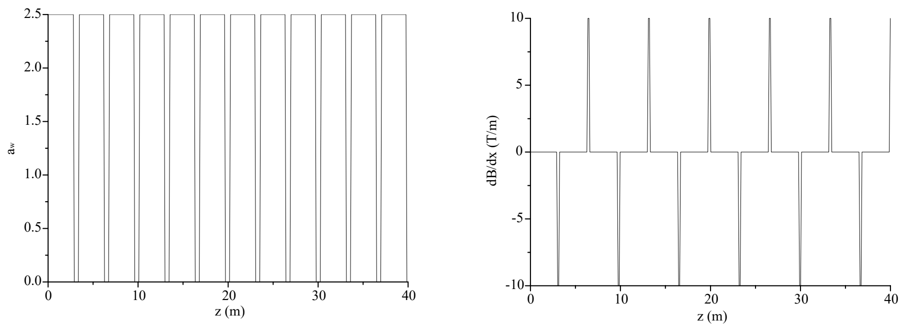

Figure 4.4: Undulator parameter a_w and quadrupole field as a function of the longitudinal position within UliX1, as given by GENESIS 1.3 (see section B.4.1)

The considered undulator is made by sections of 100 periods. The quadrupoles are 8 periods long and placed between two drifts, 4 and 8 periods respectively long, with magnetic field gradient $q = dB/dz$. With $\lambda_w = 2.8$cm, the undulator module turns out to be 280 cm long, followed by 56 cm of drift (including the quadrupole). The quadrupole will be designed with the idea of minimizing the longitudinal space occupation in the gap between undulators and steering correctors can be included in the quadrupoles structure as additional coils, so that the second drift turns out to be long enough to allow the installation of beam position monitor, phase shifters, magnetic chicanes or some diagnostics for radiation [89].

As already said in section 3.5, the maximum electron energy value is assumed to be 3.8GeV while the minimum energy is limited to $1.6-2$GeV by the arc compressor operation (see Table 3.5). As shown in Figure 3.10, by changing either the electron energy within these limits or the undulator strength, UliX1 can radiate from a maximum of 10nm (0.12keV) to a minimum of about 0.8nm (1.5keV).

Table 4.2: Simulations for UliX1 with $E_e \sim 3$GeV, $\lambda = 3$nm, $\lambda_w = 2.8$cm. Radiation properties are reported on average

Electron beam	A	B	C	A'	B'	C'
Q (pC)	8	8	8	50	50	50
ϵ (mm mrad)	0.5	0.75	0.5	0.5	0.75	0.5
$\Delta E/E$ (x 10^{-4})	2	2	5	2	2	5
I_p (kA)	1.6	1.6	1.6	1.6	1.6	1.6
Radiation	A	B	C	A'	B'	C'
ρ_{1d} (x 10^{-3})	1.56	1.37	1.56	1.56	1.37	1.56
$L_g - L_{g3d}$ (m)	0.82-0.97	0.94-1.1	0.82-1.1	0.82-0.97	0.94-1.1	0.82-1.1
N_{ph}/shot (x 10^{11})	1.91	1.27	1.15	60.3	45.2	44.2

The undulator performance has been simulated for different combinations of electron beam parameters and for three different wavelenghts (namely λ=3nm, 1.83nm, 0.83nm).
An interesting region for experimental applications with radiation in the nanometer range is the water window centered at about $\lambda = 3$nm (see Table 4.2). At this wavelength, the maximum for the FEL parameter ρ occurs for $a_w = 1.41$ and decreases quite slowly, while the radiated power increases with the electron energy. Here we present FEL simulations for $E_e = 2.97$GeV and $a_w = 2.5$ (as in Figure 4.4), with the input signals listed in Table 4.1.

Figure 4.5 (see next page) shows the exponential SASE growth of the radiation along the undulator z coordinate[2] for short (A) and long (A') pulses. As shown in Eq. (B.63), it is possible to estimate the gain length L_g as well as the saturation length by evaluating the power growth rate at two different longitudinal positions $z_{1,2}$, or simply through its definition (2.3) in terms of the FEL parameter.
Saturation occurs at $z \sim 25m$ for Q=50pC (A' in Table 4.2, solid line in the plot), and occurs slightly later at $z \sim 30m$ in the other case.

[2]Power and Energy transported by the radiation are related as follows: $E =< P > L_{beam}/c$ where $L_{beam} \sim 13\mu m$ and c is the speed of light so that one could also plot the energy vs longitudinal coordinate.

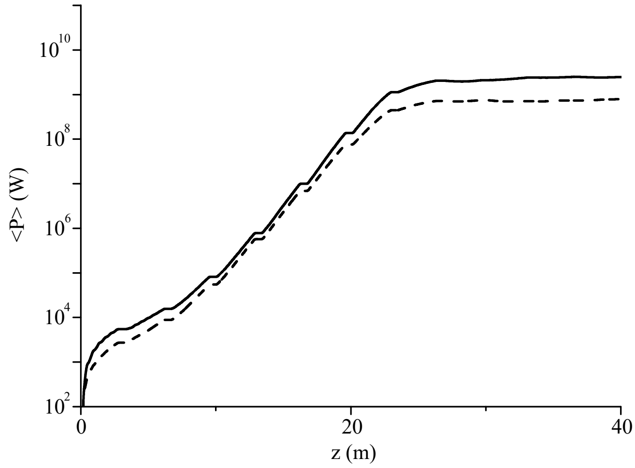

Figure 4.5: Average power (in logarithmic scale) vs undulator coordinate for $\lambda = 3$nm and $(\epsilon, \Delta E/E) = (0.5\text{mm mrad}, 2\text{x}10^{-4})$. Case A (dashed line) and A' (solid line) of Table 4.2. Resonant wavelength: $\lambda =$3nm

The spectral and temporal profiles of the FEL pulse at saturation ($z \sim 25$m) are plotted in Figure 4.6 for the two cases analyzed:

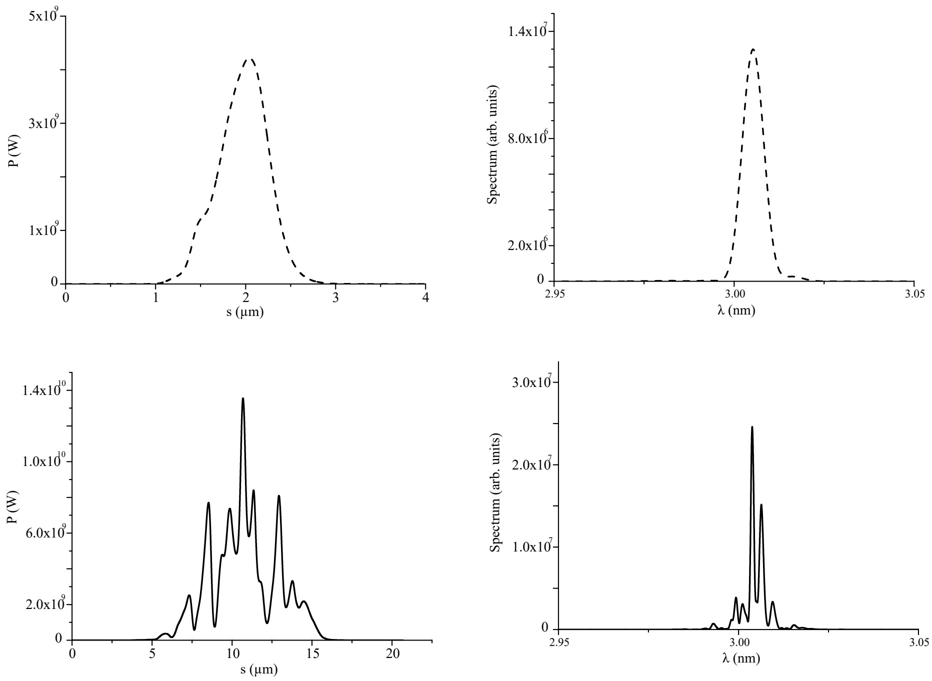

Figure 4.6: Power and spectrum at 25m for case A (dashed line) and A' (solid line). Resonant wavelength: $\lambda = 3$nm

As anticipated in the last line of Table 4.1, for Q=50pC (solid line in the plots) the radiation is in the standard SASE regime characterized by low longitudinal coherence degree. Furthermore, since the cooperation length (2.12) is shorter than $L_{beam}/2\pi$, the radiation is composed of several spikes both in time and soectral domain. However, the performance in terms of number of photons per shot produced is higher (6x10^{12} instead of 1.9x10^{11}) in this higher charge case.
By lowering the electron charge to 8pC (dashed line in the plots), we enter the single spike regime, with higher longitudinal coherence, short pulse duration and moderate photon flux. As shown in the correspondent plots of Figure 4.6, the radiation is single spiked, with phase almost constant on the whole shot.

As shown by the results and the example summarized in Table 4.2, the electron beam emittance and energy spread $(\epsilon, \Delta E/E)$ are crucial in the determination of the undulator working points and performances. In order to define the optimal characteristics of the electron beam (in the range allowed by the previous acceleration stages and summarized in Table 3.5) for the generation of radiation in the nanometer range, a parametric tolerance analysis of UliX1 was carried out. In particular we considered the more performant case with Q=50pC, varying the electron beam's emittance and energy spread in the intervals ϵ (mm mrad)$\in [0.25, 1.2]$ and $\Delta E/E$ $(10^{-4})\in [2, 9]$ leading to the level curves of Figures 4.7 and 4.8.

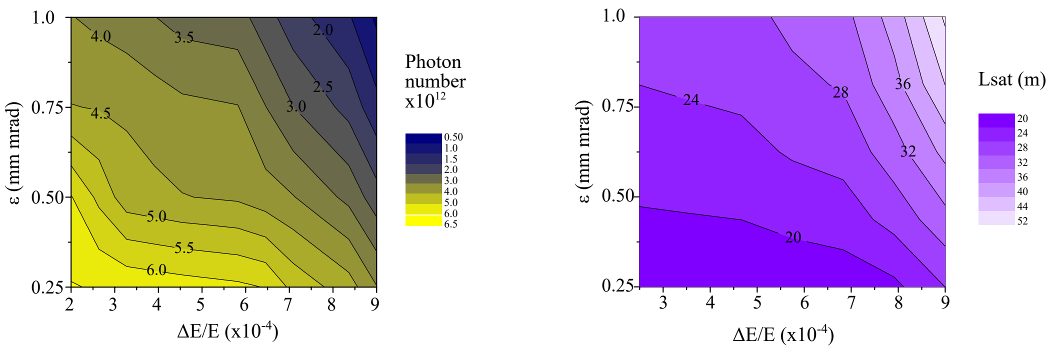

Figure 4.7: Photon number per shot (left panel) and saturation length (right panel) mapped onto the electron emittance and energy spread for the more performant beam of charge Q=50pC, for $\lambda = 3$nm

High photon numbers (N_{ph}/shot) and reduced gain and saturation lengths (L_g and L_{sat}) are required. These plots show that an increase in emittance and energy spread leads to a decrease in the number of photons produced. On the contrary, the simulation results show that the saturation length L_{sat} grows almost linearly with emittance and energy spread: assuming an average emittance of 0.5mm mrad, an energy spread larger than 0.6% can be destructive for the FEL and does not allow to reach saturation within 20m. This means that the needed undulator length should exceed the available space in the undulator room.

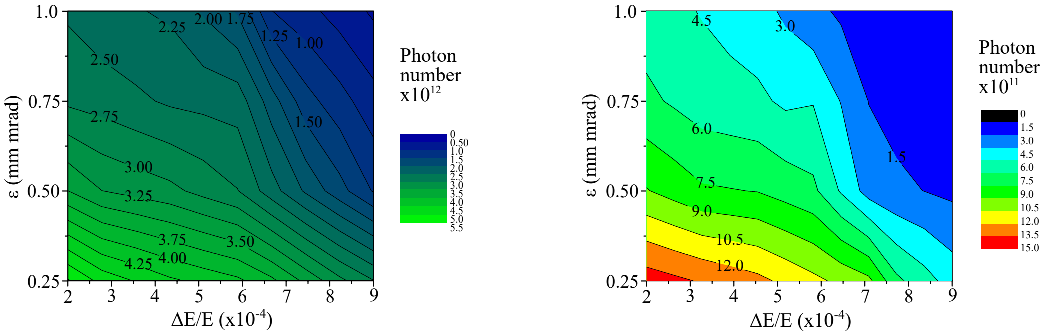

Figure 4.8: Photon number per shot in terms of emittance and energy spread of the 50pC electron beam entering UliX1 for $\lambda = 1.83$nm (left panel) and $\lambda = 0.83$nm (right panel)

According to our study and the capabilities of the machine, a physically possible and good FEL electron beam should have $(\epsilon, \Delta E/E) = (0.3 - 0.5 \text{ mm mrad}, 2 - 3\text{x}10^{-4})$. Table 4.3 summarizes the performance of the low energy line with such an optimal electron beam for the three wavelengths and in the two cases of Table 4.1:

Table 4.3: Simulations for UliX1 with $\lambda_w = 2.8$cm, $I_p = 1.6$kA and $(\epsilon, \Delta E/E) = (0.5, 2\text{x}10^{-4})$. Radiation properties are reported on average

Electron beam	A	D	E	A'	D'	E'
Energy E_e (GeV)	2.97	3.8	3.8	2.97	3.8	3.8
Q (pC)	8	8	8	50	50	50
Undulator	A	D	E	A'	D'	E'
a_w	2.5	2.5	1.5	2.5	2.5	1.5
Radiation	A	D	E	A'	D'	E'
λ (nm)	3	1.83	0.83	3	1.83	0.83
ρ_{1d} (x 10^{-3})	1.56	1.26	0.93	1.56	1.26	0.93
$L_g - L_{g3d}$ (m)	0.82-0.97	1.02-1.23	1.38-1.64	0.82-0.97	1.02-1.23	1.38-1.64
N_{ph}/shot (x 10^{11})	1.9	1.3	0.7	60	35	9.1

The maximum electron energy of 3.8GeV corresponds to a wavelength of 1.8nm at $a_w = 2.5$. To further shorten the wavelength, the undulator parameter a_w has to be decreased, producing at the same time degradation in efficiency (lower number of photons per shot) and gain length broadening (see Table 4.3 and Figure 4.9 in next page).

Furthermore, considering the single spike mode ($Q = 8pC$) a microscopic statistical analysis was performed varying the Hammersely base for loading the particle distribution, in order to evaluate the importance of electron's distribution in phase space.

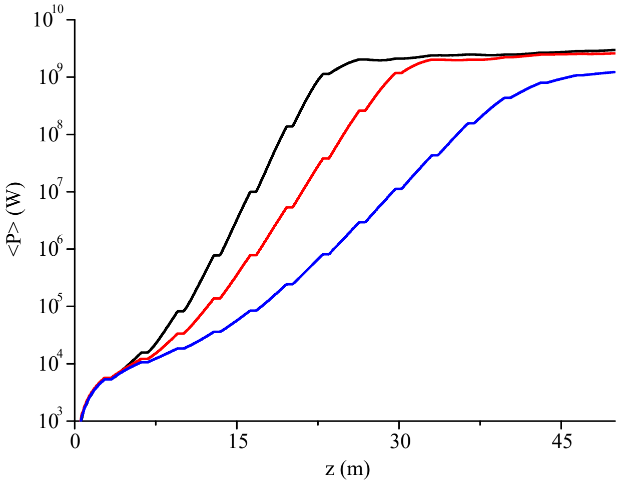

Figure 4.9: Power growth within UliX1 for $\lambda = 3nm$ (black line), $\lambda = 1.83nm$ (red line), $\lambda = 0.83nm$ (blue line). The electron beam here has $\epsilon = 0.5$mm mrad, $\Delta E/E = 2\text{x}10^{-4}$, $I_p = 1.6$kA, $Q = 50$pC (cases A', D', E' of Table 4.3). It is shown the degradation in efficiency and gain length broadening for decreasing wavelength

This analysis, together with the increase of the number of particles considered in the simulations (through the parameter NPART of GENESIS 1.3), has shown a negligible effect of both the beam microscopy and the numerical noise on the FEL performance.

4.1.2 High energy photon line

This section is devoted to the second MariX undulator line, conceived for high photon energy operation and named Undulator light infrastructure for X rays 2 (UliX2), which covers the wavelengths domain between 9$\AA$ and 1.5$\AA$ (2keV-8keV, see Figure 3.10).

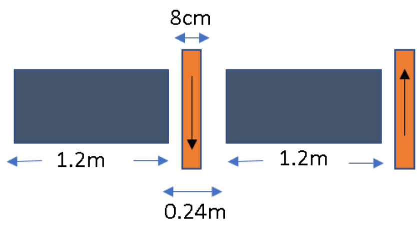

Figure 4.10: Periodicity module of the high photon energy line UliX2. The blue boxes represent the undulator modules ($L_{mod} = 1.2m$), separated by a 8cm long quadrupole

Similarly to UliX1 the basic operation mode is the SASE one. UliX2 is also designed

to work in seeded mode, although regular operations in seeded mode for hard X-rays are not so far foreseen in any X-FEL system. Different schemes (see Chapter 2) for improving the temporal and spectral properties of the radiation have been tested and are a real possibility.
The generation of radiation from 9$\mathring{A}$ to 1.5$\mathring{A}$, with 3.8GeV electron beam energy and a maximum peak field of 1T requires an undulator period of 1.2cm. As stressed in section 3.5.2, undulators with such period has not been constructed yet, but the SPARC undulator's period is 1.4cm and the technology improvements make this shorter period feasible in few years' time. Therefore, UliX2 is a short period undulator with period $\lambda_w = 1.2$cm, strength up to $a_w = 0.75$ and is about 60 meters long. A sketched-out picture of the periodicity module of the undulator system is presented in Figure 4.10, while Figure 4.11 depicts an example of the undulator sections and quadrupole positions in z (for a length z=70m):

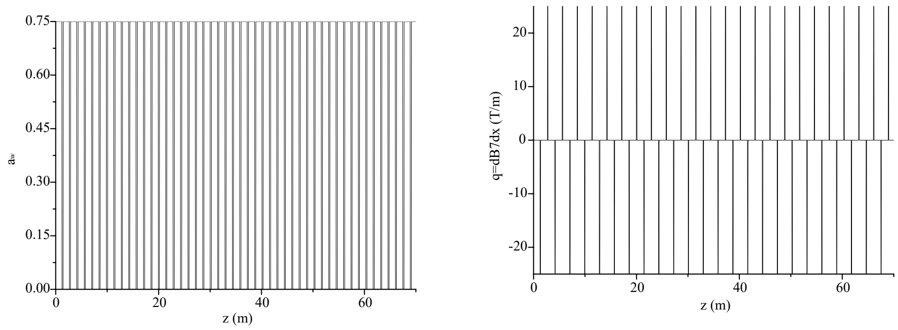

Figure 4.11: Undulator parameter a_w and quadrupole field as a function of the longitudinal position within UliX2

Each module is comprised of 100 periods and is 120cm long, while the total intra-module space length (including the quadrupole) is 24cm. The quadrupoles are 8 periods long and installed between two drift sections, 4 and 8 periods respectively long. The second drift should be long enough to allow for the installation of beam position monitors and some other diagnostics for radiation.
As shown in Figure 4.11, the quadrupole focusing strength was chosen to be of q=25T/m due to the higher performance in terms of number of photons produced (see Figure 4.12) and to the better matching of the beam.

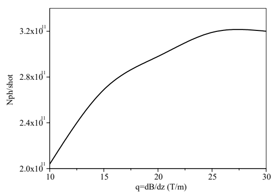

Figure 4.12: Number of photons in terms of quadrupole gradient for UliX2 with $\lambda = 7.8\mathring{A}$ and a reference beam with $(\epsilon, \Delta E/E) = (0.5\text{mm mrad}, 3\text{x}10^{-4})$

4.1.2.1 SASE mode

The Self-Amplified Spontaneous Emission mode is already validated in the sub-nm range of wavelengths in several FEL infrastructures: an X-ray pulse in the SASE regime can be generated in a single-pass not-segmented undulator. Monochromators or diamond/silicium mirror systems and gratings [101, 102] can be used for the spectral signal purification, while the statistical nature of the emission remains random.

As previously shown for the low energy FEL line UliX1 in Figures 4.7 and 4.8, we made the same tolerance parametric analysis for UliX2 at the resonant wavelength $\lambda = 7.8\mathring{A}$ (column G' of Table 4.4, see next page) to highlight the performances in terms of emittance and energy spread of the longer high charge electron beam of Table 4.1. Figure 4.13 shows the analysis and enforces our previous conclusion regarding the need of an electron beam with $(\epsilon, \Delta E/E) = (0.3 - 0.5\text{mm mrad}, 2 - 3\text{x}10^{-4})$ also for the high energy line.

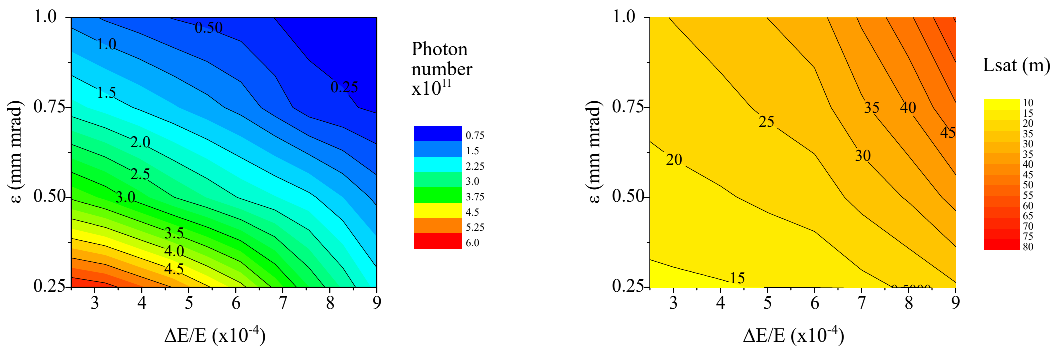

Figure 4.13: Photon number per shot (left panel) and saturation length (right panel) mapped onto the electron beam emittance and energy spread for an electron beam with Q=50pC, I_p=1.6kA and 1.78GeV energy emitting at $\lambda = 7.8\mathring{A}$

A set of typical UliX2 working points on the overall wavelength domain for the long signal of Table 4.1 (with a charge of Q=50pC), is presented in Table 4.4 (see next page) with a summary of the radiation properties. At the maximum electron energy of 3.8GeV, the minimum wavelength attainable with the maximum undulator magnetic field, corresponding to $a_w = 0.75$, is about $\lambda = 1.7\mathring{A}$. Operations at lower wavelengths can be performed by opening the undulators gap, thus decreasing a_w down to 0.6. The efficiency decreases, as can be seen from the data of column L' obtained with $a_w = 0.64$, for a wavelength of $\lambda = 1.5\mathring{A}$. By further lowering the FEL parameter, a minimum value of $1.3\mathring{A}$ may be reached.

Table 4.4: Simulations for UliX2 with λ_w = 1.2cm, Q = 50pC and I_p = 1.6kA. Radiation properties are reported at $L_{und} \sim$ 60m

Electron beam	F'	G'	H'	I'	J'	L'
Energy E_e (GeV)	1.6	1.78	2.33	2.4	3.2	3.8
ϵ (mm mrad)	0.5	0.5	0.5	0.4	0.4	0.4
$\Delta E/E$ (x 10^{-4})	2	2.5	2	2.5	3	2.5
L_c (μm)	0.19	0.16	0.13	0.13	0.09	0.08
Undulator	F'	G'	H'	I'	J'	L'
a_w	0.69	0.75	0.81	0.75	0.75	0.64
Radiation	F'	G'	H'	I'	J'	L'
λ ($\AA$)	9	7.8	4.77	4.25	2.4	1.5
ρ_{1d} (x 10^{-3})	0.75	0.79	0.56	0.52	0.42	0.3
$L_g - L_{g3d}$ (m)	0.73-0.83	0.69-0.83	0.98-1.2	1.05-1.11	1.3-2.12	1.81-3.3
N_{ph}/shot (x 10^{11})	4.2	3.5	1.99	0.49	0.95	0.013

Linear spectroscopy experiments can be performed with radiation in the wavelength range between 5$\AA$ (2.5keV) and 2.5$\AA$ (5keV), and with moderate flux per shot at high repetition rate (cases H'-J' in Table 4.4). In order to define the optimal beam for this purpose, the radiation parameters for emission at $\lambda = 4.77\AA$ are listed in Table 4.5, including a comparison between the two possible input signals of Table 4.1.

Table 4.5: Simulations for UliX2 in the linear spectroscopy range, with $\lambda = 4.77\AA$, λ_w = 1.2cm, a_w = 0.81, E_e = 2.33GeV, I_p = 1.6kA and $(\epsilon, \Delta E/E) = (0.4\text{mm mrad}, 2\text{x}10^{-4})$. Radiation properties are reported at the nominal undulator length $L_{und} = 60m$

Electron beam	H	H'
Q (pC)	8	50
L_{beam} (μm)	1.5	9.4
L_c (μm)	0.135	0.135
Radiation	H	H'
ρ (10^{-3})	0.56	0.56
$L_g - L_{g,3d}$ (m)	0.98	1.04
N_{ph}/shot (x 10^{10})	1.2	6.4
Divergence (μrad)	4	5
Size (μm)	55	60
bw (%)	0.8	1
N_{ph}/s	1.2x10^{16}	6.4x10^{16}

Figure 4.14 (see next page) shows the power growth along the undulator for the cases of Table 4.5 (E_{ph}=3keV). The radiation reaches the onset of saturation in about 50m, but continues slightly to increase.

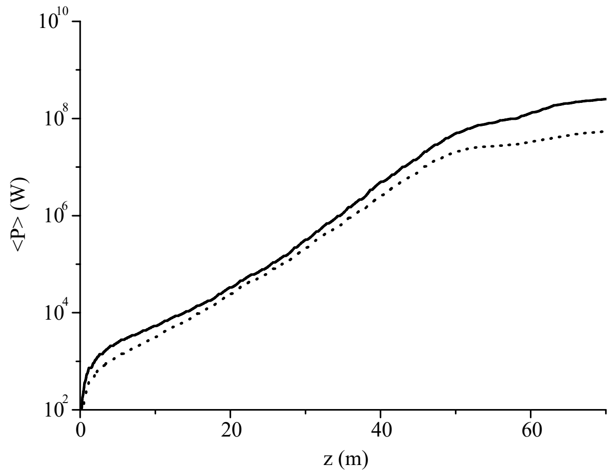

Figure 4.14: Average power $\langle P \rangle$(W) in log-scale vs undulator coordinate z(m). Case H (short pulse, dotted line) and H' (long pulse, solid line) of Table 4.5. Resonant wavelength: $\lambda = 4.77\mathring{A}$

Figure 4.15 shows the spectral and temporal profiles of the FEL pulse for the two cases H and H' at z=60m.

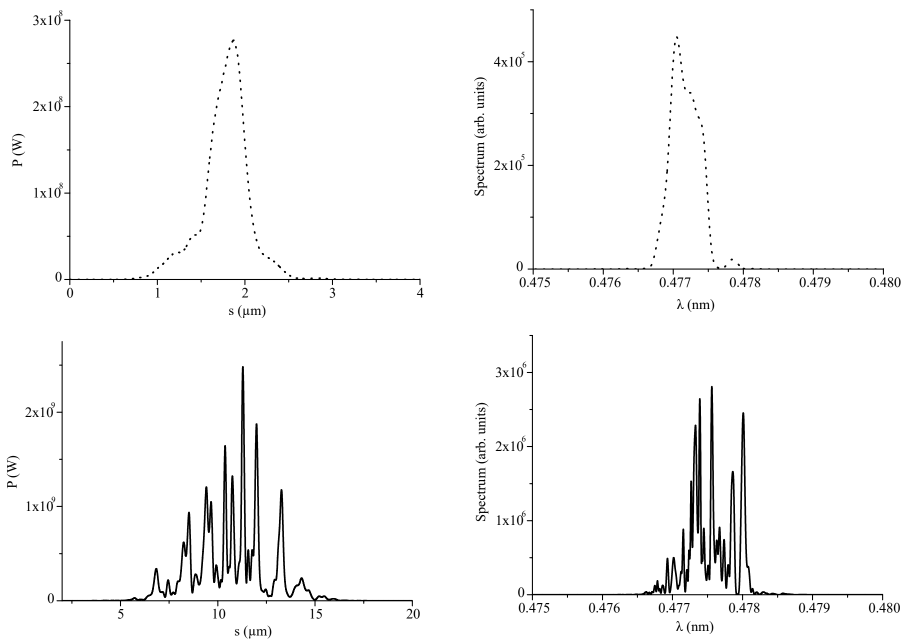

Figure 4.15: Power and spectrum at $L_{und} = 60m$ for case H (dotted line) and H' (solid line) of Table 4.5

In the long pulse case (H') the SASE fluctuations dominate pulse and spectrum and the rms length of the radiation pulse is about $2\mu m$ (7fs), similar to the electron bunch duration; on the contrary, in the short pulse case (H) the radiation exhibits only one spike with rms length of 1.3fs, with power and phase fluctuations occurring from shot to shot. For cases J'-L', single spike operation is not permitted due to the shorter cooperation length L_c.

Lowering the FEL parameter to 0.64, the shortest wavelength achieved with acceptable efficiency in the MariX FEL is about $1.5\mathring{A}$ (working point L' of Table 4.4), which allows crystallography and single shot imaging experiments. The radiation growth is shown in Figure 4.16. A 60-65m long undulator is not sufficient to reach saturation and therefore the flux is quite low, reaching only a few 10^9 photons per shot (see Table 4.4), a factor 100 times less than other FEL systems operating in this hard X-ray regime. However this is an interesting regime because of the number of photons per second (10^{15}), a factor 10 larger than the LCLS data.

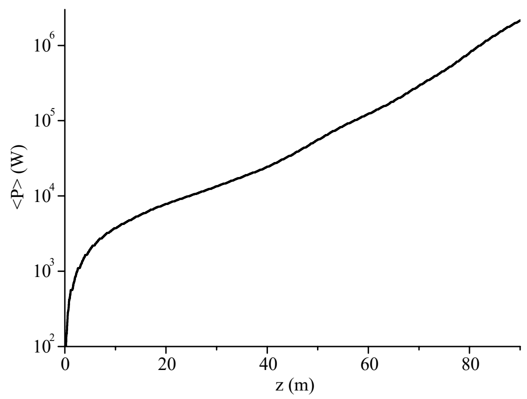

Figure 4.16: Average power $\langle P\rangle$(W) in log-scale vs undulator coordinate z(m). Case L' of Table 4.4. Resonant wavelength $\lambda = 1.5\mathring{A}$

The SASE performances of the two FEL lines with the ideal optimized beam are summarized in Table 4.6:

Table 4.6: Summary of the SASE performances for the two FEL lines with the optimized electron beam having I_p=1.6kA, $\epsilon = 0.4$mm mrad and $\Delta E/E$=3x10^{-4}

Parameter	**UliX1**	**UliX2**
Photons/shot (10^{11})	17-1.2	2.4-0.025
Bandwidth (0.1%)	2.1-0.7	2.3-3
Pulse length (fs)	3-10	1-7
Pulse divergence (μrad)	6-50	5-45
Photons/s (10^{17})	17-1.2	2.4-0.025

This preliminary analysis show the capabilities of the low and high energy lines, and demonstrate their outreaching expected performances, but do not pretend to be exhaustive. For example, as pointed out in the last section of chapter 3, the use of more advanced techniques, such as tapering in the undulator, could further improve the FEL performance.

4.1.2.2 Seeded mode

The MariX high energy photon line (see sections 3.4 and 3.5) has not been only designed for SASE operation. An alternative option for UliX2 is the seeded operation, highly requested from users and whose advantages and limits have been pointed out in Chapter 2.

An important issue concerning the study of a possible seeding technique is given by the spatial constraints, which put a limit on the overall dimension of the machine and of the FEL lines as well.
Moreover in any seeding configuration, a contrast ratio of $10^2 - 10^3$ between the seed intensity and the background noise is requested for an efficient seeding source, thus setting a limit on the shortest wavelength achievable: in fact seeding sources tipically have lower efficiency in terms of output power at shorter wavelengths and the shot noise power grows up according to the scaling law

$$P_{sn} = \omega_0 \rho^2 \gamma m c^2 \tag{4.2}$$

As shown in the next sections, the relatively low value of electron beam energy (see Table 3.5) allows to reduce the detrimental effect of the shot noise level on the seeded emission. Another limitation in going towards sub-nm wavelengths with seeded FELs is due to the lack of high-power, narrow-bandwidth laser sources below 200nm. In order to overcome these problems, other solutions and advanced schemes have been studied throughout the last decade (see in particular section 2.3).

One promising possibility for generating ultrashort pulses of coherent radiation in the XUV (30-300 eV) and soft X (300-3000 eV) regions of the spectrum, suitable to seed short wavelength Free Electron Lasers is to use the high harmonic generation (HHG) scheme starting from a ultrashort high-peak power laser (see section 2.3). Through this method, the generation in gas of the 59th (13.5nm) up to the 63rd (12.6nm) harmonic of a Ti:Sa pump laser[3] (800nm wavelength) has been demonstrated (see

[3] The most suitable sources for this scope are the Ti:Sa lasers, for their characteristic in terms of energy and pulse shortness (fs-class). However, these lasers do not provide intense radiation below 120nm of wavelength. The main component of the seed generation system is tipically a regenerative amplifier that can be seeded by the same oscillator driving the photocathode amplifier [12]. This solution may ensure sufficient synchronization between the seed laser and the electron bunch. The techniques required to inject the produced HHG radiation in the FEL amplifier have been analyzed [5, 13]. For example, the injection of a seed may be realized with a small chicane deviating the electron beam path, allowing to set in line mirrors for a proper optical matching (with a hole in

Figure 2.3 and 2.4). The energy generated in both schemes is around 3-15nJ and the time lengths of the single radiation pulse are tens of femtoseconds. These values, if reproducible, could make a seeding scheme with HHG on MariX feasible.
For these reasons, the first technique to be considered for MariX high energy photon line is the High Gain Harmonic Generation scheme (see section 2.4) seeded by high harmonics of a pump laser, already achieved at wavelength less than 20nm in He and Ne with pump lasers of 1-100mJ.

A further innovation expected from MariX facility is therefore a truly coherent photon beam at 100 kHz, that can be obtained with the cascaded High Gain Harmonic Generation (HGHG) fresh bunch technique (qualitatively described in section 2.4, see Figure 2.5). The SASE intrinsic pulse-to-pulse jitter will be substantially eliminated, as well as the reduced pulse-to-pulse intensity fluctuations, thus approaching, at X-ray energies, the unique performance of FERMI@Elettra.

HGHG Cascade mode

The most studied seeded mode for MariX throughout this work is an HGHG cascade (described in section 2.4), with the goal of increasing the frequency up-conversion of seeded FELs.
The first critical step in the definition of the seeding scheme is the choice of the seeding source, including its wavelength and its energy. A seed pulse having a Gaussian temporal profile in power[4] and 13.6nm wavelength was considered, which corresponds to the 59th harmonic of a Ti:Sa laser pulse: this last choice is due to the existence of experimental studies of laser harmonic generation in gases which extends up to 12nm, and also to the existence of multi-layer mirrors (such as molybdenum-selenium Mo/Si [101,103]) operating at this wavelength with up to 75% reflectivity and higher, opening the way to an FEL oscillator as seeding system (see section 4.3.1) and allowing the transport of the seed signal to the undulators if additional paths for the gas chamber are needed.

Regarding the required initial seed energy, it is possible to evaluate the shot noise power in Eq. (4.2) with the used electron beam parameters and for the desired resonant frequency of operation. Radiation pulses of 20nJ down to 10nJ energy are close to the state of the art and have been tested with the cascade initial stage. This choice is non trivial, since it influences the output power and stability, and the amplified harmonics intensity is also affected.

---

the input mirror to avoid electron beam bends), or by producing the harmonics directly on the beamline [5].

[4]In general the seed power can be indicated as $P = P_0 e^{-\frac{(x-x_0)^2}{2\sigma_s^2}}$ where P_0 is the peak power, x_0 the seed centroid and σ_s its FWHM size.
The seed energy E and peak power are related to its rms size σ_s by $\int P\mathrm{d}t = E$ which gives $P_0 = Ec/\sqrt{2\pi}\sigma_s$, where c is the speed of light in vacuum.

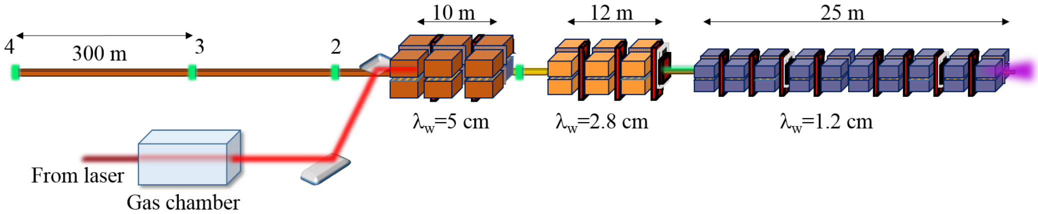

Figure 4.17: Segmented undulator scheme for a three-stage cascade with HGG as seed. A configuration of a first modulator with a single module (10m long) and a second modulator composed of three modules ($\sim$ 12m long), followed by the conventional UliX2 as radiator ($\leq$ 25m long), was found to be optimal in terms of coherence and photon number

Figure 4.17 presents a possible sequence of undulators for cascaded operation, made of two longer period modulators (5cm and 2.8cm respectively, and whose length is indicated in Figure) and the final radiator of period 1.2cm. The segmentation of the two modulators was studied by means of FEL simulations, and the best configuration is the one reproduced in Figure 4.17, with the first un-segmented modulator and the second one composed of three sections, while the radiator is a portion of UliX2 itself (see section 4.2). The length of the entire scheme should be ideally equal or less than the UliX2 60 meters, with the length for the single undulators to be adjusted and defined according to the simulated results, while the space required for the gas chamber and the laser path should not enlarge the overall longitudinal size.

According to Liouville's theorem, the required energy spread to bunch at the n^{th} harmonic is $\sigma_{induced} \approx 2n\sigma_{initial}$, thus increasing with the harmonic number. Given the high harmonic number needed to reach short wavelengths by up-shift frequency conversion, the studied cascade makes use of the fresh-bunch injection technique: a dispersive section between the different sections of the cascade delays the electron beam by few femtoseconds, allowing the radiation field to seed a fresh unused portion of the electron bunch, for which the energy spread has not been heated by the previous light-electron interaction.
The three-stage cascade works as follows. A first modulator[5] with $\lambda_{w1} = 5cm$ amplifies the seed at $\lambda_1 = 13.6nm$ together with its odd harmonics (see section 2.1.2, the even harmonics are also produced but are distributed in the transverse direction, thus off-axis, and their coherent emission is suppressed). In this first section, the radiation seed from HHG is injected and the consequent bunching of the electron forced by the laser field allows to accelerate the laser process and to have a coherence zone equal to the temporal length of the seed pulse. The second modulator ($\lambda_{w2} = 2.8cm$ as UliX1) amplifies the n_1^{th} harmonic producing coherent signal at $\lambda_2 = \lambda_1/n_1^{th}$. In the last passage, the n_2^{th} harmonic of λ_2 is amplified in the radiator, producing a coherent radiation pulse at $\lambda_3 = \lambda_2/n_2^{th} = \lambda_1/(n_1^{th}n_2^{th})$. The harmonics

[5]To be resonant at 13.6nm, the resultant undulator parameter a_w of the first modulator is fully compatible with the specifications of the given undulator.

need to be extracted from the different modules at a certain distance such that their temporal profile is not too much distorted from the FEL interaction, and the energy transported has to be comparable to the one of the input seed signal. Furthermore, the pulse energy seeding each step of the cascade scheme needs to be $10^3 - 10^4$ times higher than the electron beam noise level, estimated through Eq. (4.2).
The seeding technique based on High Gain Harmonic Generation permits to produce radiation with the same energy level as the SASE mode, but with full temporal coherence and small energy fluctuations. In this configuration, the external laser pulse, or its harmonics, encodes its coherence on the FEL radiation and determines the temporal and spectral distribution of the output radiation[6].

To define the important characteristics of the seed, and their influence on the cascade process, a SPARC-like [50] cascade was considered first, whose final wavelength is of the order of few μm so that the process was faster to simulate. The performances in terms of number of photons are not so much influenced by the seed energy, while the saturation lengths increase for lower energies: it's better to decrease the energy and increase the seed power, and to shorten it.
High-Order harmonics of an ultrashort laser pulse, as the Ti:Sa laser, show high temporal and spatial coherence and are characterized by a time duration shorter than that of the driving source[7]. Exploiting HHG for FEL seeding requires powerful laser sources and suitable techniques to boost the XUV emission to the required peak powers. Though substantial energy from this type of source is available in the VUV, no experiments have been performed so far in the EUV-soft-hard X-rays range.

The matching of the electron beam in the cascade configuration is performed backwards starting from the radiator, keeping the quadrupole strength low and the beam size large. Table 4.7 shows wavelengths and harmonics in the various segments for few electron energies. The electron beam used is the one considered in the previous sections, having I_p = 1.6kA, Q=50pC and whose current profile is shown in Figure 4.1.

Table 4.7: Example of possible cascades and frequency up-shift conversions with resonant wavelengths between 3.88$\mathring{A}$ and 9$\mathring{A}$

	Energy $m_e c^2 \gamma$ (GeV)	λ_{w1} (cm)	a_{w1}	λ_1 (nm)	n_1	λ_{w2} (cm)	a_{w2}	λ_2 (nm)	n_2	λ_{w3} (cm)	a_{w3}	λ_3 (nm)
a)	1.6	5	2.08	13.6	5	2.8	0.95	2.72	3	1.2	0.69	0.9
b)	2.3	5	3	12.7	5	2.8	1.6	2.4	5	1.2	0.81	0.48
c)	2	5	2.7	13.6	5	2.8	1.4	2.72	5	1.2	0.62	0.54
d)	2.4	5	3.31	13.6	7	2.8	1.43	1.94	5	1.2	0.65	0.38

[6]The flexibility offered by the variable gap configuration of the MariX undulators (see section 3.5.2) makes the MariX FEL layout suited for a large number of experiments

[7]XUV pulses with durations ranging from 8 to 13 femtoseconds have been generated by spectral selection of a single harmonic with a suitable time-compensated monochromator [81].

HGHG cascades were performed at FERMI [104] for wavelengths in the mid-infrared and VUV range. The implementation of this scheme in the hard X-ray spectral range, however, has still to be proven: due to the non trivial physical task, we first consider the three-stage cascade starting from 13.6nm and arriving, through a $5x3$ conversion, to 0.9nm (case a of Table 4.7).

The Seeded FEL performance has been verified in order to quantify the effect of the seed, with respect to SASE, in terms of:

- Temporal coherence enhancement indicated by the reduction of the number of spikes in the FEL spectrum and in the temporal profile of the radiation pulse.
- Increase of the FEL power and of the number of photons per pulse
- Reduction of the saturation length.

a) Cascade 5x3: $9\AA$ **wavelength**

The seed signal considered for this cascade, which is ideally the 59th harmonic of a Ti:Sa laser pulse produced from high harmonic generation in gas, with its main characteristics, is shown in Figure 4.18:

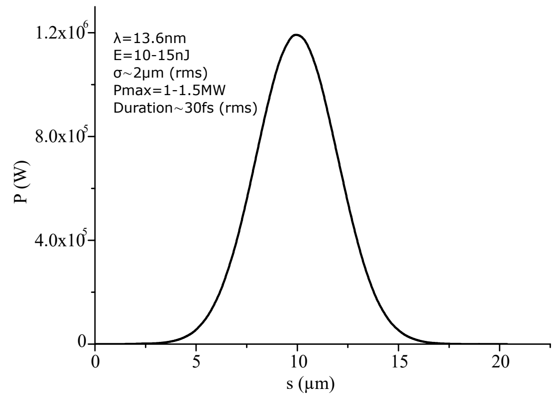

Figure 4.18: Temporal profile of the seed signal for the 5x3 cascade. The characteristics of the seed are here listed and have been selected because of the efficiency in the amplification of radiation starting from the electron beam of Figure 4.1, with Q=50pC and I_p=1.6kA. Energies of 10nJ up to 20nJ were found to be appropriate

The first stage of the cascade (see Table 4.7a) is tuned at 13.6nm; considering the electron beam energy of 1.6GeV and a typical FEL parameter of $\rho \sim 10^{-3}$, from Eq. (4.2) one finds a power of $P_{sn} \sim 35$W associated with the electrons shot noise, meaning an equivalent energy of $E_{sn} \sim 0.001$nJ (10^4 smaller than the one chosen for the seed) for the electron beam of rms length $10\mu m$ (high charge working point of Table 4.1).

The power growth for the fundamental frequency and its first odd harmonics within the two modulators and the radiator is shown in Figure 4.19, where we note the difference with respect to SASE growth (see Figure 4.5 for example) and the initial part characterized by the so-called "coherent spontaneous emission".

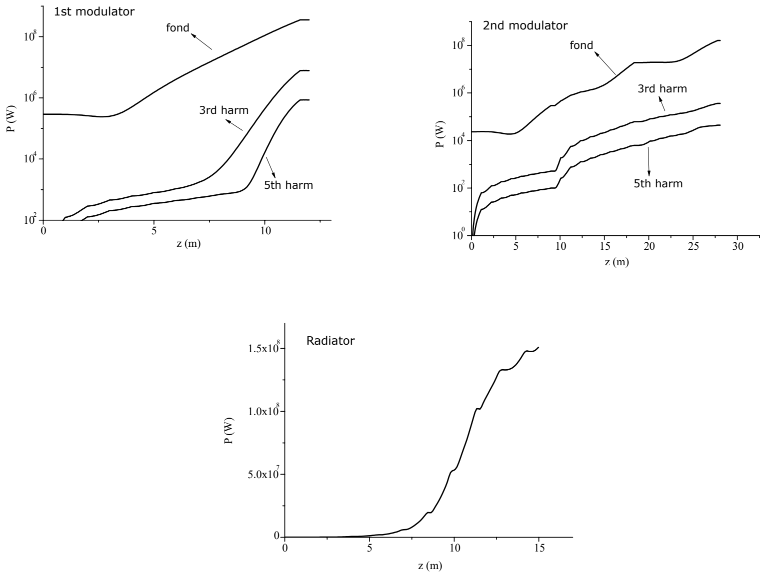

Figure 4.19: Radiation growth on the fundamental and on the lowest odd harmonics in the modulators (upper plots) and in the radiator (lower plot). Final wavelength is 0.9nm

In this particular cascade configuration, we extract the 5th harmonic ($n_1^{th} = 5$) after about z=10m from the first modulator, and the 3rd harmonic ($n_2^{th} = 3$) at $z \sim 20$m from the second modulator, obtaining a 0.9nm wavelength coherent pulse which can be extracted from the radiator at $z \sim 10$m, reducing the needed space for the radiator. The total length of the undulators' sequence is therefore 40 meters, leaving enough space for chicanes and radiation diagnostics.

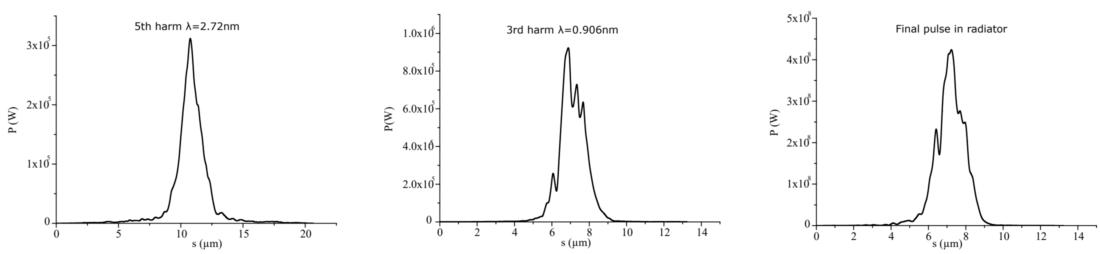

Figure 4.20: Temporal profiles of the 5th harmonic extracted from modulator1 (left), 3rd harmonic extracted from modulator2 (middle) and the final radiation pulse at z=10m in the radiator (right). The wavelength of the extracted pulses is indicated in each plot

The temporal profiles of the harmonics extracted from the two modulators and the final coherent FEL pulse extracted from the radiator are reported in Figure 4.20. Thanks to the fresh-bunch injection, as shown in Figure 4.20, the harmonics extracted at each step were enough cleaned to be used for the subsequent seeding of the next step. Besides, the extracted harmonics' energy (about 12nJ for the third one and 30nJ for the fifth one) are sufficient (about 10^3 times higher than the shot noise level of $E_{sn} \sim 0.005$nJ for the fifth harmonic and 0.015nJ for the third one) to overcome the electrons' noise level.

The produced pulse in the radiator (right panel of Figure 4.20) remains stable and undistorted (coherent) for 10 meters, and its coherence may be enhanced by extracting the third harmonic at an higher energy level, if the pulse stability is still satisfactory. At $z \sim 10$m, taking into account the electron beam length of $\sim 20\mu m$, the final yield of 10μJ of radiation corresponds to 10^{10} photons per pulse and up to 10^{16} photons per second. The simulated performances are summarized in Table 4.8:

Table 4.8: Radiation characteristics of the HGG seeded cascade. The repetition rate of the source is 1 MHz.

λ (nm)	0.9	E (μJ)	5-10
N_{ph}/shot	10^{10}	N_{ph}/sec	10^{16}
bw (%)	0.07	Length (μm)	2-3
div (μrad)	35	size (μm)	75

If a more Gaussian-like output pulse is desired, it is possible to extract the radiation few meters earlier, obtaining a better final pulse-shape with a slightly reduced number of photons produced: the primary reason for seeding is the pulse stability indeed.

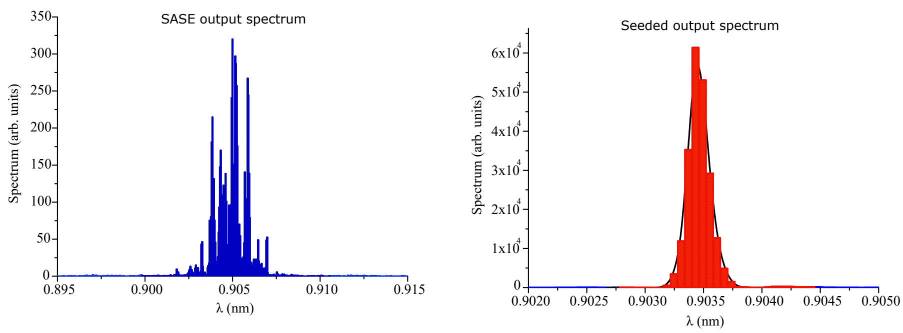

Figure 4.21: Spectral profile of the SASE pulse from UliX2 operation at $\lambda = 0.9$nm (case F' of Table 4.4, in blue) at z=10m and of the pulse extracted at the end of the cascade (in red). In order to calculate the degree of coherence the spectrum is plotted in terms of frequency

The performances of this cascade (listed in Table 4.8) should be compared with its self-amplified spontaneous emission counterpart, which is column F' of Table 4.4, which gives a number of photons produced only one order of magnitude higher. One big advantage of the cascaded operation is related to the coherence degree of the output pulse with respect to the SASE case.

The coherence time of the output pulse, in general, can be calculated by fitting the spectral profile of the pulse (shown in Figure 4.21 for the pulse from SASE amplification at z=10m within UliX2 and the pulse extracted after 10m of radiator) with a Gaussian function and estimating the inverse of the FWHM, which is 13fs for the pulse extracted from the radiator, and 1.3fs (one order of magnitude lower) for the pulse extracted from UliX2 (case F' of Table 4.4).

Through the HGHG fresh bunch cascade, we obtained a coherent and stable pulse to be used by MariX users for bulk photoemission to become highly efficient probe of matter at the nanoscale but in bulk environments, like buried interfaces of interest in materials science, in-vivo biological samples or catalysers at work.
According to the presented results, the radiator can be limited to be 30 meters long. If the radiation is extracted after few meters of radiator, it gives a lower number of photons but is even more stable.

b) Cascade 5x5: $4.8\mathring{A}$ wavelength

The electron beam considered for this cascade has a peak current of 1.8kA and a rms length of about $13\mu m$ in the longitudinal direction, with a Gaussian longitudinal current profile as the one shown in Figure 4.1. The seed signal considered for this cascade is ideally the 63rd harmonic (12.7nm) of a 800nm Ti:Sa laser pulse produced from high harmonic generation in gas, and has the same characteristics of the seed shown in Figure 4.18.
In this case the shot noise energy level (see Eq. (4.2)) in the first stage amounts to $E_{sn} \sim 0.001$nJ, so that the seed energy is enough to overcome the problem.

The power growth of the odd harmonics used for the cascade and the final wavelength in the radiator is shown in Figure 4.22:

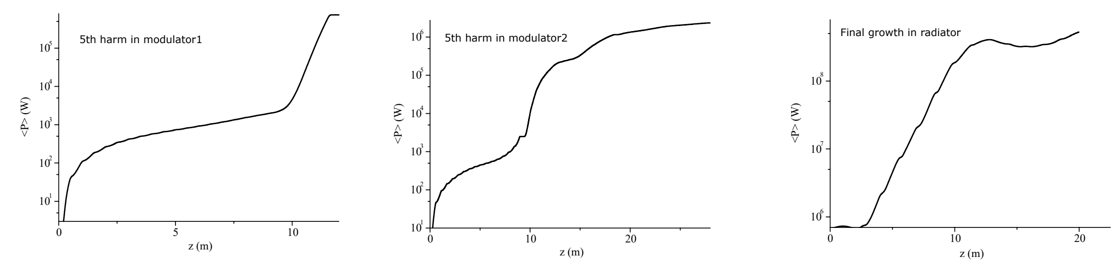

Figure 4.22: Radiation growth on the used odd harmonics in the modulators (first two plots from left) and on the fundamental in the radiator (right panel). Final wavelength is 0.48nm

As in the 5x5 cascade, we considered the fresh bunch injection technique. In this case we extract the 5th harmonic ($n_1^{th} = 5$) at the end of the first modulator (z=12m), and the 5th harmonic ($n_2^{th} = 5$) at $z \sim 17$m from the second modulator, obtaining a coherent pulse at $4.8\mathring{A}$ which can be extracted after about $\sim 10 - 12m$ of radiator. The temporal profiles of the harmonics extracted from the two modulators and the final coherent beam extracted from the radiator are reported in Figure 4.23. As in the case of the previous cascade, the harmonics are extracted when their energy level (30nJ and 50nJ respectively) is about three orders of magnitude larger than the shot noise level, which now corresponds to $E_{sn} \sim 0.01$nJ for the second stage tuned at 2.52nm, and 0.06nJ for the third stage tuned at $0.5\mathring{A}$.

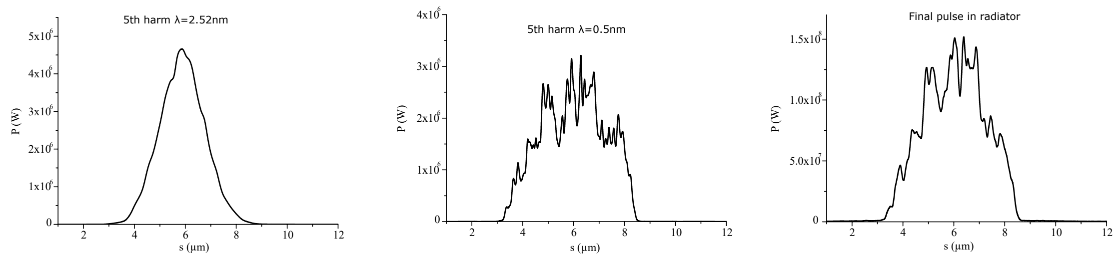

Figure 4.23: Power shape of the 5th harmonic extracted from modulator1 (upper left), 5th harmonic extracted from modulator2 (in the middle) and the final radiation pulse at z=10m in the radiator. The wavelength of the extracted pulses is reported in each plot

The output pulse temporal profile is less clean than the one obtained from the previous cascade (see Figure 4.20 right), because of the shape of the 5th harmonic from the second modulator and of its slightly lower contrast ratio to the electron shot noise with respect to the previous stage, but the broader signal results in a more strict and clean spectrum, as shown in Figure 4.24.
The produced pulse in the radiator (right plot in Figure 4.23) remains stable and undistorted for 10 meters. At $z \sim 10$m, taking into account the electron beam length of $\sim 13\mu m$, it brings to 10^{10} photons per pulse and up to 10^{16} photons per second as the 0.9nm wavelength cascade.

Figure 4.24 (see next page) plots the output spectrum compared to the one of Figure 4.15 (bottom right panel), which shows the spectrum of column H' of Table 4.5, the self-amplified spontaneous emission counterpart of the result analyzed here. The number of photons produced is the same, even if they are now coherent (the coherence time is increased by almost one order of magnitude).

Following previous studies on harmonic generation in gas and the generation of short wavelength seed signals, the results obtained with the proposed seeded operation demonstrate the production of statistically stable and totally coherent X-ray pulses at high repetition rate, but the method needs to be experimentally tested and optimized. The extraction from the different sections depends on the desired stabil-

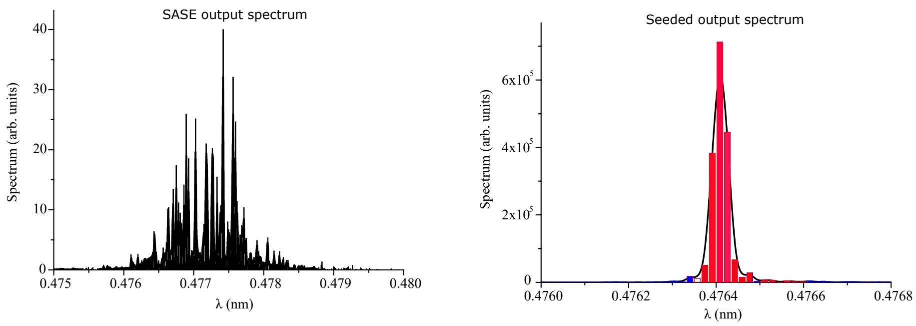

Figure 4.24: Spectrum of the SASE pulse from UliX2 operation at $\lambda = 4.8\mathring{A}$ (case H' of Table 4.5) at z=10m (in blue) and of the pulse extracted at the end of the cascade (in red)

ity and coherence of the pulse, and this is also dictated by experimental applications. Moreover some difficulties may occur in the production and transport of the HHG toward the undulator, as for example the overlapping with the electrons, the temporal synchronization, attenuation of the HHG signal due to the transport optics. Of course, this would require at least knowledge acquisition on the topics of HHG generation. As regards the temporal and spatial coherence level of the produced pulses, it will need to be measured experimentally once the scheme is tested, for example by means of interferometric experiments or speckle-based diffraction studies.

4.2 Simulations with the MariX real beam

The MariX beam after the arc is shown in Figure 3.8. Basically due to its particular longitudinal phase space and high energy spread (see Figure 4.7 for example), this electron beam did not reveal itself as a good candidate for FEL operation, resulting in very low amplification and other correlated problems.

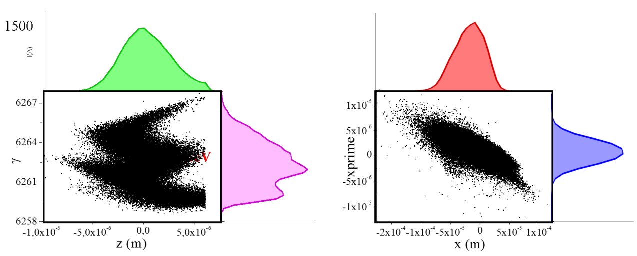

Figure 4.25: Longitudinal (left) and Transverse (right) phase space of the electron beam before the undulator

In order to determine the relative effects and benefits from high peak currents or low energy spread and to optimize the beam, few simulations were performed with an ideal Gaussian beam having 800A or 1.6kA peak currents and 0.2% or 0.4% of relative energy spread. This analysis showed that high current intensities and low

relative energy spreads have the same effect on the FEL performance, remarking the need of an electron beam having a lower energy spread than the one of the beam of Figure 3.8.
With the particle tracking code ELEGANT, an electron beam with parameters very similar to the nominal/optimal ones was obtained. Its longitudinal phase space is shown in Figure 4.25 (left), and can be considered the result of the matching line operation to the electron beam in Figure 3.8.

The electron beam phase space has been rotated and stretched in the transverse x direction, keeping the emittance constant (with the products between coordinates and associated momentum constant), and the longitudinal phase space tails have been cutted. This kind of beam modification may be obtained by closing the dispersion.
The electron beam parameters are summarized in Table 4.9:

Table 4.9: Real MariX electron beam parameters for FEL operation

Electron beam	Units	
Energy E_e	GeV	3.2
Charge Q	pC	30
Peak current I_p (slice)	kA	1.5
Norm. emittance ϵ (slice)	μm	0.33 (x) 0.2 (y)
Energy spread $\Delta E/E_e$ (slice)	10^{-4}	3.6
rms length in z-x-y	μm	20.6-34.5-14.5

Its longitudinal current profile is shown in Figure 4.26.

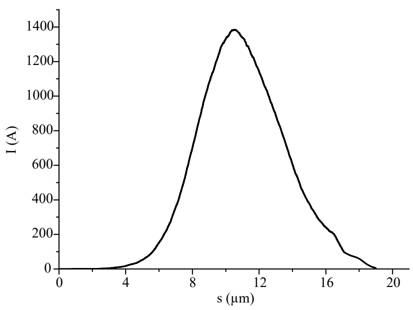

Figure 4.26: Longitudinal current profile of the real beam entering the undulators

For both the FEL lines, the performances starting from this real beam have been compared with the results obtained with an ideal beam (see Figure 4.1) similar to the real one, having the parameters of Table 4.9.

4.2.1 Low energy photon line

We first simulated the performances of the low energy photon line UliX1: due to the electron beam energy of 3.2GeV, the only achievable wavelength at the maximum undulator field $a_w \sim 2.5$ is $\lambda = 3$nm, while lower wavelengths (such as $\lambda = 1.8$nm) can be reached with reduced efficiency by lowering a_w down to 2.

The simulations for $\lambda = 3$nm are summarized in Table 4.10 (see next page). The real case is in good agreement (same orders of magnitude for the main properties) with the results and radiation properties obtained with the ideal beam.

Table 4.10: Comparison between simulations for UliX1 ($\lambda_w = 2.8$cm, $a_w = 2.72$) with the real and ideal beam emitting at $\lambda = 3$nm. The electron beam parameters are the one of Table 4.9 and radiation properties are reported at the nominal undulator length $L_{und} = 35$m

	Real beam	**Ideal beam**
ρ (10^{-3})	0.93	0.93
L_c (m)	2.05	2.05
$L_g - L_{g,3d}$ (m)	0.59-0.74	0.59-0.74
N_{ph}/shot (x 10^{12})	1.53	2.25
N_{ph}/s	1.53x10^{18}	2.25x10^{18}
Divergence (μrad)	18	14
Size (μm)	60	55
bw (%)	0.2	0.1

The spectral profiles at the end of the undulator for the two cases of Table 4.10 are reported in Figure 4.27, from which it's possible to note the similarity between the two cases in terms of spectral purity and bandwidth.

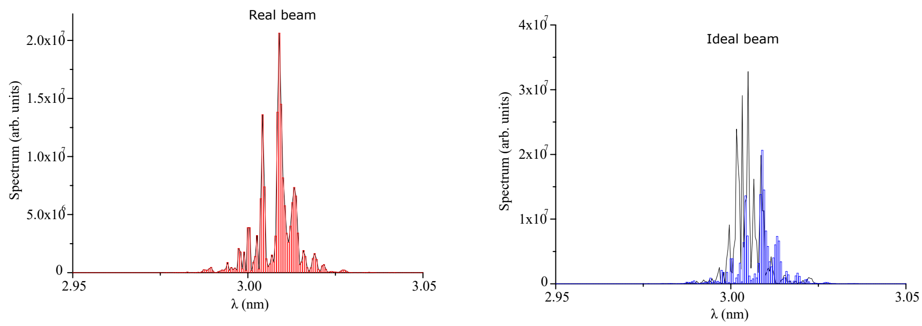

Figure 4.27: Spectrum at the end of UliX1 for emission at $\lambda = 3$nm, with the real electron beam (left panel) and with the ideal one (right panel)

For completeness, the emission at $\lambda = 1.8$nm with $a_w = 2$ gives a number of photons per shot of about 7x10^{11} (7x10^{17} photons per second).

4.2.2 High energy photon line: SASE

In order to test the SASE performances of UliX2 with the real MariX electron beam (see Figure 4.26), we analyzed the emission at the two wavelengths $\lambda = 2.4\mathring{A}$ and $5\mathring{A}$.

These two cases are summarized in Table 4.11 (see next page): the emission in the Angstrom range is also comparable in the two cases, thus demonstrating the efficiency of this beam for FEL operation within the entire wavelength domain of operation of MariX.

Table 4.11: Comparison between simulations for UliX2 ($\lambda_w = 1.2$cm) with the real and ideal beam. The electron beam parameters are the one of Table 4.9 and radiation properties are reported at the nominal undulator length $L_{und} = 60$m

	Real beam		**Ideal beam**	
λ ($\mathring{A}$)	2.4	5	2.4	5
a_w	0.75	1.5	0.75	1.5
ρ (10^{-3})	0.42	0.64	0.42	0.64
L_c (m)	4.59	2.99	4.59	2.99
$L_g - L_{g,3d}$ (m)	1.32-2.11	0.86-1.16	1.32-2.21	0.86-1.1
N_{ph}/shot (x 10^{11})	0.36	1.79	0.3	2.99
N_{ph}/s (x 10^{17})	0.36	1.79	0.3	2.99
Divergence (μrad)	2.6	4.5	2.5	3
Size (μm)	40	60	40	60
bw (%)	0.13	0.1	0.12	0.2

The comparison between the output spectra for emission at $\lambda = 2.4\mathring{A}$ at the end of UliX2 is shown in Figure 4.28.

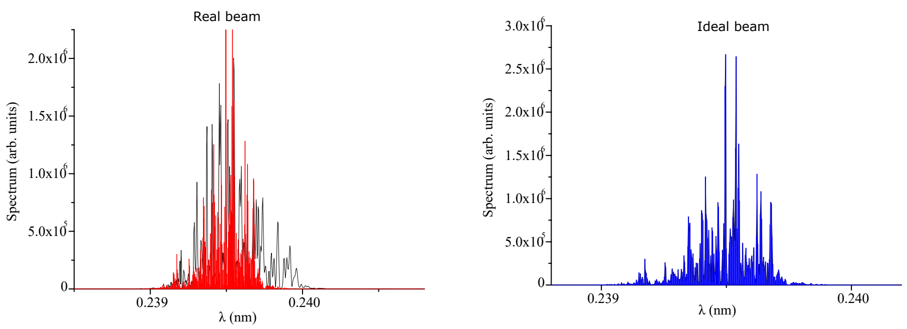

Figure 4.28: Spectrum at the end of UliX2 for emission at $\lambda = 2.4\mathring{A}$, with the real electron beam (left panel) and with the ideal one (right panel)

4.2.3 HGHG cascade with the real beam

The MariX beam has also been tested in the HGHG fresh-bunch 5x3 cascade down to $9\mathring{A}$ radiation. For this purpose and due to the present lack of simulated MariX beams at different energies, the beam energy of 3.2GeV has been reduced by one half to 1.6GeV as requested for this case (Table 4.6, example a).

The cascade layout is the one of Figure 4.17 and the seed source in Figure 4.18, the same used in the ideal cascade and already tested again shot noise at the same resonant frequencies, was considered.
The power growth for the used harmonics in the modulators and the final frequency in the radiator are shown in Figure 4.29:

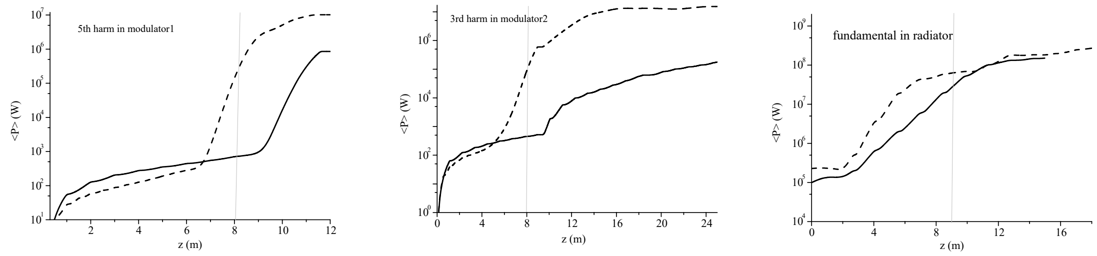

Figure 4.29: Comparison between the real beam (dashed line) and the ideal one (solid line) regarding the radiation growth on the used 5th harmonic from the first modulator (left panel), on the 3rd harmonic from the second modulator (in the middle) and on the fundamental from the radiator (right panel). The thick gray line indicates the approximate distance at which the radiation is extracted from the three modules Final wavelength is 0.9nm

The extracted pulse temporal profile from the radiator at $z \sim 8.5$m, together with its spectral profile compared to the one with the ideal beam are shown in Figures 4.30 and 4.31 (see next page).

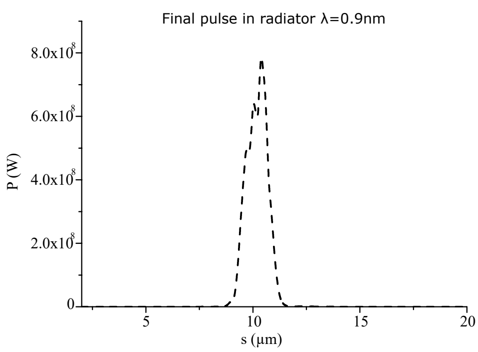

Figure 4.30: Temporal profile of the output pulse from the 5x3 cascade (final wavelength 0.9nm) with the real beam (see Table 4.9)

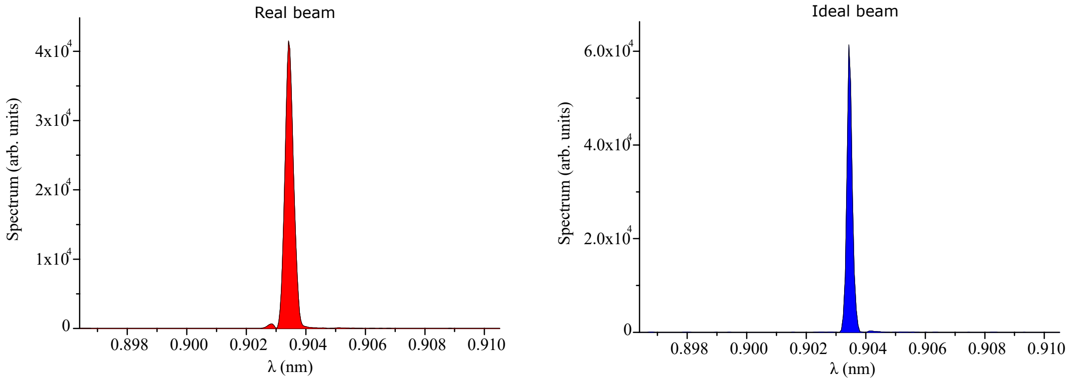

Figure 4.31: Spectral profile of the output pulse from the 5x3 cascade with the real beam (in red) compared to the one of the pulse obtained using the ideal beam (in blue)

The pulse is stable and coherent for about 10 meters, after which the SASE contribution breaks its stability and coherence as well.
The performances and radiation properties of the two cascades, with the real and the ideal electron beam, are listed in Table 4.12:

Table 4.12: Radiation properties of the output pulse extracted after about 10 meters of radiator in the 5x3 cascade ($\lambda = 0.9\mathring{A}$) with the real and ideal electron beam

	Real beam	**Ideal beam**
L_c (m)	2.8	2.85
ρ (10^{-3})	0.66	0.65
$L_g - L_{g,3d}$ (m)	0.82-1.04	0.8-1
N_{ph}/shot (x 10^{11})	1.28	0.36
Divergence (μrad)	32	30
Size (μm)	10	40
bw (%)	0.25	0.12
N_{ph}/s	1.28x10^{17}	3.6x10^{16}
τ_c (fs)	8.3	13.6

The listed results underline the possibility of using the real beam for the seeded configuration discussed. All the presented results do not take into account degradations due to errors, misalignments, jitters. However, the estimations exceed by one or more orders of magnitude the target values set by the scientific case.
MariX will be therefore capable to satisfy the requested FEL photon beam parameters expected by the envisaged experiments, considering also a safety margin dealing with the losses (tipically estimated to one order of magnitude) in delivering the photon beams to the experimental hall.

4.3 Discussion on other seeding options for MariX

The stringent condition of minimizing the space and the costs induced us to consider as primary option the use of a conventional, not segmented undulator and the operation in the SASE mode, with the possibility of exploiting the single spike regime combined potentially with the undulator tapering (as an upgrade option of the configuration considered here). Regarding the seeding option, techniques requiring a linear space larger than the allocated one and providing only partial coherence, such as EEHG (see section 2.5) and self-seeding (see section 2.6), have not been discussed but could be considered for future upgrades. As shown in this chapter, among all the proposed schemes (see Chapter 2 for a detailed description), the more interesting for MariX are the operations with segmented undulator, either with the implementation of an afterburn module for harmonic up-conversion or with the sequence of modules in cascade, by exploiting the non linear harmonic generation and the direct seeding done with the harmonics in gas.
At such short wavelengths as the ones reached by MariX, and starting the cascade from about 13nm, the main issue for the FEL emission is the SASE/seed competition, which makes the generation of a coherent, stable and shape-cleaned pulse more difficult than at lower wavelengths (see Figure 4.23). For these reasons, the work focused mainly on the definition of an optimal seed for the FEL.

However, future outlooks may also include an upgrade to the fresh-bunch technique for the HGHG cascades, able to exploit also the electron bunching at higher harmonics: the bunching could be enhanced by means of a dispersive chicane[8] between the second modulator and the radiator, and could lead to reduced saturation lengths (by one order of magnitude) and increased saturation powers with respect to SASE operation. This kind of technique would require an extra space for the cascade, but would approximately result in the same total length with respect to the considered option, and it is thus a viable alternative. Its effect on the beam coherence and stability needs to be investigated.

To improve the HHG spectrum and the pulse stability, another option which has been studied is that of seeding the HGHG cascade with an FEL oscillator [10] at 13.6nm (see section 4.3.1). It would be also interesting to study the feasibility and the performances of an X-ray regenerative amplifier, as highlighted in section 4.3.2.

4.3.1 Harmonic cascade seeded by a FEL Oscillator

The rather distorted spectrum arising from HHG at 13nm can be improved using another seeding configuration for the fresh-bunch harmonic cascade. A possibility which has been analyzed is that of seeding the cascade with a FEL oscillator at 13.6nm.

[8]Dispersive chicanes are made of 5 drift spaces separated by 5 bending magnets for beam deflection

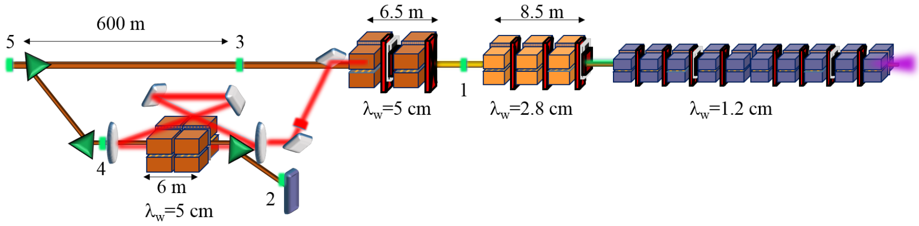

Figure 4.32: Segmented undulator scheme for a three-stage cascade driven by a FEL Oscillator in the EUV

In this second option, shown in Figure 4.32, the seed is delivered by an oscillator (FELO) working at 13.6nm. Since the electron beam alimenting the oscillator is deteriorated by the radiation, it is dumped after the passage into the module of undulator of the oscillator. Therefore, the electron beams of the 1 MHz train (separated by 300m) are alternatively driven into the oscillator and into the FEL cascade, giving a resulting 0.5MHz repetition rate.
A 12m long undulator resulted in sovra-saturation and low temporal stability of the pulse, composed by two horns. The oscillator is therefore constituted by a 6m long undulator with period λ_w = 5cm and a_w = 2.08, the same values of the first modulator in the following cascade. Assuming to use the 1.6 GeV electron beam, it emits at 13.6nm, corresponding to the optimum wavelength for Mo/Si multi-layer mirrors [101], having reflectivities up to R=0.75% at normal incidence.

Since the seed radiation should superimpose to the subsequent electron beam at the entrance of the first modulator, it has to be retarded by $1\mu s$, corresponding to a total length of about 300m. If a four mirrors 150m long cavity is hypotized, the decrease of the seed field is about 50%. The seed should then be transported in a delay line, made of a couple of mirrors at least, corresponding to further reflections and losses.

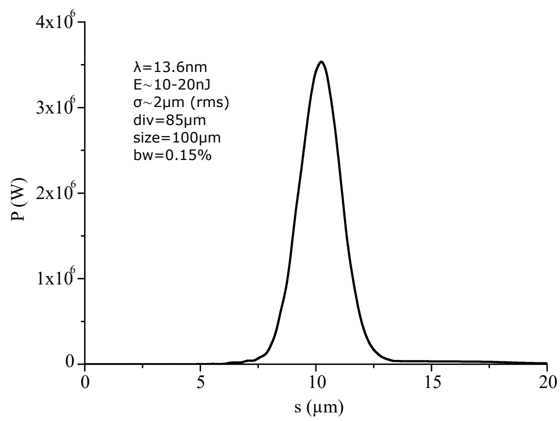

Figure 4.33: Radiation pulse extracted after 12 roundtrips within the FEL oscillator, to be used as seed

After about 12 passages within the undulator (about 12μsec), corresponding to 12 roundtrips in the oscillator cavity, the radiaton pulse has been enough amplified and purified to seed the cascade. The pulse extracted from the oscillator, which is subjected to other two reflections in the transfer line, is shown in Figure 4.33 together with its characteristics. Its energy is three orders of magnitude larger than the shot noise level of $E_{sn} \sim 0.002$nJ, similarly to the HHG seeding source considered in the previous sections.
Due to the use of additional mirrors in the transfer to the cascade, the seed reported in Figure 4.33 has already lost about one order of magnitude of peak power.

The 13.6nm signal of the oscillator is now used to seed the 5x3 cascade: the result are presented in Figure 4.34, which compares the output temporal and spectral profiles obtained with the 5x3 cascade seeded by HHG and the oscillator:

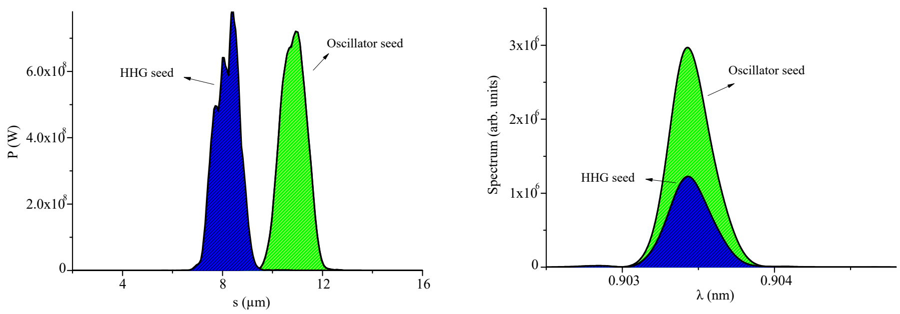

Figure 4.34: Temporal (left panel) and spectral (right panel) profile of the output pulse extracted from the radiator when the cascade is seeded by HHG (blue) or by the oscillator at 13.6nm (green). The temporal profile from the cascade seeded by HHG has been shifted longitudinally to be compared with the other profile. The spectral intensities are given in arbitrary units in both cases, and this difference here makes the comparison easier

The radiation pulse in this case showed more stability, retaining its Gaussian profile (see the green area in left panel) for more than 12m within the radiator (instead the pulse from the HHG cascade is stable for about 8 meters), and the one showed in Figure 4.34 was extracted at $z \sim 12$m.
It is possible to note that the pulse is less subjected to SASE contributions than in the cascade seeded by HHG. The effects of the oscillator on the radiation properties include higher pulse temporal stability and coherence, shorter saturation length and also a slightly higher number of photons produced.

Table 4.13 (see next page) compares the final radiation pulse characteristics.
The seeded FEL performances are improved in this configuration, but other upgrades and options will not be excluded. For this reason, it may give better results also at shorter wavelengths such as the 4.8$\mathring{A}$ cascade. This will be object of further investigation.

Table 4.13: Radiation properties of the output pulse extracted after about 10 meters of radiator in the 5x3 cascade ($\lambda = 0.9\AA$)

	HHG cascade	**Oscillator cascade**
L_c (m)	2.8	2.47
ρ (10^{-3})	0.71	0.77
$L_g - L_{g,3d}$ (m)	0.82-1.01	0.7-1.1
N_{ph}/shot (x 10^{11})	1.28	1.58
Divergence (μrad)	32	6.2
Size (μm)	10	5
bw (%)	0.25	0.1
Rep. Rate (MHz)	1	0.5
N_{ph}/s	1.28x10^{17}	0.8x10^{17}
τ_c (fs)	8.3	14

4.3.2 X-ray regenerative amplifier

A third option to be considered for MariX seeded FEL is a regenerative amplifier [105, 106], where the sequence of the electron bunches entering the undulator is synchronized with the path of the radiation that is reflected and recirculated by hard X-rays mirrors as shown in Figure 4.35.

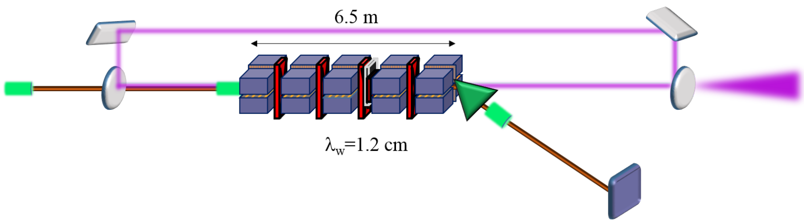

Figure 4.35: Regenerative Amplifier at MariX

Crystal diffractive mirrors [9, 102, 103, 107], such as graphite (tunable from 1.85keV with continuity), Si (from 2keV) and diamond (from 3keV), may be used in principle: however, their effect of monochromatization and their reflectivity spectra need to be carefully analyzed to prove the feasiblity of such a scheme in the hard-X range. In particular, their reflectivity and transmission profiles need to be simulated with respect to the photon energy and angle of incidence. Preliminary simulations with plane, perfect crystals have shown the graphite-based mirrors to be the best candidate, having high reflectivity and low absorption, but the technological availability of such mirrors has not been checked yet.
This kind of configuration has been only proposed and still has to be studied, so that other problems may arise in the future.

Chapter 5

Conclusions

The study and design of a new X-ray FEL source, as part of the newly conceived ambitious MariX project aimed at delivering ultra-bright and ultra-fast pulses with high repetition rates (1-100MHz), suitable for various experimental research applications such as linear spectroscopy and imaging, has been carried out.
In particular the performances of both low (100eV to 4KeV) and high (2keV to 8keV) energy lines have been simulated and the optimal electron beam characteristics within the nominal range allowed by the upstream accelerator complex have been defined, analizing the two working points corresponding to long high charge and short low charge X-ray signals.

The electron beam optimized for FEL operation in the soft-to-hard X-range should have relative energy spread of $2-3\text{x}10^{-4}$, normalized emittances of about 0.5mm mrad and 1.6-1.8kA peak currents. Through such optimal electron beam, the capability of generating $10^{10}-10^{11}$ photons per pulse ($10^{16}-10^{17}$ photons per second) in the low energy soft-X range (0.8-3nm in wavelength) with low charge (Q=8pC) electrons has been demonstrated, resulting in single spiked X-pulses, while the use of high charge (Q=50pC) electron beams allows to increase the number of photons up to one order of magnitude but results in multiple spiked pulses. As regards the high energy line (0.1-0.9nm in wavelength), the more performant high charge electron beams enable the production of $10^{9}-10^{10}$ photons per pulse ($10^{15}-10^{16}$ photons per second) tailored for linear spectroscopy experiments (for emission at $2.5-5\mathring{A}$) and single shot imaging (down to $1.5\mathring{A}$). Therefore, the expected performances do not exceed the linear response regime and space charge effects, as requested by MariX scientific case.

To improve the limited coherence and low shot-to-shot stability of the produced FEL pulses, different seeding schemes have been proposed and studied in literature, and an High Gain Harmonic Generation (HGHG) multi-stage cascade using the fresh-bunch injection technique was initially considered for the MariX FEL, thanks to the limited space requirements and the possibility to reach the desired beam characteristics and frequencies by up-shift frequency conversion.

As regards the seeded operation in the wavelength domain covered by the source, the main difficulty comes from the seed signal, which should have a much shorter wavelength with respect to the VUV laser sources available. The High Harmonic Generation (HHG) in gas is an advanced technique which allows to reach shorter wavelengths using laser harmonics produced by the interaction with a gas target, and a couple of studies support its efficacy in obtaining wavelengths of 13.6nm down to 12nm corresponding to very high-order harmonics of a Ti:Sa laser.
In the HGHG cascade seeded by HHG, the electron energy modulation by means of an external seed (in this case the coherent harmonics of a pump laser produced in gas) is converted into a density modulation which enhances the harmonic content of the electron bunch at the desired wavelength.
A 5x3 cascade starting from a 13.6nm, 12nJ seed signal and reaching a final wavelength of $9\AA$ resulted in 10^{10} photons per shot with a coherence time of about 13fs, at least one order of magnitude higher than the one of the SASE pulse. A second 5x5 cascade reaching a shorter wavelength of $4.8\AA$ has been analyzed, resulting in the same number of photons but with a reduced pulse stability. In the wavelength range between 2 and $5\AA$ (5-2keV), the simulations forecast, at the exit of the undulator, either $10^{10} - 10^{11}$ photons per shot with a repetition rate of 1MHz in SASE mode or $10^{9} - 10^{10}$ photons per shot in single spike SASE mode and in cascaded seeded configuration.
The results obtained with the proposed seeded operation of the FEL demonstrate the production of coherent X-ray pulses at high repetition rate, but the method needs to be experimentally tested and optimized.

A second seeding option to the same cascade, namely an FEL oscillator at 13.6nm with no need to extend the longitudinal space of the machine and having a more cleaned spectrum than HHG, demonstrated improved central wavelength stability, reduced spectral linewidth and a larger longitudinal coherence length with the same number of photons produced.
The results obtained throughout this work do not pretend to be exhaustive and conclusive, but they confirm the expected outstanding performances of the MariX FEL and the possibility of generating a truly coherent photon beam at 100kHz with state of the art technologies, thus approaching, at X-ray energies, the unique performance of the only-existing seeded FEL FERMI@Elettra. Furthermore, even if the presented results do not take into account degradations due to errors, misalignments, jitters and were obtained with tight optimizations along the whole beam, the estimations exceed by one or more orders of magnitude the target value of 10^{8} set by the MariX scientific case, which will be therefore capable to satisfy the requested FEL photon beam parameters expected by the envisaged experiments, considering also a safety margin dealing with the losses in delivering the photon beams to the user's stations in the experimental butch.

Future outlooks include the study of other possible techniques and implementations of the seeded configuration to further improve the results here obtained and the feasibility study of a possible X-ray regenerative amplifier for MariX, which is now in progress. Since linear spectroscopy experiments are the main target application of MariX radiation, and since a relatively small number of coherent photons per pulse (order 10^{10}) is requested, higher coherence of the FEL pulses is preferred to the higher pulse intensity.

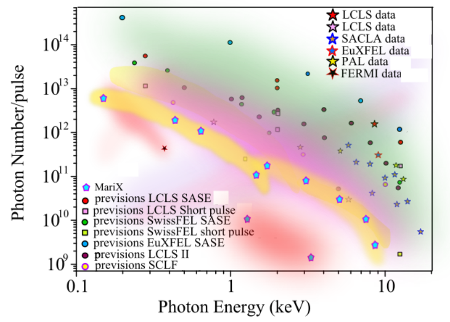

Figure 5.1: Number of photons per pulse vs photon energy (keV) for FELs operating in X-ray: experimental (stars) and predicted (circles and squares) data. The green shadow marks the long pulse SASE operation area, the magenta shadow delimits the short pulse or self-seeded regime, the red one is relevant to the operation in the seeded mode and the yellow shadow marks the MariX performances, re-elaborated from [89]

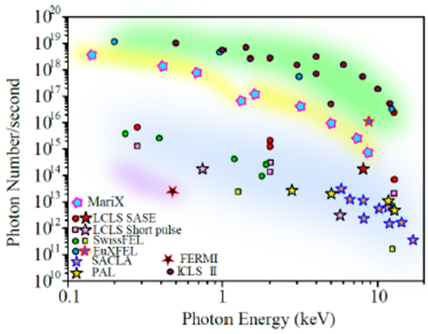

Figure 5.2: Number of photons per second versus photon energy (keV). The green shadow delimits the high flux operation with Super-conducting Linacs, the blue one is relevant to room temperature Linacs (10-120 Hz). Violet area is relevant to FERMI, while the yellow area to MariX, from [89]

Figures 5.1 and 5.2 show the MariX previsions compared to other existing FEL sources or projects worldwide in terms of photons per pulse and per second respectively. The nominal number of photons per shot produced by the designed FEL source is only marginally competitive with respect to other existing facilities, because it remains almost one order of magnitude below. However, the novelty introduced by MariX is given by the number of photons per second, which places the source in an uncovered domain among other more costly and biggest super-conducting infrastructures. The 4-5 orders of magnitude gain in repetition rate allowed by MariX restores the high flux per second of the most advanced synchrotron sources, whilst having ultrashort pulses suitable for time resolved pump-probe methods in optical, photoelectric effect and inelastic X scattering experiments.

Figure 5.3 shows its expected peak and average brilliance compared to other facilities. Such source will fill in the X-ray absorption spectroscopy and X-ray Magnetic

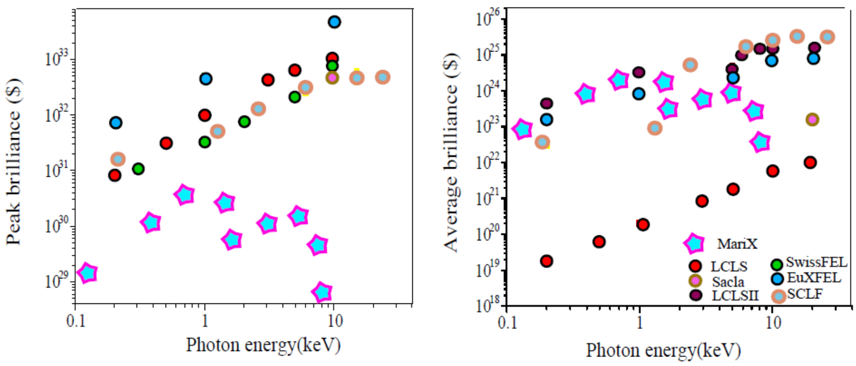

Figure 5.3: MariX peak and average brilliance compared to other sources, from [89]

Circular dichroism, as well as bulk photoemission, to become highly efficient probes of matter at the nanoscale but in bulk environments, like buried interfaces of interest in materials science, in-vivo biological samples or catalysers at work. The source will therefore create absolutely novel conditions for experiments that cannot be performed satisfactorily at the present and foreseen sources based on storage rings or SASE-FELs. The anticipated performances of MariX Free Electron Laser are well beyond the state of the art of presently FELs in operation, and in the trailing edge of EuXFEL and of the US future superconducting FEL project of reference (LCLS-II) as illustrated in Figure 5.1. The work may constitute also an outcome and valuable result for all the existing or foreseen facilities with seeded FEL amplifiers.

Bibliography

[1] L. Serafini et al., “MariX, an advanced MHz-class repetition rate X-ray source for linear regime time-resolved spectroscopy and photon scattering,” *Submitted to NIM-A*, (2019).

[2] P. Emma, R. Akre, et al., “First lasing and operation of an Angstrom-wavelength free-electron laser,” *Nature Photonics*, vol. 4, (2010).

[3] D. Pile, “First light from SACLA,” *Nature Photonics*, vol. 5, (2011).

[4] E. Allaria, R. Appio et al., “Highly coherent and stable pulses from the FERMI seeded free-electron laser in the extreme ultraviolet,” *Nature Photonics*, vol. 6, (2012).

[5] F. Ciocci, G. Dattoli et al., “Proposition of Experiment at SPARC: harmonic generation seeded by high order harmonics produced in gas,” *SPARC-FEL-04/005*, (2004).

[6] G. Stupakov, “Echo-Enabled Harmonic Generation,” (2010).

[7] G. Geloni, “Cascade self-seeding scheme with wake monochromator for narrow-bandwidth X-ray FELs,” *Physics acc-ph*, (2010).

[8] G. Dattoli, E. Di Palma, A. Petralia, “Free electron laser oscillator efficiency,” *Optics Communications*, vol. 425, (2018).

[9] R. Lindberg et al., “Performance of the x-ray free-electron laser oscillator with crystal cavity,” *Phys Rev. Accelerators and beams*, vol. 14, 010701, (2011).

[10] K .Li et al., “High brightness fully coherent x-ray amplifier seeded by a free-electron laser oscillator,” *Phys. Rev. Accel. and Beams*, vol. 21, 040702, (2018).

[11] A.Kai Li, Jiawei Yan, Chao Feng, Meng Zhang, and Haixiao Deng, “High brightness fully coherent X-ray amplifier seeded by a free-electron laser oscillator.”

[12] M. Artioli et al., “EuPRAXIA at SPARC Lab CDR,” (2017).

[13] M. Couprie and L. Giannessi, “Seeding Free Electron Lasers with High Order Harmonics Generated in Gas,” *Springer Series in Optical Sciences*, (2015).

[14] L. Giannessi et al., "Self-amplified spontaneous emission free-electron laser with an energy-chirped electron beam and undulator tapering," *Physical review letters*, vol. 106.14, (2011).

[15] Sven Reiche, "Overview of Seeding Methods for FELs," *Proceedings of IPAC, Shangai, China*, (2013).

[16] Sven Ackermann, "Experimental and numerical investigations on seeding options for the multi-beam line Free-Electron Laser facility FLASH," *Dissertation, Hamburg*, (2016).

[17] H. Freund et al., "Nonlinear harmonic generation and proposed experimental verification in SASE FELs," *Nucl. Instrum. Methods Phys. Res. Sect A*, vol. 445, (2000).

[18] W. Ackermann et al., "Operation of a free-electron laser from the extreme ultraviolet to the water window," *Nature Photon*, vol. 1, 336, (2007).

[19] D. Ratner et al., "Second and third harmonic measurements at the linac coherent light source," *Phys. Rev. ST Accel. Beams*, vol. 14, (2011).

[20] E.L.Saldin et al. *Opt. Commun.*, vol. 212, (2002).

[21] E. L. Saldin et al., "Self-amplified spontaneous emission FEL with energy-chirped electron beam and its application for generation of attosecond x-ray pulses," *Phys. Rev. ST Accel. Beams*, vol. 9, (2006).

[22] R. Hajima et al., "Third-harmonic lasing at JAERI-FEL," *Nucl. Instrum. Methods Phys. Res., Sect A*, vol. 475, (2001).

[23] R. Warren et al., "Lasing on the third harmonic," *Nucl. Instrum. Methods Phys. Res., Sect A*, vol. 296, (1990).

[24] S. Benson and J. Madey, "Demonstration of harmonic lasing in a free-electron laser," vol. 39, (1989).

[25] Thompson, McNeil, "Mode locking in a Free Electron Laser amplifier," *Phys. Rev. Lett.*, vol. 100, 203901, (2008).

[26] Kur, Dunning, McNeil, Wurtele and Zholents, "A wide bandwidth free-electron laser with mode locking using current modulation," *NJP*, vol. 13, 063012, (2011).

[27] L. Giannessi, "Seeding and Harmonic Generation in Free-Electron Lasers," *Springer*, (2016).

[28] G. Stupakov, "Using the Beam-Echo effect for generation of short-wavelength radiation," *Physical Review Letters*, vol. 102, (2009).

[29] T. Tanaka and R. Kinjo, "High gain harmonic generation free electron lasers enhanced by pseudoenergy bands," *Physical Review Accelerators and Beams*, vol. 20, (2017).

[30] E. J. Takahashi et al., "Dramatic enhancement of High-order harmonic generation," *Physical Review Letters*, vol. 99, (2007).

[31] M. E. Couprie, G. Lambert et al., "Seeding FEL with high harmonics in gas," *Conference: Nanobeam 35th ICFA*, (2005).

[32] M. Labat et al., "Pulse Splitting in short wavelength seeded Free Electron Lasers," *Phys. Rev. Lett.*, vol. 103(26), 26480, (2009).

[33] L. Giannessi et al., "High-Order Harmonic Generation and Superradiance in a seeded free-electron laser," *Phys. Rev. Lett.*, vol. 108, (2012).

[34] G. Dattoli, L. Giannessi, P. L. Ottaviani and A. Torre, "Dynamical behavior of a free-electron laser operating with a prebunched electron beam," *Physical Review Letters E*, vol. 49, (1994).

[35] Dinh C. Nguyen and Quinn R. Marksteiner, "One dimensional FEL theory," *US Particle Accelerator School*, (2014).

[36] G. Stupakov, "Echo-enabled harmonic generation for seeded FELs," *Proc. SPIE 8078, Advances in X-ray Free-Electron Lasers: Radiation Schemes, X-ray Optics, and Instrumentation*, (2011).

[37] L. Giannessi et al., "FEL experiments at SPARC: Seeding with harmonics generated in gas," *Proceedings of FEL, Malm, Sweden*, (2010).

[38] G. Lambert et al., "Seeding high gain harmonic generation with laser harmonics produced in gases," *Proceedings of the FEL Conference*, (2004).

[39] P. Corkum, "Plasma perspective on strong field multiphoton ionization," *Phys. Rev. Lett.*, vol. 71, (1994).

[40] M. Lewenstein et al., "Theory of high-harmonic generation by low-frequency laser fields," *Phys. Rev. A*, vol. 49, (1994).

[41] K. Kulander et al., "Dynamics of short-pulse exitation, ionization and harmonic-conversion," *Springer*, (1993).

[42] P.Balcou et al., "Generalized phase-matching conditions for high harmonics: The role of field-gradient forces, journal=,"

[43] L. H. Yu et al., "High-Gain Harmonic Generation Free Electron Laser," *Science*, (2000).

[44] Couprie et al., "A French proposal for an innovative accelerators based coherent UV X-ray source," *Nucl. Instr. Meth. Phys. Res. A*, vol. 528, (2004).

[45] D. Garzella et al., “Using VUV high-order harmonics generated in gas as a seed for single pass FEL, journal=,”

[46] A. Doyuran et al., “Characterization of a high-gain harmonic-generation free-electron laser at saturation,” *Phys. Rev. Lett.*, vol. 86, (2001).

[47] G. Lambert et al., “Injection of harmonics generated in gas in a free-electron laser providing intense and coherent extreme-ultraviolet light,” *Nat. Phys.*, vol. 4, 296, (2008).

[48] M. Labat et al., “High-Gain harmonic generation free-electron laser seeded by harmonics generated in gas,” *Physical Review Letters*, vol. 107, (2011).

[49] E. Allaria, “Impact of radiator length in the emitted power for a high-gain harmonic generation free-electron laser,” *Physical Review*, vol. 16, (2013).

[50] L. Giannessi, “Superradiant cascade in a seeded free-electron laser,” *Physical Review Letters*, vol. 110, (2013).

[51] L. Giannessi, M. Artioli et al., “High-order harmonic generation and Superradiance in a seeded free-electron laser,” *Physical Review Letters*, vol. 108, (2012).

[52] L. Giannessi et al., “Seeding at SPARC,” *Proceed. FEL Conf. Stanford*, (2005).

[53] T. Togashi et al., “Extreme ultraviolet free electron laser seeded with high order 8232harmonic of Ti: sapphire laser,” *Opt. Express*, vol. 19, (2011).

[54] S. Ackermann et al., “Generation of Coherent 19- and 38-nm Radiation at a Free-Electron Laser Directly Seeded at 38 nm,” *Phys. Rev. Lett.*, vol. 111, (2013).

[55] D. Alesini et al., “Status of the SPARX FEL project,” *Proceedings FEL Conf. Stanford*, (2005).

[56] M. Zepf et al., “Bright Quasi-phase Matched Soft-X-Ray Harmonic Radiation from Argon Ions,” *Phys. Rev. Lett.*, vol. 99, (2007).

[57] A. Paul et al., “Quasi-phase matched generation of coherent extreme-ultraviolet light,” *Nature*, vol. 421, (2003).

[58] I. Kim et al., “Generation of submicrojoule high harmonics using a long gas jet in a two-color laser field,” *Appl. Phys. Lett.*, vol. 92, 021125, (2008).

[59] X. Zhang et al., “Quasi-phase matching and quantum-path control of high-harmonic generation using counterpropagating light,” *Nature Physics*, vol. 3, (2007).

[60] B. Carré *Talk presented at the slicing ARC-EN-CIEL Workshop Orsay*, 3-4 February 2004.

[61] Z.Chang et al., "Generation of coherent soft-X rays at 2.7nm using high harmonics," *Phys. Rev. Lett.*, vol. 79, 16, (1997).

[62] E.J.Takahashi et al. *IEEE Journal Of Selected Topics In Quantum Electronics*, vol. 10, No. 6.

[63] G Lambert et al., "An optimized kHz two-colour high harmonic source for seeding free-electron lasers and plasma-based soft x-ray lasers," *New Journal of Physics*, vol. 11, 083033, (2009).

[64] G. Lambert et al., "High harmonics from gas, a suitable source for seeding FEL from the vacuum-ultraviolet to soft X-ray region," *Proceedings of FEL, Shangai, China*, (2011).

[65] L. H. Yu et al., "First ultraviolet high-gain harmonic generation free electron laser," *Physical Review Letters*, vol. 91, (2003).

[66] M. Labat et al., "Seeding experiments at SPARC," *Proceedings of FEL, Liverpool UK*, (2009).

[67] L. Giannessi et al., "First lasing of FERMI FEL-2 (1 stage) and FERMI FEL-1 recent results," *Proceedings of the 2012 FEL Conference, Nara*, (2012).

[68] Ben-Zvi, K. M. Yang and L. H. Yu, "The fresh-bunch technique in FELs," *International free electron conference, Santa Fe, New Mexico*, (1991).

[69] I. Ben-Zvi et al., "The fresh-bunch technique in FELS," *Nucl. Instrum. Methods Phys. Res. A*, vol. 318, (1992).

[70] L. HuaYu, I. Ben-Zvi, "High-gain harmonic generation of soft x-rays with the fresh-bunch technique," *Nucl. Instrum. Methods Phys. Res. A*, (1997).

[71] E. Allaria et al., "Double stage seeded FEL with fresh bunch injection technique at FERMI," *Nature Photonics*, (2013).

[72] Quinn Marksteiner, "FEL class notes on Seeding techniques," *US Particle Accelerator School*, (2015).

[73] C. Evain, M.-E. Couprie et al., "Study of high harmonic generation at synchrotron soleil using echo-enabling technique," *Procceedings of IPAC Kyoto, Japan*, (2010).

[74] Z.T. Zhao et al., "First lasing of an echo-enabled harmonic generation free-electron laser," *Nat. Photonics*, vol. 6, (2012).

[75] D. Xiang, G. Stupakov et al., "First demonstration of the Echo-enabled harmonic generation technique for short wavelength seeded free electron lasers," *Phys. Rev. Lett.*, vol. 105, (2010).

[76] D. Xiang, Z. Huang et al., "Feasibility study for a seeded hard x-ray source based on a two-stage echo-enabled harmonic generation FEL," *Proceedings of FEL, Liverpool, UK*, (2009).

[77] M. Dunning et al., "A proof-of-principle echo-enabled harmonic generation experiment at SLAC."

[78] J. Felhaus, E. Saldin et al., "Possible application of X-ray optical elements for reducing the spectral bandwidth of an X-ray SASE FEL," *Optics Communications*, vol. 140, (1997).

[79] V. Miltchev, J. Rossbach et al., "Simulation studies on the self-seeding option at FLASH," (2006).

[80] E. Saldin et al., "X-ray FEL with a meV bandwidth," *Nucl. Inst. and Meth. in Phys. Research Section A*, vol. 475, (2001).

[81] F.-J. Decker, "LCLS operation in self-seeding mode," *Desy*, (2013).

[82] J. Amann et al., "Demonstration of self-seeding in a hard X-ray free-electron laser," *Nature Photon*, vol. 6, (2012).

[83] Y. Feng et al., "X-ray Optics for soft X-ray Self-Seeding the LCLS-II," *Proceedings of the FEL Conference, Malmo*, (2010).

[84] J. Wu, A. Marinelli and C. Pellegrini, "Generation of longitudinally coherent ultra high power X-ray FEL pulses by phase and amplitude mixing," *Proceedings of the FEL Conference, Japan*, (2012).

[85] D. C. Nguyen et al., "Regenerative Amplifier FEL," *Proceeding of the Linac Conference, Monterey*, (2000).

[86] M. L. Grnbein, J. Bielecki et al., "Megahertz data collection from protein microcrystals at an X-ray free-electron laser," *Nature Communications*, vol. 9, (2018).

[87] T. Raubenheimer, "LCLS-II-HE FEL Facility Overview," (2016).

[88] "https://www.elettra.trieste.it/lightsources/elettra."

[89] L. Serafini, G. Rossi et al., "MariX Conceptual Design Report," *http://www.fisica.unimi.it/ecm/home/ricerca/marix*, (2019).

[90] W.J. Brown et al., "Experimental characterization of an ultrafast Thomson scattering x-ray source with three-dimensional time and frequency-domain analysis," *Physical Review Special Topics-Accelerators and Beams*, vol. 7.6, (2004).

[91] A. Jochmann et al., "High resolution energy-angle correlation measurement of hard x rays from laser-Thomson backscattering," *Physical review letters*, vol. 111.11, (2013).

[92] S. Di Mitri, "Feasibility study of a periodic arc compressor in the presence of coherent synchrotron radiation," *Nuclear Instruments and Methods in Physics Research Section A: Accelerators, Spectrometers, Detectors and Associated Equipment*, vol. 806, (2016).

[93] S. D. Mitri and M. Cornacchia, "Transverse emittance-preserving arc compressor for high-brightness electron beam-based light sources and colliders," *EPL*, vol. 109(6):62002, (2015).

[94] G. Bellomo, "Dispensa del corso di Fisica degli Acceleratori 1, cap.5." (2018).

[95] F. Ciocci et al., "Segmented undulator operation at the SPARC-FEL test facility," *International Society for Optics and Photonics, Advances in X-ray Free-Electron Lasers Instrumentation III*, vol. 9512, (2015).

[96] "PSI-SwissFEL Conceptual Design Report."

[97] A.B. Temnykh, "Delta undulator for Cornell energy recovery linac," *Phys. Rev. ST Accel. Beams*, vol. 11, (2008).

[98] L. Giannessi et al., "Self-amplified spontaneous emission for a single pass free-electron lase," *Physical Review Special Topics-Accelerators and Beams*, vol. 14.6, (2011).

[99] E.L. Saldin, E.A. Schneidmiller and M.V. Yurkov, "Self-amplified spontaneous emission FEL with energy-chirped electron beam and its application for generation of attosecond x-ray pulses," *Physical Review Special Topics-Accelerators and Beams*, vol. 9.5, (2006).

[100] B.W.J. McNeil, N.R. Thompson, and D.J. Dunning, "Transform-limited X-ray pulse generation from a high-brightness self-amplified spontaneous-emission free-electron laser," *Physical review letters*, vol. 110.13, (2013).

[101] M. Singh, J.Braat, "Design of multilayer extreme-ultraviolet mirrors for enhanced reflectivity," vol. 39, (2000).

[102] Y. Shvydko et al., "High-reflectivity high-resolution x-ray crystal optics with diamonds," *Nature Physics*, vol. 6, (2010).

[103] Y. Shvydko, R. Lindberg, "Spatiotemporal response of crystals in x-ray bragg diffraction," *Physics Optics*, (2012).

[104] E. Allaria et al., "Two stage seeded soft X-Ray Free Electron Laser," *Nature Photonics*, (2013).

[105] K. Kwang-Je, "An FEL oscillator: performance, challenges and implementations," *ARD seminar Desy, Hamburg, Germany.*

[106] K. Kwang-Je, "Beam dynamics problems for x-ray FEL oscillator (XFELO)," *Argonne National Laboratory, Arcidosso, Italy*, (2017).

[107] Y. Shvydko et al., "Diamond double-crystal system for a forward bragg diffraction x-ray monochromator of the self-seeded pal XFEL," *FEL 2017, Santa Fe, NM, USA.*

[108] Timur Shaftan, "Synchrotron Radiation," (1999).

[109] P. Schmuser, M. Dohlus and J. Dohlus, "Low Gain FEL Theory," (2008).

[110] Sven Reiche, "Numerical Studies for a Single Pass High Gain Free-Electron Laser," *Dissertation, Hamburg*, (1999).

[111] K. Balewski et al., "PETRA III: a low emittance synchrotron radiation source. Technical Design Report," *Tech. rep.*, (2004).

[112] J. M. Madey, "Stimulated emission of bremmstrahlung in a periodic magnetic field," *Journal of Applied Physics*, vol. 42(5), (1971).

[113] G. Dattoli, S.Pagnutti et al., "Introduction to the Physics of Free Electron Laser and Comparison with conventional laser sources," *Free Electron Lasers, Dr. Sandor Varro*, (2012).

[114] W. Colson, "The Nonlinear Wave Equation for Free Electron Lasers driven by Single-Particle Currents," *Physics Letters*, vol. 76A, (1980).

[115] G. Dattoli et al., "High gain oscillators: pulse propagation and saturation," *J. Appl. Phys*, vol. 101(10), (2007).

[116] G. Dattoli, A. Ranieri and A. Torre, "Lectures on the free electron laser theory and related topics," *World Scientific*, (1993).

[117] W. Colson, "The Nonlinear Wave Equation for Higher Harmonics in Free-Electron Lasers," *Journal of Quantum Electronics*, vol. 17, (1981).

[118] G. Dattoli et al., "Two Color Free electron laser and Frequency beating," *Physical Review Letters*, vol. 111, (2013).

[119] G. Dattoli, L. Giannessi and A. Torre, "Unified view of free-electron laser dynamics and of higher harmonics electron bunching," *J. Opt Soc. Am. B*, vol. 10, (1993).

[120] G. Dattoli, L. Giannessi, P. L. Ottaviani and A. Segreto, "Free electron laser dynamics, evolution of the bunching coefficients, and coherent harmonic generation," *Journal of Applied Physics*, vol. 78, (1995).

[121] V. Petrillo and Marcello R. Conti, “Scaling laws for X-ray Free-electron lasers.” (2010).

[122] Sven Reiche, *GENESIS 1.3, user manual.*

List of Tables

List of Figures

Appendix A

From Synchrotron Radiation to Free Electron Laser sources

A.1 Synchrotron radiation

Synchrotron radiation is produced when relativistic charged particles are forced to have bent trajectories by magnetic fields, and is emitted tangentially to their curvature. With the growing demand for higher electron beam energies and stored beam currents, the development of accelerators led to the invention of storage rings, which are the technological basis for all circular light sources nowadays.
Light sources can be divided according to some of their properties, such as wavelength, directivity, flux, brilliance (also called brightness in USA) and coherence. The directivity is the maximum directive power $D(\theta, \phi) \propto \frac{\text{power per solid angle}}{P_{\text{total}}}$ among all solid angles of radiation [108], the flux is represented by the number of photons emitted per second and the coherence refers to the pulses' spectral and temporal stability (analyzed later in section 3.6). As regards the brilliance, it is defined as photon flux divided by radiation volume according to

$$B = \frac{\text{Photon flux}}{\text{source area} * \text{source divergence} * \text{bandwidth}} = \frac{N_{ph}}{(2\pi)^2 \Sigma_x \Sigma'_x \Sigma_y \Sigma'_y} \tag{A.1}$$

where bandwidth (BW) $= \Delta\lambda/\lambda$. It depends on the total source size, which is a convolution of electron beam $(\sigma_{x,y}, \sigma'_{x,y})$ and radiation $(\sigma_R, \sigma\prime_R)$ sizes and divergences, thus $\Sigma_{x.y} = \sqrt{\sigma^2_{x,y} + \sigma^2_R}$ and $\Sigma\prime_{x.y} = \sqrt{\sigma\prime^2_{x,y} + \sigma\prime^2_R}$.

The history of synchrotron radiation sources is conventionally subdivided into four so-called generations [16, 108]. The 1^{st} generation light sources parasitically used synchrotron radiation emitted in bending magnets of storage rings operated for particle physics. Two examples were the DORIS (Double Orbit Ring System) at DESY and CESR (Cornell Electron-positron Storage Ring) at Cornell, which were later upgraded to 2^{nd} generation light sources [97]. The 2^{nd} generation light sources were necessary due to the changed demands of high-energy physics experiments: the geometry of the machines was changed in a way that longer arcs were installed to be

able to deliver more synchrotron radiation.
The 3^{rd} generation synchrotron light sources were optimized for smaller emittances and used many undulator straight sections. Synchrotron radiation emitted from bending magnets has a broad spectral range, which limits the brilliance to $B = 10^{12} mm^{-2} mrad^{-2} s^{-1} (0.1\%\text{bandwidth})^{-1}$, not sufficient for investigation of atomic strucrures [16]. In 1947 V. Ginzburg proposed the concept of the undulator, an array of alternating magnets whose field forces the electrons to move on sinusoidal trajectories as they pass through. The use of undulators decreases the radiated bandwidth and the opening angle, which increases the brilliance. As depicted in Figure 1.2, the undulator radiation has a narrower spectral range than the synchrotron radiation and can achieve peak brilliances in the order of $B = 10^{21} mm^{-2} mrad^{-2} s^{-1} (0.1\%\text{BW})^{-1}$. One important example is the PETRA III synchrotron light source at DESY [111], which is also one of the most brilliant 3^{rd} generation synchrotron light sources (see Figure A.1).

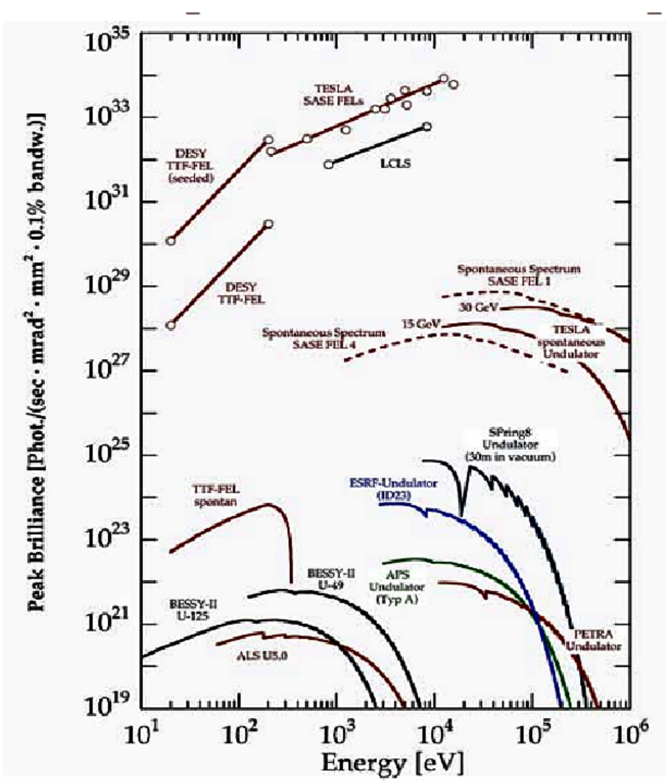

Figure A.1: Peak brilliance of synchrotron radiation sources as a function of photon energy, from [16]

Synchrotron Radiation has become the most successful and widespread advanced analytical tool for the determination of the properties of matter, based on a large infrastructure shared by thousands of users. Extremely brilliant beams of photons with energies ranging from 10eV to 300keV can be concentrated onto small samples, usually after monochromatization, and their scattering or absorption by the material under scrutiny provides invaluable information, from the atom positions in crystals and molecules, to the electronic and magnetic microscopic organization, to the mesoscopic and microscopic distribution of particles, defects and domains. Electromagnetic radiation is exceptionally well suited for these purposes as it interacts mainly with the electronic clouds of atoms, ultimately responsible for the chemical and physical properties of materials [89]; its wavelengths can be adjusted to match the interatomic distances to study structures with diffraction; their energy can be tuned to match electronic resonances to amplify signals and gain chemical selectivity. Ultraviolet and X-ray radiation is born inherently polarized in synchrotron sources and it can be highly monochromatized along the beam lines and focused down to micrometer scale at their end, offering further degrees of precision to the experiments. X-ray beams are compatible with intense magnetic and electric fields and can penetrate high pressure devices, allowing studies in extreme conditions of pressure, temperature and fields. For all these reasons Synchrotron Radiation has grown in popularity in the last 30 years, despite the drawback of requiring a high level of concentrated economical investment of modern Storage Rings (SR), at variance with "on campus" techniques, such as scanning probe and electron beam microscopy or laser based methods, that can be distributed on the territory [89].

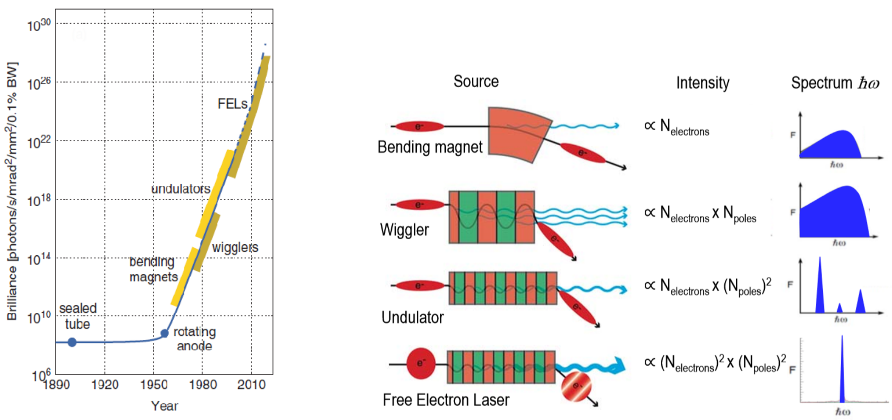

Figure A.2: Increase in brilliance due to new technologies (left), and Spectral range and intensity for different devices used in radiation sources, from [108]

Novel technologies, based on electron accelerators, lasers and their combination are determining the upgrade from the 3^{rd} to the 4^{th} generation of synchrotron radiation sources based on storage rings as well as the successful implementation of free-electron laser (FEL) sources and inverse-Compton scattering (ICS) light sources. The increase in brilliance as well as the spectral range covered by new technologies is shown in Figure A.2. Accelerator-based light sources produce short-wavelength,widely tunable radiation, either in storage rings (second or third generation) with partial transverse coherence, or in linear accelerators (linac) combined to FEL amplifiers (fourth generation). The 4^{th} generation light sources are introduced in the next section.

A.2 Free-Electron Lasers

Fourth generation light sources based on free-electron lasers (FELs) represent an invaluable in exploring nature at ultrasmall spatial and ultrashort temporal scales. In order to imagine a new class of electromagnetic radiation sources allowing experiments intrinsically impossible at storage ring based facilities, few fundamental parameters have to be considered: brilliance (A.1) and coherence of the beam. High peak brilliance means very many photons impinging on the sample in a very short time, allowing multi-photon processes to take place and/or time-resolved experiments to be realized. High average brilliance means more sophisticated and selective experiments carried out in a shorter experimental time. Optical coherence means that phases of propagating radiation wavefronts correlate and do not change with time: a coherent beam brings to some extent a control over the phase of the scattering photons, removing some ambiguities inherent in normal diffraction experiments [89]. In 1971 John Madey [112] came up with the revolutionary idea of the free-electron lasers [16], a new type of coherent and high brilliance radiation source whose basic scheme is sketched in Figure A.3 and which can be classified as the 4^{th} generation of light sources. The invention of the laser provided a revolutionary source of coherent

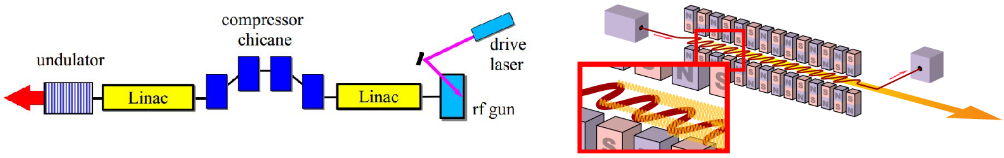

Figure A.3: Basic FEL scheme (left) and operation (right)

light that created many new fields of scientific research, and modern laser technology provides versatile performance throughout much of the electromagnetic spectrum. Optical resonators exist in the infrared, visible and ultraviolet regions, whereas nonlinear optics extends coverage toward shorter wavelengths (< 200nm) [43, 113]. However, the small nonlinear susceptibilities available at short wavelengths result in inefficient photon up-conversion. Particularly in the hard X-ray regime, the free-electron laser emerges as a promising source capable of producing unprecedented intensities. Although the radiation of accelerated electrons differs from radiation of conventional lasers, the bremsstrahlung of electrons in a periodic magnetic field can be stimulated by an externally applied radiation field as pointed out by Madey. Using a quantum mechanical description, where the stimulated emission is based on population inversion between quantum states of the electron beam, the analogy to conventional lasers became obvious [110, 113]. Because the electrons are not bound to any optical medium, such as atoms, molecules of crystals, Madey named this device Free-Electron Laser (FEL). Five years later Colson [114] published an equivalent description using classical mechanics, and the experimental verification was in 1976. The FEL emission mechanism is based on the coherent radiation emitted by a high-brightness relativistic electron beam passing the periodic field of an undulator magnet, which allows the number of curvatures to be increased and the radiation to

be reinforced, with a spectrum that is wavelength-adjustable over a wide range. The FEL thus transforms the kinetic energy of an electron beam into electromagnetic radiation with laser-like properties. A first advantage of such FEL over a conventional laser is that the electron bunch itself is the lasing medium, offering continuously tunable resonant wavelength by changing either the energy of the driving electron beam or the strength of the undulator field. On the contrary a conventional laser is always using an active material with the correct energy bands to reach a certain wavelength [113] and quantum energy gap limits the tuneability of the device: therefore the electron beam power in the case of FELs corresponds to the pump power in the case of conventional lasers. As shown later in appendix B, the resonant interaction between the transverse motion of the wiggling electrons, the undulator magnetic field, and the emitted transverse electromagnetic field leads to an instability that converts the electron kinetic energy into the electromagnetic radiation. As a result, the lasing phenomenon at the basis of FELs yields both ultra-short pulses (of the order of $10 - 100 fs$, about 1000 times shorter than in storage rings) and a high coherence (virtually 100%, 10 to 100 times better than in synchrotron beam lines). In addition the average flux (and brilliance) can be higher than in storage rings, depending on the repetition rate of the FEL [89]. Another important advantage with respect to solid-state sources of coherent radiation follows from the fact that the FEL process takes place in vacuum, so that the amplification is not constrained by dispersion/absorption processes. Furthermore, like synchrotron radiation sources, FELs are based on accelerator technology; but if synchrotron radiation is emitted incoherently by independently radiating electrons, the FEL process benefits from multiparticle coherence, combining the intensity and coherence of a laser with the broad spectral coverage of a synchrotron [43].
The FEL offers to the users the unique possibility of tailoring the radiation characteristics on the necessity of the specific application in operation. In fact, the FEL wavelength range can be opportunely varied, as well as bandwidth, power, temporal structure, thus allowing a number of design strategies, including multifrequency operation, polarization control, pump and probe configurations with naturally synchronized beams [12].

A.2.1 The oscillator and single-pass FEL Configurations

The FEL process tipically begins with a drive laser beam incident on a photocathode, by which electrons are emitted via photoelectric effect with a time structure replica of the laser pulse. Photo-injectors allow controlling the electron beam distribution by shaping the pulse of the laser used for the photoemission and are usually used in Linacs for FEL (SCSS at Spring8 in Japan is a notable exception [16, 108]). High gradient field promptly accelerates the electron beam.

Free-Electron Lasers can be grouped into three types of operation [43, 110, 113]

- FEL multi-pass oscillator
- FEL single-pass amplifier

- Self Amplified Spontaneous Emission (SASE) FEL

The first basic FEL scheme presents an undulator within an suited high-Q optical cavity allowing the radiation power to build up during the passes of several electron bunches in the undulator until an equilibrium state is reached at saturation. The FEL oscillator is started by the spontaneous emission and the shot noise of the electron beam, and the interaction between trapped light and electron bunches lead to micro-bunching and fully temporal coherent emission [43, 110]. The characteristics of the FEL, such as the transverse size of the radiation field and the synchronization between radiation pulse and electron beam, are strongly influenced by the optical cavity. FEL gain does not need to be very high and accelerator requirements are reasonable.

Oscillator (low gain) FELs are used if the electron beam peak current is low, thus many passes through the undulator are necessary to reach saturation, and if broad-band extraction mirrors are available [16]. In order to couple out radiation from the optical cavity an old extraction mechanism, the so-called hole coupling, is used: an aperture in the center of one of the cavity-building mirrors is used as a broad-band extraction mechanism. The technological lack of reasonably reflective mirrors below $100nm$ has restricted their use during the first two decades of the operation of free-electron lasers, in a wavelength range from THz to UV [105].

In most FELs in the infrared regime (IR-FELs) oscillators are used, for example in FELIX and ELBE. In this respect, it is worth mentioning the studies [115] on regenerative FEL oscillators operating in large-gain regime and the detailed studies [58] aimed at extending their operation at short wavelengths, relying on Bragg reflectors as mirrors [27].

For wavelength in the deep UV and beyond, no broad-band high reflectivity mirrors for normal incidence are available. Therefore, one has to limit a machine to one fixed wavelength and use multi-layer mirrors [specchi] or needs to have saturation within one single pass of the undulator [16].

With a new generation of injectors, based on photo-electron guns, the electron beam quality became sufficient to reach saturation of the FEL amplification within a single pass of the electron bunch through the undulator. In single-pass (high gain) FELs, the FEL is an amplifier: an external radiation field seeds the FEL and gets amplified by the interaction with an electron beam of high peak current in an undulator with increased length, having a similar effect but with only limited longitudinal coherence. Single pass FELs were developed on the basis of theoretical works in the 1980s and have been used since the 1990s for wavelength regimes from UV down to X-rays. The basic working principle of an FEL can be explained best by this device (see Appendix B).

A straightforward approach to single-pass amplification is the SASE FEL, where the seeding field is supplied by the spontaneous emission emitted at the beginning of the undulator. Because the bandwidth of the spontaneous emission spectrum is larger than the FEL amplification bandwidth, the SASE FEL is always tuned to the resonant frequency with the largest growth rate. In this case, the accelerator performances should fulfill the best qualities in terms of low emittance, high brightness

electron beam, short pulse [31].
The electron bunch used in a SASE FEL consists of stochastically distributed electrons and the emitted radiation between the different trains of bunches is not correlated. The radiation pulse of a SASE FEL has an enormous peak power ($\sim GW$) together with quite high transverse coherence, but the random phase and amplitude of the initial shot noise limit its longitudinal coherence ($\tau_c \ll \tau_{pulse}$), resulting in strong pulse-to-pulse fluctuations in both the spectral and temporal domains. As a matter of fact, the output radiation power and spectrum feature several radiation spikes, where the duration of one spike as well as the complete spectral width are about the coherence time τ_{coh}. Furthermore, a short SASE pulse requires an equally short electron bunch, which is beyond the state of the art below a few hundred femtoseconds [31].

The choice of FEL configuration and radiation scheme is based on user-defined requirements of the properties of the output FEL pulses, as radiation wavelength, peak power, polarization and required average repetition rate. The time structure of the pulse has to be matched to the characteristic timescales of the physical processes under study. An example is given by X-ray imaging and other high intensity applications, where the photons should be delivered in ultra-short, high-intensity pulses. On the other hand, spectroscopic studies require limited peak intensity so as to avoid non-linear processes, but also a high repetition rate in order to collect sufficient data in acceptable experimental periods.
In Chapter 2, we discussed the state of the art regarding new schemes for modern FELs aimed at increasing both its spatial and temporal coherence.

A.2.2 Science with FEL radiation

Electromagnetic radiation from FELs must be used for experiments otherwise impossible with the more traditional synchrotron radiation sources. Table A.1 highlights the advantage of using FELs in experiments, compared to other light sources, while Figure A.4 (see next page) reports the time scales accessible by FEL based experiments [89].

Table A.1: Light sources properties compared

Source	Photon Flux	Tuneability	Brilliance
X-ray tube	Low	No	Low ($\sim 10^7$)
Synchrotron	High	Yes	High average ($\sim 10^{22}$)
FEL	Medium	Yes	High peak ($\sim 10^{33}$)

The interest in X-ray FELs is motivated by their characteristics of tuneability, coherence, high peak power, short pulse length which allow to explore matter at the length and time scale typical of atomic and molecular phenomena [89].
With the peak brilliance of an FEL, one has many photons ($10^{11} - 10^{13}$ photons

reaching the sample in a $10 - 100$fs flash). Usually this light is concentrated in a focal spot of few micron diameter and is absorbed in a depth of the order of 1 micron in condensed matter. This means that, on average, every atom in the interaction volume absorbs or scatters one photon in a time of few tens of femtoseconds: a very strong perturbation to the system, that often leads to the explosion of molecules and the sublimation of solid samples if the intensity of the beam is not reduced [89].

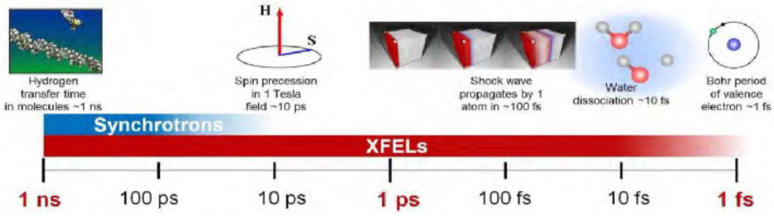

Figure A.4: Time scales accessible by FEL based experiments, from [89]

Whenever possible, the sample is made to flow, as gas or liquid or microcrystal suspension in a liquid, and automatically fresh sample is exposed to each flash of UV or X-ray radiation. But even then one has to be confident that the alteration in the molecular and electronic structure does not happen before the radiation pulse has finished interacting with the sample: it is the " diffract before destroy" approach. The same approach is much more difficult to realize in the case of solids, even if one thinks of moving the sample continuously under the beam; therefore, the pulse energy is usually reduced when dealing with solids [89].

The large number of photons per pulse allows to determine the structures of complex molecules or nanosystems in a single shot, to study non linear phenomena and high energy density systems. The transverse coherence gives new possibilities of imaging at the nano and sub-nano scale. An X-FEL opens a new physics, leading to the observation of new interesting processes like: make movies of chemical dynamics in action, study the structure and time-resolved function of single molecules, do 3D imaging and dynamical studies of the bio-world, solve the transient structure of liquids, characterize the transient states of matter created by radiation or pressure.

A.2.3 X-Ray Free electron Lasers scenario

The panoramic picture sketched in Table A.2 has to be evaluated in the context of existing and future FEL sources worldwide. The pioneers have been LCLS in Stanford (USA), covering the soft X-ray and hard X-ray ranges, SACLA in Japan (hard X-ray only) and FLASH in Hamburg (Germany) for VUV; all these are SASE sources, with low effective number of pulses per second (50-100). FERMI@ELETTRA in Trieste is the only seeded FEL in operation, in the VUV range to be extended to the very soft X-rays: the seeding has there demonstrated its feasibility and exceptional gain in quality of the experimental output. More recently the European X-FEL has started operations in Hamburg, with a non-uniform time structure leading to 27000 pulses per second organized in 10 trains of 2700 pulses and a time between pulses of $220ns$. The European X-FEL covers the soft and hard X-ray ranges and is based on a superconducting Linac [89].

Table A.2: X-ray FEL facilities panorama, from [89]

XFEL Facility	**N. Und. Sources**	**X-ray Energy Range**	**Repetition Rate**	**Linac**
LCLS-I (U.S.)	1	0.25 to 12.8 keV	120 Hz	warm Cu 15 GeV
LCLS-II (U.S.)	2	0.25 to 5 keV 0.25 to 25 keV	up to 1 MHz 120 Hz	CW-SCRF 4 GeV
LCLS-II-HE (U.S.)	2	0.25 to 12.8-20 keV	up to 1 MHz	CW-SCRF 8 GeV
SACLA (Japan)	2(3)	5 to 20 keV	60 Hz	warm Cu 8 GeV
PAL-FEL Republic of Korea	2	0.3 to 20 keV	60 Hz	warm Cu 10 GeV
Swiss-FEL (Switzerland)	2	0.2 to 12 keV	100 Hz	warm Cu 5.8 GeV
European XFEL (Germany)	3(5)	0.2 to 25 keV	28 kHz (effective) in 10 Hz bursts	Pulsed-SCRF 17.5 GeV
FLASH (Germany)	2	0.03 to 0.3 keV	5 kHz (effective) in 10 Hz bursts	Pulsed-SCRF 1.2 GeV
FERMI (Italy)	2	0.01 to 0.3 keV	50 Hz	warm Cu 1.5 GeV

As shown in Table A.2, the next generation of FEL is represented by LCLS-II (expected to be running from 2020), an upgrade of LCLS with a superconducting Linac capable of providing 106 pulse per second, equally spaced by $1\mu s$. It will cover the soft and "tender" X-ray range, up to $5keV$. The hard X-ray range $(5-20keV)$ will be covered by a "warm" Linac working at $120Hz$, but a proposal for the extension of the full energy range to the MHz repetition rate (LCLS-II HE) is under scrutiny in the US [89]. This last upgrade is motivated by the fact that the $5-12keV$ photon energy range is extremely useful because it allows diffraction experiments and covers the K absorption edges of 3d transition metals, which are among the most important elements in materials science and not only.

Appendix B

Free Electron Laser Theory

This Appendix gives an overview of the theoretical description of a Free-Electron Laser (FEL), and the case of an FEL amplifier is treated because it exhibits the FEL physics in its simplest form.
The motion of the electrons within the undulator field, excluding interaction with the radiation field, is derived in section B.1. Section B.2 includes an external radiation field, which might be the spontaneous emission or an external seed. Then, in the approximation of a nearly constant amplitude of the radiation, the equations of a low-gain FEL are discussed.
On the basis of the self-consistent FEL equations, including Maxwell's equation for the radiation field, the 1D FEL model of an high-gain FEL is discussed (Section B.3). This model is capable to analyze the fundamental characteristics of a high-gain FEL. Section B.4 derives the power scaling laws in different cases, highlighting the difference between SASE and seeded FELs. The remaining section briefly extends the 1D model to radiation field diffraction and other 3D effects.

B.1 Electron Motion in an Undulator

The hardware part of a Free-Electron Laser (FEL) is an undulator or wiggler. Its main purpose is to force the electrons to oscillate ('wiggle') while moving through. This transverse motion causes the electron beam to emit synchrotron radiation, which is confined to a forward cone whose opening angle is the inverse of the Lorentz factor $\gamma = (\sqrt{1-\beta^2})^{-1}$ for relativistic electrons, where E is the electron energy, m is the electron mass, c is the speed of light in vacuum and β its velocity normalized to c [110].
The main feature of an undulator and wiggler is a series of paired magnets along the main axis, placed opposite to each other and separated by a gap. If the plane of the gap is fixed, the undulator or wiggler is planar, while the helical undulator involves the rotation of the magnets along the main axis in the form of a double helix.
Following Refs. [35, 110, 116], a Cartesian coordinate system, where the z-axis coincides with the undulator axis, will be considered throughout this Appendix . The transverse coordinates x and y are chosen so that the magnetic field for a planar un-

dulator or wiggler is parallel with the y-axis (see Figure B.1). Due to the rotational symmetry, the choice of the coordinate system orientation for the helical undulator is arbitrary.

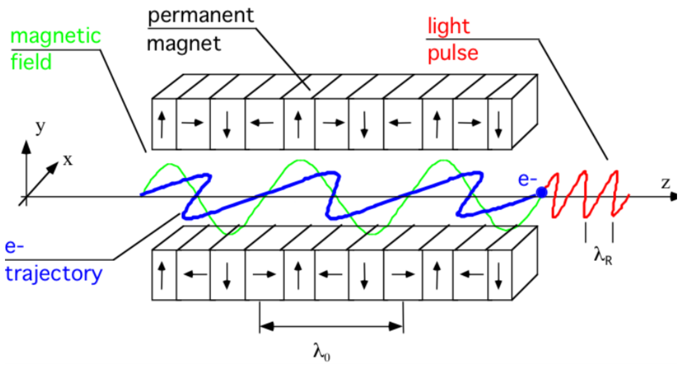

Figure B.1: Undulator sketch and coordinate system

Both undulators and wigglers are used for Free-Electron Lasers, and they differ in the deflection strength of the magnetic field (see Figure A.2). If the maximum deflection angle is larger than the opening angle of the spontaneous emission there is no continuous emission in the forward direction, resulting in a wiggler. The spectrum observed is enriched by higher harmonics of the periodic signal of the detected radiation. Undulator radiation is modulated but not pulsed in the forward direction, and the number of higher harmonics in the spectrum is reduced [110].

B.1.1 The Planar Undulator

The case of a planar undulator will be considered, and the main differences with an helical undulator will be highlighted. The magnetic field on the undulator axis is a harmonic function of the longitudinal position z:

$$B_y(z, x = 0, y = 0) = B_0 \cos(k_w z) \tag{B.1}$$

The field points in the y-direction and has an amplitude B_0 and wavenumber $k_w = 2\pi/\lambda_w$. Within the free space of the undulator gap, Maxwell's equations for a static magnetic field require that $\nabla \cdot B = 0$ and $\nabla \mathrm{x} B = 0$. The second condition determines the dependence of the magnetic field on the transverse coordinates [110].
The electron motion can be conveniently split in two parts

$$\vec{r}(t) = \vec{r_0}(t) + \vec{R}(t)$$

separating the main quickly varying oscillation $\vec{r_0}(t)$ due to the periodic undulator field from a drift $\vec{R}(t)$ in the transverse position with a characteristic length on the scale of many undulator periods (thus assumed to be constant at first order).
The equations of motion for the position $\vec{r}$ and canonical momentum $\vec{P}$ of a single

electron are obtained from the Hamilton formalism, using the Hamilton function of a relativistic electron [110]

$$H = \sqrt{(\vec{P} - e\vec{A})^2c^2 + m^2c^4} + e\Phi \tag{B.2}$$

where Φ is the scalar potential of the electric field $\vec{E}$, with $\vec{E} = -\vec{\nabla}\Phi - \partial\vec{A}/\partial t$.
The motion can also be obtained starting from

$$m\gamma\frac{\mathrm{d}\vec{v}}{\mathrm{d}t} = e\vec{v} \times \vec{B} \tag{B.3}$$

where $\vec{B} = (0, B_y, 0)$ so that the resulting motion takes place in the xz-plane with the 'fast' velocity given by

$$m\gamma\frac{\mathrm{d}\vec{v_x}}{\mathrm{d}t} = e\vec{v} \times \vec{B} = e(v_yB_z - v_zB_y) \tag{B.4}$$

thus

$$\dot{x_0} = v_{x,0} = -\frac{e\hat{B}}{m\gamma}\int \cos(k_wz)v_z\mathrm{d}t = -\frac{\sqrt{2}cK}{\gamma}\sin(k_wz) \tag{B.5}$$

where the identity $v_zdt = dz$ was used.
Eq. (B.5) suggests the definition of the dimensionless deflection parameter of the undulator field

$$K = \frac{e\hat{B}}{mck_w}\left(1 + \frac{k_x^2}{2}X^2 + \frac{k_y^2}{2}Y^2\right) \tag{B.6}$$

depending to second order on the transverse position $X = X(t)$ and $Y = Y(t)$ of the 'slow' trajectory $\vec{R}(t)$. As in [110], this definition uses the root-mean-square value $\hat{B}$ instead of the on-axis peak field B_0 (in the case of a planar undulator $\hat{B} = B_0/\sqrt{2}$). The advantage of this definition is that many equations remain the same for the case of the helical undulator. The value of K at the undulator axis $(X, Y = 0)$ defines the undulator parameter, which for a planar undulator is given by

$$a_w = \frac{eB_0}{\sqrt{2}mck_w} \tag{B.7}$$

and can be expressed in practical units as $a_w = 6.57\text{x}10^{-2}B_0\,[T]\,\lambda_w\,[mm]$.
Since the second order corrections to the undulator field are of the order of 10^3, the transverse dependence of the undulator field has a negligible impact on most of the calculations and it is sufficient to use the constant value of the undulator parameter a_w instead [110].
Eqs. (B.6-B.7) exhibits the distinction between wiggler and undulator. If the electron is relativistic ($z \approx ct$, $\gamma \gg 1$), the maximum divergence of the electron is $x' = \dot{x_0}/c = \sqrt{2}K/\gamma$, where the opening angle of the synchrotron radiation is γ^{-1}: the device is an undulator for $K \leq 1/\sqrt{2}$ ($K \sim 1$) and the radiation is a coherent overlap of all the trajectory oscillations, while it is a wiggler otherwise ($K \gg 1$) and the radiation is a series of light pulses.

The motion in the y-direction consists only of the 'slow' motion ($y_0(t) = 0$) thus the electrons' oscillation is perpendicular to the magnetic field direction.
Due to energy conservation, the longitudinal velocity can directly be obtained from the definition of the Lorentz factor γ and the normalized velocity $\vec{\beta} = \mathrm{d}\tilde{\mathrm{r}}/c\mathrm{dt}$. Then the longitudinal velocity is

$$\begin{aligned}\beta_z &= \sqrt{1 - \frac{1}{\gamma^2} - \beta_x^2 - \beta_y^2} \\ &\approx 1 - \frac{1+K^2}{2\gamma^2} - \frac{\beta_R^2}{2} + \frac{K^2}{2\gamma^2}\cos(2k_w z)\end{aligned} \tag{B.8}$$

where β_R is the transverse velocity of the slow drift, normalized to c (neglected in the next passages). The cross term proportional to $\beta_R K/\gamma \sin(k_w z)$ has been neglected because it is either small compared to the leading oscillating term ($\propto K^2 \cos(2k_w z)$) or not resonant with variation of β_z as is the case for $\beta_R^2/2$ [110]. The transverse motion slows down the electron by $\Delta\beta_z = K^2/2\gamma^2$ with a superimposed longitudinal oscillation with a period half as long as the transverse oscillation.

To obtain the trajectory $x_0(t)$, the longitudinal position is approximated by $z = c\beta_z t \approx c\beta_0 t$ and then Eq. (B.5) is integrated in first order, using the averaged velocity

$$\beta_0 = 1 - \frac{1+a_w^2}{2\gamma^2} \tag{B.9}$$

where we replaced K by a_w of Eq. (B.7). The integration yields

$$x_0(t) = \frac{\sqrt{2}a_w}{\gamma k_w \beta_0}\cos(ck_w\beta_0 t) \tag{B.10}$$

The longitudinal oscillating term in Eq. (B.8) is the source of a phase modulation in the cosine function in Eq. (B.10). As a consequence, the transverse oscillation exhibits higher harmonics of the fundamental wavenumber k_w.
The treatment of the helical undulator is very similar to that of the planar one and goes beyond our aims.

B.2 The Interaction of Electrons with a Radiation Field in an Undulator

In this section the interaction of electrons with a radiation field, either from an external master oscillator or from the incoherent spontaneous synchrotron radiation, while they move through the undulator is analyzed. The approach to this problem is similar to that in the previous section except that an additional term in the Hamilton function (B.2) describes the vector potential of the radiation field [110]. If the emission of radiation is stronger than the absorption, the electrons are losing energy in average and the radiation field is amplified. As long as this amplification is small, the radiation field amplitude can be assumed to be constant. The limitations of this model of a 'low gain' Free-Electron Laser are given at the end of this section, and a more self-consistent model of an FEL can be found in the next section, including Maxwell's equation for the radiation field description. Nevertheless a discussion of the low gain FEL shows the basic principle of FEL emission with rather simple equations.

The interaction of charged particles with a radiation field shows two major aspects [110]. The first is the energy exchange between the electrons and the radiation field, thus a change of the particle momentum and energy. The second aspect is the change of the radiation field itself. The fast transverse oscillation of the relativistic electrons, induced by the undulator magnets, is a source of radiation that points mainly in the forward direction of the electron beam motion.
Under special conditions both processes are the source of a collective bunching of the electrons on a resonant frequency and the radiation field is strongly amplified. The next sections analyze this instability, which is the working principle of the "high gain" FEL. In contrast to the high gain FEL, the low gain FEL provides an amplification without the necessity of a strong modulation in the electron density [110].

The electric field components are lying in the transverse xy-plane, thus only a transverse motion, along or against the field orientation, changes the electron energy. Due to the symmetry of the magnetic field, the radiation emitted in a planar undulator is linearly polarized while it is circularly polarized for the case of a helical undulator. In this section the case of a planar undulator is regarded. The electric field component of the radiation field

$$\vec{E} = \vec{E_0} \cos(k(z - ct) + \phi) \tag{B.11}$$

is defined by its amplitude $\vec{E_0}$, its wavenumber $k = 2\pi/\lambda$ or wavelength λ, and its initial phase ϕ at the undulator entrance[1].
The amplitude E_0 and the phase ϕ depend on z due to diffraction, which is considered in section b.5. The dependence becomes negligible if the transverse extension of the radiation wavefront is much larger than the radiation wavelength [35, 109, 110].
The change of the electron energy is caused only by the electric field components, which, depending on the radiation phase, accelerate or decelerate the electron with

$$\begin{aligned}\dot{\gamma} = e\frac{\vec{E}\cdot\vec{\beta}}{mc} &= \frac{e}{mc^2}\begin{bmatrix} v_x \\ 0 \\ v_z \end{bmatrix} \cdot \left(\begin{bmatrix} E_x \\ 0 \\ 0 \end{bmatrix} + \begin{bmatrix} v_x \\ 0 \\ v_z \end{bmatrix} \mathrm{x} \begin{bmatrix} 0 \\ B_y \\ 0 \end{bmatrix} \right) \\ &= \frac{e}{mc^2}\begin{bmatrix} v_x \\ 0 \\ v_z \end{bmatrix} \cdot \begin{bmatrix} E_x - v_z B_y \\ 0 \\ v_x B_y \end{bmatrix} = e\frac{E_x \beta_x}{mc}\end{aligned} \tag{B.12}$$

[1]The magnetic field component is perpendicular to $\vec{E}$ as well as to the unit vector in the direction of propagation, which mainly coincides with $\hat{e_z}$. Compared to the strong undulator field, the magnetic field of the radiation field is negligible and can be ignored in the further discussion.

where we note that the transverse wiggle motion is necessary for the interaction (the second equality follows from considering the case of planar undulator and linearly polarized radiation field).
In order to have a net energy transfer to the radiation field, the electrons and the light wave have to move in the same direction throughout the undulator. This is not obvious since light moves faster and slips with respect to the electron beam, thus electrons should fall back by the right amount behind the light. Intuitively from Figure B.2, one sees that the light has to slip by one wavelength in one undulator period λ_w [109].

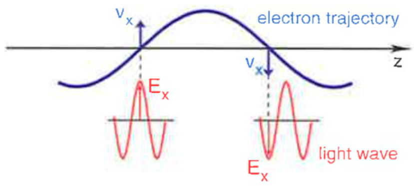

Figure B.2: Slippage of the radiation field with respect to the electron beam. When the electron moves along one undulator period λ_w, the radiation field slips by a wavelength λ, from [109]

Indeed, one has $\lambda + \lambda_w = c(\lambda_w/v_z)$ therefore after a length $L_w = N_w\lambda_w$ (with N_w number of undulator periods) the radiation slips by $L_s = N_w\lambda$, the so-called *slippage length*.
The new equation of motion will contain the electric field term and reads

$$m\gamma\frac{\mathrm{d}\vec{v}}{\mathrm{d}t} = e(\vec{E} + \vec{v} \times \vec{B})$$

Solving this equation, as well as inserting the vector potential of the radiation field and the undulator field into the Hamilton function, the transverse velocities are [110]

$$\begin{aligned}\dot{x} &= -\frac{\sqrt{2}cK}{\gamma}\sin(k_w z) - \frac{\sqrt{2}cK_r}{\gamma}\sin(k(z-ct)+\phi) + \dot{X} \\ \dot{y} &= \dot{Y}\end{aligned} \tag{B.13}$$

The dimensionless radiation amplitude

$$K_r = \frac{e\hat{E}}{mc^2k} \tag{B.14}$$

is defined in an analogous way as the undulator parameter K (b.6) (the motivation to use the root-mean-square value $\hat{E}$ of the electric field is the same).
For sake of simplicity, any transverse variation of the radiation field is here excluded.

For small transverse momenta, the longitudinal velocity is approximately

$$\begin{aligned}\beta_z \approx\; & 1 - \frac{1+K^2+K_r^2}{2\gamma^2} - \frac{\beta_R^2}{2} \\ & + \frac{K^2}{2\gamma^2}\cos(2k_w z) + \frac{K_r^2}{2\gamma^2}\cos(2k(z-ct)+2\phi) \\ & - \frac{2KK_r}{2\gamma^2}\sin(k_w z)\sin(k(z-ct)+\phi)\end{aligned} \tag{B.15}$$

The electric field forces an additional transverse oscillation with the frequency of the electromagnetic wave. The longitudinal velocity is slowed down and modulated with an oscillation of twice the frequency of the radiation field. The cross term $\propto KK_r$ can be split into two independent oscillations [110]: if one of them has a small frequency, it can significantly change the longitudinal velocity β_z on a time scale different to the dominant oscillating term $\propto K^2$.
Combining all constant or slow varying terms to β_0, the integration of Eq. (B.15) up to first order yields

$$z = \beta_0 ct + \frac{a_w^2}{4\gamma^2 k_w \beta_0}\sin(2k_w\beta_0 ct) \tag{B.16}$$

With the given expression of the transverse velocities $\dot{x}$ and $\dot{y}$, Eq. (B.12) can be evaluated. Most of the cross terms between E_x and β_x are fast oscillating. Over many undulator periods, the net change of the electron energy is negligible.
The only possible term that might be constant is the product of $\cos(k(z-ct)+\phi)$ and $\sin(k_w z)$, similar to the term in Eq. (B.15). Therefore inserting Eqs. (B.11) and (B.13) into Eq. (B.12) yields the resonant term

$$\dot{\gamma} = -\frac{2ckKK_r}{\gamma}\cos(k(z-ct)+\phi)\sin(k_w z) \tag{B.17}$$

This term is split into two independent oscillations

$$\sin(k_w z)\cos(k(z-ct)) \sim \sin\left[(k-k_w)z - kct\right] + \sin\left[(k+k_w)z - kct\right]$$

with the phases $\theta = (k+k_w)z - kct + \phi$ (the so-called *ponderomotive phase*) and $\psi = (k-k_w)z - kct + \phi$. If one of the phases remains almost constant, the energy change is accumulated over many periods.
With an average longitudinal velocity of $c\beta_0$, the phase relation between electron and radiation field remains unchanged ($\dot{\theta} = 0$, $\dot{\psi} = 0$ respectively) if the condition

$$\beta_0 = \frac{k}{k \pm k_w} \tag{B.18}$$

is fulfilled. As shown later in this chapter, the interaction between the electron beam and the radiation field needs to add up resonantly over many undulator periods to result in a significant change of the electron energy or radiation amplitude

and phase [109,110]. This implies that, for a given beam energy and undulator wavelength, the wavelength of the radiation field is well defined according to Eq. (B.18). The case of the '-' sign, corresponding to the condition $\dot{\psi} = 0$, is excluded because it would demand an electron velocity v_z faster than the speed of light to keep the electrons in phase with the radiation field for any time.
In the limit of a weak electric field ($K_r \propto E_0 \to 0$) and a small beam emittance, β_0 is identical with Eq. (B.9). The restriction to a well defined resonant radiation wavelength is called *resonance approximation.*
Considering $K = a_w$, the resonant radiation wavelength is

$$\boxed{\lambda = \frac{\lambda_w}{2\gamma^2}(1 + {a_w}^2)} \tag{B.19}$$

This important equation is valid for a planar and a helical undulator as well, and shows the tune-ability of an FEL by changing the electron energy or the undulator field strength (by changing the gap for permanent magnet insertion devices or the power supply current for electromagnetic insertion devices). A transverse betatron motion and a stronger radiation field shift slightly the resonance condition towards longer wavelength. If Eq. (B.19) is exactly fulfilled, the energy change is constant over many undulator periods pushing the electron off-resonance. We call γ_R the resonant energy satisfying Eq. (B.19), thus

$$\gamma_R = \left[\frac{k}{2k_w}(1 + a_w^2)\right]^{\frac{1}{2}} \tag{B.20}$$

The ponderomotive phase is the relative phase between v_x and E_x. If the resonance condition is fulfilled, it corresponds to a wave along the bunch that moves with the speed of the bunch v_z. The wavelength of θ is λ, which is the distance between two micro-bunches. Due to the made assumptions, the longitudinal bunching is periodic and it suffices to study the range $\theta = [-\pi/2, 3\pi/2]$ in which one micro-bunch will sit [35, 109].

For the case of a helical undulator, the amplification of higher modes is much smaller because the dominant longitudinal oscillation, which is the reason for the coupling to higher harmonics, is strongly suppressed [110]. At the fundamental frequency the synchronization of the phase front of the ponderomotive wave and the electrons is almost perfect, while it is reduced by the kinematic factor $(J_0(\chi) - J_1(\chi))$ for the planar undulator with $\chi = kK^2/4\gamma^2 k_w$ (=$K^2/(4 + 2K^2)$ for the fundamental resonant wavelength).

Compared to the fast changing position of the electron $z \approx \beta_0 ct$, the ponderomotive phase $\theta = (k + k_w)z - ckt$ of the electron is almost constant if on-resonance.

The equation of motion becomes

$$\begin{aligned}\frac{\mathrm{d}\theta}{\mathrm{d}t} &= (k+k_w)c\beta_z - kc \\ &= c(k+k_w)\left(1-\frac{1+a_w^2}{2\gamma^2}\right) - ck \\ &\sim ck_w\left[1-\frac{k(1+a_w^2)}{k_w\gamma^2}\right] \\ &= ck_w\left(1-\frac{\gamma_R^2}{\gamma^2}\right)\end{aligned} \tag{B.21}$$

with the definition of γ_R (B.20) and assuming $k \propto \gamma_R^2 k_w \gg k_w$.
For small energy deviations $\gamma \sim \gamma_R$,

$$\frac{\mathrm{d}\theta}{\mathrm{d}t} = 2ck_w\frac{\gamma-\gamma_R}{\gamma_R} \tag{B.22}$$

which suggests the introduction of the normalized electron energy variable

$$\eta = \frac{\gamma-\gamma_R}{\gamma_R} \rightarrow \frac{\mathrm{d}\theta}{\mathrm{d}t} = 2ck_w\eta$$

As regards the equation for the energy transfer (B.17), it can be simplified to

$$\frac{\mathrm{d}\gamma}{\mathrm{d}t} = -\frac{ea_wE_0}{2\gamma_R mc}\cos(\theta) \rightarrow \frac{\mathrm{d}\eta}{\mathrm{d}t} = -\frac{ea_wE_0}{2\gamma_R^2 mc}\cos(\theta) \tag{B.23}$$

To evaluate Eq. (B.23), the sine and cosine function are replaced by complex exponential functions. The oscillating part of the longitudinal motion (Eq. B.16) can be expanded into a series of Bessel functions by the identity [110]

$$e^{ia\sin b} = \sum_{m=-\infty}^{\infty} e^{imb}J_m(a) \tag{B.24}$$

The result is a sum of exponential functions with the frequencies $[(k+(2m+1)k_w)\beta_0 - k]c$. Beside the ground mode with $m=0$, some terms are resonant at different wavelengths. The frequencies of these are the odd harmonics of the resonant frequency $\omega_0 = ck_0$. Thus the longitudinal oscillation induces higher harmonics in the motion of the electrons.
For completeness, it is noted that a transverse non-uniform radiation field couples the particle motion also to the even harmonics of ω_0. If the radiation field is expanded into a Taylor series around the electron position of the betatron oscillation $(x = X + x_0)$

$$\vec{E}(x) = \vec{E}(X) + \left.\frac{\mathrm{d}\vec{E}}{\mathrm{d}x}\right|_X x_0$$

the factor $x_0\dot{x}_0$ is proportional to $\sin(2k_w z)$ in Eq. (B.16) and the complex exponential functions have the arguments $[(k + (2m+2)k_w)\beta_0 - k]ct$, being resonant at all even harmonics. The resonant frequencies are well separated such that only one resonance frequency is of importance for a given radiation field. The interaction is the strongest for the fundamental mode, which is the only mode considered in the following discussion.

The longitudinal phase space of one electron can be described by the two coupled first-order differential equations for the rates of change of electron's phase and energy [35, 109]

$$\begin{cases} \frac{\mathrm{d}\theta}{\mathrm{d}t} = 2ck_w\eta \\ \frac{\mathrm{d}\eta}{\mathrm{d}t} = -\frac{ea_w E_0}{2\gamma_R^2 mc}\cos\theta \end{cases} \tag{B.25}$$

The phase space motion of N electrons at a constant radiation field amplitude, as the one of a seed laser, obeys the familiar pendulum equation

$$\frac{\mathrm{d}^2\theta}{\mathrm{d}t^2} + \Omega_s^2\cos\theta = 0 \tag{B.26}$$

with the synchrotron oscillation frequency

$$\Omega_s^2 = \frac{eE_0 a_w k_w}{2m\gamma_R^2} \tag{B.27}$$

which can be considered constant in the low gain regime.
In literature [34, 114, 116–118], another widely used notation for the FEL pendulum equation (B.26) is that of Colson's dimensionless parameters

$$\frac{\mathrm{d}^2\theta}{\mathrm{d}\tau^2} = |a|\cos(\theta + \phi)$$

with the dimensionless time $\tau = tc/L_w$ ($L_w = N\lambda_w$ being the undulator length). The electron relative phase with respect to the radiation field is denoted by $\theta(\tau)$, $|a|$ and ϕ are the amplitude and phase of the dimensionless optical field a (B.44)

$$a = \frac{eJJa_w N_w \lambda_w}{\gamma_R^2 mc^2} E_x$$

Integration of Eq. (B.26) yields

$$\frac{1}{2}\left(\frac{\mathrm{d}\theta}{\mathrm{d}t}\right)^2 - \Omega_s^2\sin\theta = U = \text{const} \tag{B.28}$$

Figure B.3 (see next page) shows the electron's phase space trajectory in the combined system of the radiation field and the undulator. The dashed lines are the phase-space trajectories, and the solid red line is the *separatrix*, which is the boundary between stable and un-trapped trajectories. The region inside the separatrix is

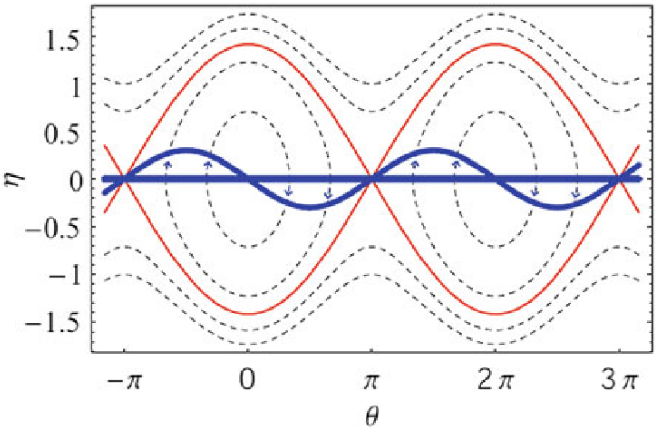

Figure B.3: Electron phase space trajectory, from [109]

called *bucket*. The initial distribution (blue line) depicts mono-energetic electrons at time $t = 0$. The FEL interaction causes the electrons to gain or lose energy depending on their ponderomotive phase [35, 109].
The initial ponderomotive phases of the electrons are almost uniformly distributed over 2π. Due to the finite number of electrons over one radiation wavelength, a small modulation of the electron beam remains. This spontaneous emission provides the initial radiation field for Self-Amplified Spontaneous Emission Free-Electron Laser [109, 110] (SASE FEL).
In the centre of the FEL bucket ($\theta = 0$) there is no change of η. Electrons with $\theta \in [2n\pi, (2n+1)\pi]$ lose energy and move to the bottom of the bucket, electrons with $\theta \in [(2n-1)\pi, 2n\pi]$ gain energy and move to the top of it. At 1/4 of the synchrotron period, the electrons have sinusoidal energy modulations, which causes the electrons to develop density modulation with the period of the radiation wavelength. At 1/2 of the period, FEL bunching is maximum [35, 109].
The untrapped electrons flowing around the separatrix also provide gain (linear regime) until the separatrix grows and captures them (non linear regime).

As depicted in Figure B.4, electrons with energy above the resonant energy γ_R move lower and provide FEL gain, while electrons below γ_R absorb FEL radiation.

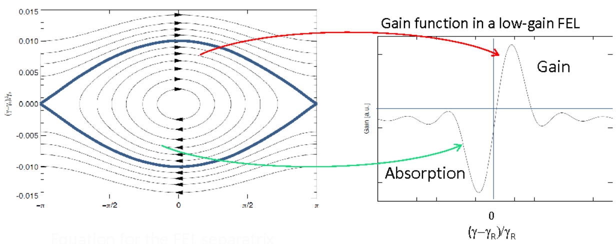

Figure B.4: Gain function in a low-gain FEL, from [109]

Madey's theorem expresses the relative energy gain G of the light wave for one pass of the undulator in a low gain amplifier, by considering that the radiation energy change is equal to the lost electron beam energy and tracking many particles [35, 109, 110].

$$G(\xi) = -\frac{\pi e a_w^2 N_w^3 \lambda_w^2 n_e}{4\epsilon_0 m_e c^2 \gamma_R^3} \cdot \frac{\mathrm{d}}{\mathrm{d}\xi} \frac{\sin^2 \xi}{\xi^2} \tag{B.29}$$

where n_e indicates the electron charge density and with $\xi = 2\pi N_w \eta$ (N_w=number of undulator periods). The theorem states that the line-shape of the small-signal gain of a low-gain FEL is the negative frequency derivative of the intensity spectrum of the spontaneous emission curve, a sinc-square function.
As pointed out in [35], the small-signal gain can be calculated from the energy gained by the radiation in each pass divided by the radiation energy, using second-order perturbation theory and obtaining the gain curve in Figure B.5

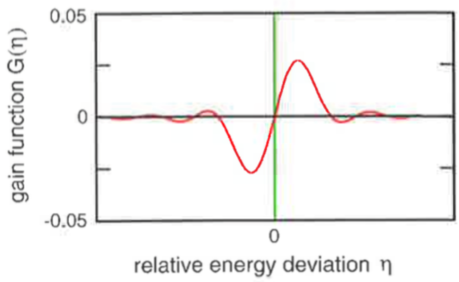

Figure B.5: Small signal gain curve in a low gain FEL, from [35]

It is clear that particles have to be injected with an average energy γ higher than the resonant energy γ_R to get the radiation amplified. For $\eta = 0$ there's no energy gain, but this is not the case in the high-gain theory (see later).
FEL oscillators and SASE FELs start from the spontaneous emission with a broad bandwidth in the frequency domain, and results are similar by replacing ξ with $\xi = 4\pi N_w(\omega - \omega_0)/\omega_0$ where ω_0 is the resonant frequency.
Unless the gain does not exceed several percents, the usage of the FEL equations (B.24) is justified. Otherwise the assumption of a constant field K_r is not valid anymore. The radiation power can grow which might change the strength of the electron interaction: to cover this aspect, a self-consistent set of FEL equations must be derived as discussed in the following section.

However, it is important to estimate the limits of the resulting FEL model due to the approximations made so far. The resonant approximation (see Eq. (B.17)) has the strongest impact on the accuracy of the analytic model in this Appendix [110]: this approximation states that the electrons and the radiation field have a constant phase relation and that the interaction adds up resonantly. In order to neglect the resonant mode, which corresponds to an unphysical velocity of the electrons faster than the speed of light, the phase relation between the electrons and the radiation field must be fast oscillating for this mode.

B.3 Self-Consistent High-gain FEL Equations

The constraint of the previous section is that the gain of the radiation field must be small over the whole undulator length in order to keep the radiation amplitude $K_r \propto E_0$ constant. If the electrons get bunched, the coherent emission on the resonant wavelength is enhanced [110]. The total emitted power of coherent radiation is proportional to the square of the number of electrons: thus it is a question of the electron current whether the model of the low gain FEL is valid or not. Another point is that, for a high current beam, the electrostatic interaction of the electrons becomes significant. The FEL process is inhibited by these space charge forces because work against the electrostatic field must be done to bunch the charged electrons at a certain phase.
To include both effects in a self-consistent manner, Maxwell's equations

$$\left[\nabla^2 - \frac{\partial^2}{c^2 \partial t^2}\right] \vec{A} = -\mu_0 \vec{J} \tag{B.30}$$

$$\left[\nabla^2 - \frac{\partial^2}{c^2 \partial t^2}\right] \phi = -\frac{\rho}{\epsilon_0} \tag{B.31}$$

which can be more easily written as

$$\left[\nabla^2 - \frac{\partial^2}{c^{\partial} t^2}\right] \vec{E} = \mu_0 \frac{\partial \vec{j}}{\partial t} + \frac{\nabla \rho}{\epsilon_0} \tag{B.32}$$

have to be solved, providing the current density $\vec{J}$ as the source term for the vector potential $\vec{A}$, and the charge distribution ρ for the scalar potential ϕ, with ϵ_0 as the dielectric constant and μ_0 as the magnetic permeability [110].
The current density and charge distribution are

$$\vec{J} = ec \sum_j \vec{\beta_j}(t) \delta(\vec{r} - \vec{r_j}(t)) \text{ and } \rho = e \sum_j \delta(\vec{r} - \vec{r_j}(t)) = \frac{\vec{J}}{\vec{v}}$$

where δ is the Dirac-function and $\vec{r_j}(t)$ the trajectory of the jth electron.
Restricting our analysis of FEL theory to the 1D model, we assume a transversally large beam with uniform charge distribution ($\partial\rho/\partial z = 0$) and a wave equation driven by a transverse current density of electrons j_x oscillating along the x-direction in the undulator. Eq. (B.32) becomes

$$\left[\frac{\partial^2}{\partial z^2} - \frac{\partial^2}{c^2 \partial t^2}\right] E_x(z,t) = \mu_0 \frac{\partial j_x}{\partial t} \tag{B.33}$$

with $j_x = e\vec{v_x} n_e(z,t) = \frac{a_w}{\gamma} j_z \cos(k_w z)$ [109]. A trial solution to the wave equation is

$$E_x(z,t) = E_x(z) e^{i(kz - \omega t)} \tag{B.34}$$

where we note that the seed radiation is chosen polarized in the same direction as the electron oscillatory motion. The radiation field interacts with the complex transverse current j_x due to the electrons' velocity in x, causing the radiation amplitude to vary with z.

The next goal is the description of the rate of change of the slowly varying radiation field amplitude $E_x(z)$. Inserting the ansatz (B.34) into Eq. (B.33) gives

$$\left[-k^2 + 2ik\frac{\partial E_x}{\partial z} + \frac{\partial^2 E_x}{\partial z^2} + \frac{\omega^2}{c^2}\right] e^{i(kz-\omega t)} = \mu_0 \frac{\partial j_x}{\partial t} \tag{B.35}$$

According to the Slowly Varying Envelope Amplitude (SVEA) approximation, it is possible to neglect the second spatial derivatives of the field amplitude $|E_x''| \ll k\,|E_x'|$, therefore

$$\begin{aligned}\frac{\partial E_x}{\partial z} &= -\frac{i\mu_0}{2k}\frac{\partial j_x}{\partial t} e^{-i(kz-\omega t)} \\ &= -i\frac{\mu_0 a_w}{2k\gamma}\frac{\partial j_z}{\partial t} e^{-i(kz-\omega t)} \cos(k_w z)\end{aligned} \tag{B.36}$$

The longitudinal current density j_z has two components [35]

$$j_z = j_0 + j_1(z)e^{i\theta} \rightarrow \frac{\partial j_z}{\partial t} = -i\omega j_1(z) e^{[i(k+k_w)z-\omega t]} \tag{B.37}$$

where θ is the ponderomotive phase, also representing the electron position in the phase space.

The rate of change of the field amplitude (B.36) is proportional to the first harmonic Fourier component of the current j_1

$$\begin{aligned}\frac{\partial E_x}{\partial z} &= -\frac{\mu_0 c a_w}{2\gamma} j_1 \left[1 + e^{2ik_w z}\right] \\ &= -\frac{\mu_0 c a_w}{4\gamma_R} j_1\end{aligned} \tag{B.38}$$

where we averaged the term in the brackets out and exchanged γ with γ_R since high-gain FELs are always operated close to resonance [35, 110].

The amplitude of j_1 has to be determined from the position θ_n of the N particles. The electron longitudinal distribution is known from the solution of the pendulum equation

$$S(\theta) = e\sum_{n=1}^{N} \delta(\theta - \theta_n) \text{ with } \theta, \theta_n \in [0, 2\pi] \tag{B.39}$$

Being A_b the transversal beam area, the current density $j_z(\theta)$ is

$$j_z(\theta) = v_z n_e \sim c\frac{S(\theta)}{A_b \lambda_w} = \frac{ec}{A_b\lambda_w}\sum_{n=1}^{N}\delta(\theta - \theta_n)$$

and can be expanded in a Fourier series as

$$j_z(\theta) = \frac{c_9}{2} + \mathrm{Re}\left[\sum_{k=1}^{\infty} c_k e^{ik\theta}\right] \text{ with } c_k = \frac{1}{\pi}\int_0^{2\pi} j(\theta) e^{-ik\theta} \mathrm{d}\theta \tag{B.40}$$

Evaluating c_k for k=0,1 gives the initial DC current density and the first harmonic current [35]

$$j_0 = \frac{c_0}{2} = \frac{ecN}{A_b\lambda_w} \text{ and } j_1(\theta) = c_1 = j_0\frac{2}{N}\sum_{n=1}^{N} e^{-i\theta_n} \tag{B.41}$$

The initial DC current j_0 coincides with the electron density n_E, while the first harmonic current j_1 is proportional to the correlation of the phases of N electrons, which is called *bunching* parameter $b_n =< e^{-i\theta} >= \frac{1}{N}\sum_{n=1}^{N} e^{-i\theta_n}$. It follows the wave equation

$$\frac{\partial E_x}{\partial z} = -\frac{\mu_0 c a_w}{2\gamma_R} j_0 b_n \tag{B.42}$$

As mentioned in the previous section, the oscillatory longitudinal motion of the electrons in a planar undulator causes a reduction in the interaction strength due to the non perfect synchronization between the ponderomotive wave and the electrons [110]. We recall the kinematic coupling factor accounting for the average phase mismatch in linear undulators

$$JJ(\chi) = J_0(\chi) - J_1(\chi) \text{ where } \chi = \frac{a_w^2}{4+2a_w^2} \tag{B.43}$$

where J_0, J_1 denote the cylindrical Bessel functions of the first kind. JJ becomes less than unity at large K.
In calculations that involve the interaction strength, in order to account for this effect, we use the modified undulator parameter $\tilde{a_w} = a_w \cdot JJ$.
The wave equation (B.42) can be more easily written in terms of the dimensionless field strength [116, 117]

$$a = \frac{eJJa_wN_w\lambda_w}{\gamma_R^2 mc^2} E_x \tag{B.44}$$

as

$$\frac{\mathrm{d}}{\mathrm{d}\tau} a = -2\pi g_0 < e^{-i\theta} >_{\theta_0} \tag{B.45}$$

where $< .. >_{\theta_0}$ represents an average over the electron initial phase θ_0 and g_0 is the small signal gain coefficient [27, 119]

$$g_0 = \frac{2\pi}{\gamma^3}\frac{(\lambda_w JJa_w)^2}{\sigma_{beam}}\frac{I_p}{I_A} \tag{B.46}$$

Useful information about the effect of the "pre-bunching" of the electron beam can be inferred considering the small signal limit of Eq. (B.45), which is obtained expanding all the relevant quantities up to the first order in the amplitude a [117, 120].
Assuming an initial phase distribution [34]

$$f(\theta_0) = \sum_{n=-\infty}^{+\infty} b_n e^{i\nu\theta_0} \text{ , } b_0 = \delta(\nu-\nu_0) = 1 \text{ for a monoenergetic beam} \tag{B.47}$$

with the detuning parameter $\nu = 2\pi(\omega_0 - \omega)/\omega$ (with the same physical meaning of η in Eq. (B.23)), and thus,

$$\begin{aligned} \left\langle e^{-i\theta_0} \right\rangle &= \frac{1}{2\pi} \int_0^{2\pi} \mathrm{d}\theta_0 f(\theta_0) e^{-i\theta_0} = b_1 \ , \\ \left\langle e^{-2i\theta_0} \right\rangle &= \frac{1}{2\pi} \int_0^{2\pi} \mathrm{d}\theta_0 f(\theta_0) e^{-2i\theta_0} = b_2 \ , \end{aligned} \tag{B.48}$$

the integral equation governing the evolution of the radiation field in the small signal regime is [27,34,117,119]

$$\begin{aligned} \frac{\mathrm{d}}{\mathrm{d}\tau} a = &-2\pi g_0 b_1 e^{-i\nu_0 \tau} + i\pi g_0 \int_0^{\tau} \tau' e^{-i\nu_0 \tau'} a(\tau - \tau') \mathrm{d}\tau' \\ &+ i\pi g_0 b_2 e^{-2i\nu_0 \tau} \int_0^{\tau} \tau' e^{i\nu_0 \tau'} a^*(\tau - \tau') \mathrm{d}\tau' \end{aligned} \tag{B.49}$$

In deriving Eq. (B.49) it was assumed a long bunch condition with a single resonant mode at frequency ω, defined with respect to the resonant frequency ω_0 by the detuning $\nu_0 = 2\pi(\omega_0 - \omega)/\omega_0$, namely in the case in which slippage effects can be neglected.
Eqs. (B.42) and (B.49) constitute two equivalent ways to describe the FEL instability, which may start from an initial seed, $a(0) \neq 0$, or from a density-modulated beam, $b_1, b_2 \neq 0$, as it happens in SASE FEL amplifiers [27].

In fact, Eq. (B.49) has been shown [34] to reduce to a third order ordinary differential equation of the type

$$\dddot{a}(\tau) + 2i\nu_0 \ddot{a}(\tau) = i\pi g_0 \left[a(\tau) + b_2 a^*(\tau) e^{-2i\nu_o \tau} \right]$$

with initial conditions given by

$$a(0) = a_0 \ , \ \dot{a}(0) = -2\pi g_0 b_1 \ , \ \ddot{a}(0) = 2\pi i \nu_0 g_0 b_1$$

The possibility of a seedless operation is due to the fact that a nonzero lowest order bunching coefficient b_1 ensures initially nonvanishing first and second derivatives [119]. As shown later, it is possible to analyze independently the two situations, by integrating Eq. (B.49) with different initial conditions.

B.4 FEL Power Scaling

Collecting the different equations (B.35, B.38 and B.40), we obtain four universal coupled first-order differential equations, respectively describing the rates of change of the ponderomotive phase and of the relative energy deviation of the n^{th} electron, of the radiation field amplitude and of the j_1 current amplitude.

$$\begin{cases} \frac{\mathrm{d}\theta_n}{\mathrm{d}t} = 2ck_w\eta_n \\ \frac{\mathrm{d}\eta_n}{\mathrm{d}t} = -\frac{e}{mc\gamma_R}\mathrm{Re}\left[\left(\frac{\tilde{a_w}E_x}{2\gamma_R} - \frac{i\mu_0 c^2}{\omega}j_1\right)e^{i\theta_n}\right] \\ \frac{\mathrm{d}E_x}{\mathrm{d}z} = -\frac{\mu_0 c\tilde{a_w}}{4\gamma_R}j_1(\theta) \\ j_1(\theta) = 2j_0 b_n \end{cases} \tag{B.50}$$

These equations are the basic differential equations to describe the physics of a high gain Free-Electron Lasers, under the assumptions of a relativistic electron energy, small transverse extension compared to the undulator period length and resonant interaction between radiation field and electron beam [35, 110]. Another important assumption is that of an infinitely long electron bunch and radiation pulse: at a certain position in the undulator, an observer would not see any change in the amplitude of the radiation field or in the modulation of the electron beam in time (steady-state model).

The maximum growth rate of the field amplitude occurs when all electrons emit coherently at a certain phase. In the frame of the electron beam, this case occurs if all electrons are bunched with a periodicity of the ponderomotive wavelength which is much smaller than the electron bunch length. This kind of modulation is called *microbunching*. The performance of the FEL is at its optimum when this maximum bunching is achieved. The radiation field cannot be amplified beyond the maximum bunching [35]. A trivial solution of the FEL equations is the injection of an unbunched beam with no correlation between energy and phase and no initial radiation field ($E_0 = 0$). If an energy-phase correlation is present, the bunching factor b_n may grow.

The transverse betatron oscillation has only a weak influence on the FEL dynamics and is neglected in the 1D treatment, while stronger is the dependence on the transverse extension of the radiation field and the electron beam [110]. The main aspect here is the diffraction, where the radiation field tends to spread out transversely and thus to weaken the field amplitude and to change the phase at the center of the electron beam. Although it is important, diffraction does not change the basic working principle of a high gain Free-Electron Laser.

However, these equations are rather complex and it is difficult to analyze them analytically without any further assumptions [35].

Combining the first order equations (B.50) and after some mathematical steps, one arrives at the third order FEL equation [35, 109, 110]

$$\begin{aligned} &E_x''' + 4ik_w\eta E_x'' + (k_p^2 - 4k_w^2\eta^2)E_x' - i\Gamma^3 E_x = 0 \\ &\frac{E_x'''}{\Gamma^3} + 2i\frac{\eta}{\rho}\frac{E_x''}{\Gamma^2} + \left[\frac{k_p^2}{\Gamma^2} - \left(\frac{\eta}{\rho}\right)^2\right]\frac{E_x'}{\Gamma} - iE_x = 0 \end{aligned} \tag{B.51}$$

with the gain parameter Γ (resembling Eq. (B.46)) and the space charge parameter k_p given by

$$\Gamma = \left(\frac{\mu_0 \tilde{a}_w^2 e^2 k_w n_e}{4\gamma_R^3 m}\right)^{1/3} \quad k_p = \left(\frac{2k_w \mu_0 n_e e^2 c}{\gamma_R m \omega}\right)^{1/2} \tag{B.52}$$

and their expression in terms of the important FEL or Pierce parameter

$$\rho = \frac{1}{2\gamma}\sqrt[3]{\frac{I}{I_A}\left(\frac{JJ\lambda_w a_w}{2\pi\sigma_{beam}}\right)^2} \rightarrow \begin{cases} \Gamma = \frac{4\pi}{\lambda_w}\rho \\ k_p = \sqrt{\frac{2\lambda}{\lambda_w}}\frac{\omega_p}{c} \end{cases} \tag{B.53}$$

where $\omega_p = \sqrt{\frac{n_e e^2}{\gamma_R \epsilon_0 m}}$ is the plasma frequency in beam frame. $I = Q/(\sqrt{2\pi}\sigma_t)$ is the electron current in terms of the rms time duration σ_t and of the total bunch charge Q, σ_{beam} is the transverse dimension of the electron beam (average of its dimensions in x and y), $I_A = 17.045kA$ is the Alven current and $JJ = J_0(\chi) - J_1(\chi)$ represents the Bessel correction factor for a planar undulator of argument $\chi = \frac{1}{2}\frac{a_w^2}{1+a_w^2}$ as in (B.43).

Plasma oscillation is important in long-wavelength FELs (Raman regime), and the plasma wavenumber k_p is much smaller than the growth rate Γ in today's high-gain FELs [35]. In this approximation, we can rewrite Eq. (B.51) as

$$\frac{E_x'''}{\Gamma^3} + 2i\frac{\eta}{\rho}\frac{E_x''}{\Gamma^2} - \left(\frac{\eta}{\rho}\right)^2\frac{E_x'}{\Gamma} - iE_x = 0 \tag{B.54}$$

For a mono-energetic electron beam at resonance ($\eta = 0$) it is

$$E_x''' - i\Gamma^3 E_x = 0 \tag{B.55}$$

which is a simple third-order differential equation. There are many different ways to start the FEL process; for a general seeding configuration, we can use the trial solution

$$E_x(z) = \sum_j c_j \exp(\alpha_j z) \tag{B.56}$$

obtaining the cubic equation

$$\alpha^3 = i\Gamma^3 \tag{B.57}$$

Taking first and second derivatives of (B.48), in matrix form one has [72]

$$\begin{pmatrix} E_x(z) \\ E_x'(z) \\ E_x''(z) \end{pmatrix} = \begin{pmatrix} 1 & 1 & 1 \\ \alpha_1 & \alpha_2 & \alpha_3 \\ \alpha_1^2 & \alpha_2^2 & \alpha_3^2 \end{pmatrix} \begin{pmatrix} c_1\exp(\alpha_1 z) \\ c_2\exp(\alpha_2 z) \\ c_3\exp(\alpha_3 z) \end{pmatrix} \tag{B.58}$$

It is possible to calculate the $c's$ from the initial conditions at z=0 inverting the central matrix **A**.
The eigenvalue solutions of Eq. (B.57) are given by the three roots

$$\begin{cases} \alpha_1 = \frac{(i+\sqrt{3})}{2}\Gamma & \text{Growing mode} \\ \alpha_2 = \frac{(i-\sqrt{3})}{2}\Gamma & \text{Decaying mode} \\ \alpha_3 = -i\Gamma & \text{Oscillatory mode} \end{cases} \tag{B.59}$$

Inserting the values into $\mathbf{A}$ matrix, its inverse is

$$\mathbf{A}^{-1} = \frac{1}{3}\begin{pmatrix} 1 & (\sqrt{3}-i)/2\Gamma & (-i\sqrt{3}+1)/(2\Gamma^2) \\ 1 & (-i-\sqrt{3})/2\Gamma & (1+i\sqrt{3})/(2\Gamma^2) \\ 1 & i/\Gamma & -1/\Gamma^2 \end{pmatrix} \tag{B.60}$$

B.4.1 External seed

From a theoretical point of view, the simplest case is that of seeding the FEL with a linearly polarized electromagnetic radiation along x. If the beam is not pre-bunched, the instability is initiated by an input seed of dimensionless amplitude a_0, thus

$$E_x(0) = E_{seed} \tag{B.61}$$

Therefore,

$$\begin{pmatrix} c_1 \\ c_2 \\ c_3 \end{pmatrix} = \mathbf{A}^{-1}\begin{pmatrix} E_{seed} \\ 0 \\ 0 \end{pmatrix}$$

giving the coefficients $c_1 = c_2 = c_3 = \frac{1}{3}E_{seed}$. The electric field evolution is described by

$$E_x(z) = \frac{E_{seed}}{3}\sum_i e^{\alpha_i z} \tag{B.62}$$

The solution is the superposition of three terms, with one exponential, having real positive argument, leading to exponential growth

$$\begin{aligned} E_x &\approx \frac{E_{seed}}{3}e^{\frac{\sqrt{3}\Gamma z}{2}} = \frac{E_{seed}}{3}e^{z/2L_g} \\ P_{exp}(z) = |E_x(z)|^2 &\approx \frac{|E_{in}|^2}{9}e^{\sqrt{3}\Gamma z} = \frac{|E_{in}|^2}{9}e^{z/L_g} \end{aligned} \tag{B.63}$$

where the last equality introduces the gain length (equal to the dimensionless folding length)

$$L_g = \frac{1}{\sqrt{3}\Gamma} = \frac{\lambda_w}{4\pi\sqrt{3}\rho} = \sqrt{3}(\pi g_0)^{1/3} \tag{B.64}$$

This is the phenomenon of a collective instability [35, 110]. The observed power $P = |E_x|^2$ is fluctuating due to the interference of the three modes. Despite the interference, the absolute power of the radiation field and the maximum gain of the FEL is limited to the order of the initial seeding field. At first in the so-called *lethargy region* (see Figure B.6), the three modes compete with one another and the driving mechanism is the interference defining the 'start-up' regime (the sum grows slowly with z). After a certain distance the growing mode dominates and causes exponential amplification of the initial radiation since $\mathrm{Re}[\alpha_1] > 0$ ("exponential regime").

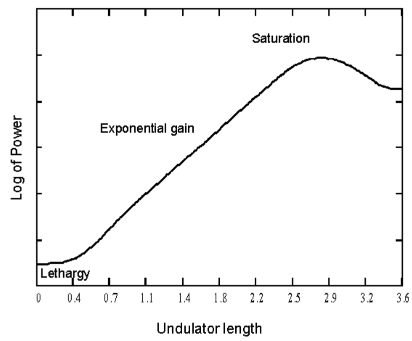

Figure B.6: Power growth in an high-gain FEL, from [35]

Start-up and exponential growth are combined to the FEL "linear regime" because the differential equations used only linear terms. For growing radiation amplitudes, numerical simulations show that the exponential regime ends up in the "saturation regime", where the radiation field amplitude is limited [35, 110].
This result seems to be in contradiction with the results of a low gain FEL, where at resonance no energy gain is visible (see Figure B.3): the explanation of this difference is that the low gain FEL remains in the start-up regime.

Eq. (B.63) holds for $z \geq 3L_g$. After about $L_{sat} \approx 20L_g$ the amplification process reaches saturation, with a final FEL power of the order of [27, 121]

$$P_{fin} \sim 1.6\rho P_{beam} \tag{B.65}$$

where $P_{beam} = mc^2\gamma I_p/e$ is the peak power carried by the electron beam. The power growth in the FEL amplifier starting from an input signal of power P_0 is described by the logistic function (similarly to Eq. (B.63) but taking into account the final power in Eq. (B.65), valid in the 1D "cold" beam limit) [27]

$$P(z) = \frac{P_0}{9} \frac{\exp(z/L_g)}{1 + \frac{P_0}{9P_fin}\exp(z/L_g)} \tag{B.66}$$

Figure B.7 (see next page) highlights the transition between linear and non linear regime of the 1D FEL. For small initial radiation fields and a nearly unbunched beam, the start-up of the amplification and the exponential growth of the radiation can be described by the FEL equations in the linear regime. The limit of the linear model towards large amplitudes is given by the bunching factor $b_n =< exp(-i\theta) >$, which cannot exceed unity ($b_{max} \sim 0.8$). The exponential growth is significantly reduced if the radiation field comes close to this limit and one enters the non-linear regime. In addition to start-up and exponential growth of the radiation field, the reduction of the FEL amplification process is observed in the saturation regime. The radiation field evolution in this regime can only be calculated by numerical simulation, and the maximum gain is several orders of magnitude larger than for the low gain FEL [110].

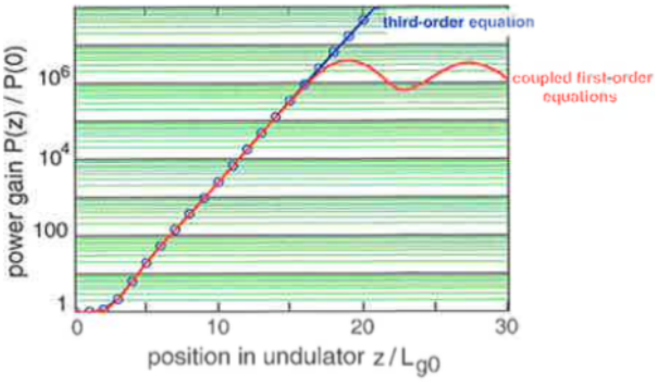

Figure B.7: Comparison of results of 1^{st} and 3^{rd} order equations, from [35]

Using the definition of the dimensionless field (B.44), the linear model agrees well up to a field amplitude of $|a| \approx 0.3$ with the numerical simulation (for $z < 2L_g$), and the growth rate of further amplification is reduced till the radiation field reaches a maximum amplitude of $a \approx 1.2$ [110].

As shown in Figure B.7, the coupled first-order equations give accurate estimates and predict the power saturation regime, while the third-order equation cannot predict it: this is due to the fact that, contrarily to what happens at saturation, a small bunching was assumed for its derivation.
After reaching the maximum amplification in the beginning of the saturation regime (in a length $L_{sat} \approx 20L_g$), no further amplification is visible, the electrons begin to absorb FEL radiation but the electrons' phase space becomes chaotic so the FEL power is not reduced and oscillates about an average non-zero value. The period length is about five gain lengths and the maximum growth and decay rate is comparable to the exponential regime [35, 110].
It is not useful to extend an undulator beyond the saturation point if the FEL is seeded by an external radiation field, unless the undulator parameters (a_w and λ_w) are matched to compensate the energy loss of the electron beam.

Typical phase space distributions of the electron beam are shown in Figure B.8 (see next page) for different positions in the undulator. The initial distribution (upper left) gets deformed in the linear regime (upper right) until most of the electrons are nearly vertically placed at saturation. Beyond saturation the distribution gets wound up (lower left). Electrons, which are located close to the separatrix of the ponderomotive wave bucket, are detrapped when the radiation field amplitude starts to oscillate (lower right) [110].

The energy conservation, written in terms of the scaled radiation field,

$$|a|^2 + \left\langle \frac{\gamma}{\rho\gamma_R} \right\rangle = const \tag{B.67}$$

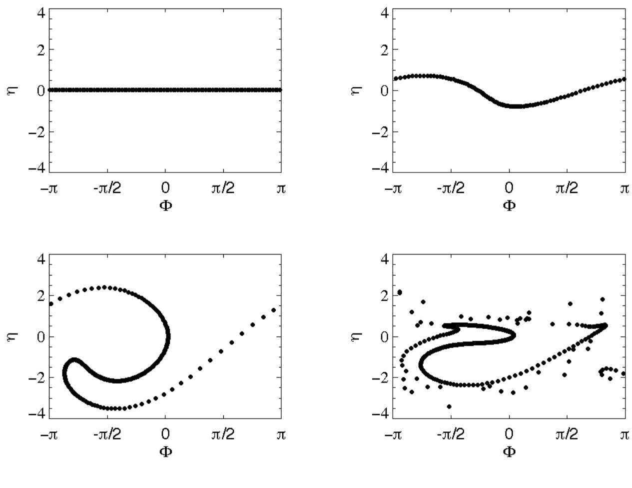

Figure B.8: Longitudinal phase space distribution of the electron beam at different times, from . Here the ponderomotive phase $\theta = \Phi$, from [110]

directly derived from the equation of motions, determines the efficiency of the FEL at saturation ($|a| \approx 1$) [110]

$$\text{Efficiency} = \frac{\Delta\gamma}{\gamma_R} \sim \rho \tag{B.68}$$

The FEL parameter is a measure of the energy conversion efficiency, approximately the fraction of beam power converted into photons at saturation according to Eq. (3.65). Its numerical value is tipically in the order of 10^{-3}.
The FEL parameter also gives an estimate of the natural bandwidth of the FEL

$$bw = \Delta\lambda/\lambda \approx \rho \tag{B.69}$$

The resonance approximation (B.17) yields the constraint

$$\rho \ll 1 \tag{B.70}$$

The FEL parameter ρ can be as well regarded as the error of the accuracy due to the resonance approximation.

B.4.2 Pre-bunched beam

Another seeding option uses a pre-bunched electron beam. To calculate the initial conditions we recall Eq. (B.38) at z=0 from the one-dimensional theory

$$\frac{\mathrm{d}E_x(0)}{\mathrm{d}z} = -\frac{\mu_0 c a_w}{4\gamma_R} j_1(0) \to \frac{\mathrm{d}^2 E_x(0)}{\mathrm{d}z^2} = -\frac{\mu_0 c J J a_w}{4\gamma_R}\frac{\mathrm{d}j_1(0)}{\mathrm{d}z} \tag{B.71}$$

With $j_1(0)$ given by Eq. (B.41), it is

$$\frac{\mathrm{d}j_1(0)}{\mathrm{d}z} = j_0 \frac{-2i}{N}\sum_{n=1}^{N} \frac{\mathrm{d}\theta_n(0)}{\mathrm{d}z}\exp(-i\theta_n(z)) \text{ with } \frac{\mathrm{d}\theta_n(0)}{\mathrm{d}z} = 2k_w\eta$$

where we considered monoenergetic electrons ($\eta_n = \eta$). We obtain

$$\begin{pmatrix} E_x(0) \\ E_x'(0) \\ E_x''(0) \end{pmatrix} = \frac{\mu_0 c J J a_w}{4\gamma_R} j_1(0) \begin{pmatrix} 0 \\ -1 \\ 2ik_w\eta \end{pmatrix} \tag{B.72}$$

with the starting coefficients given by

$$\begin{pmatrix} c_1 \\ c_2 \\ c_3 \end{pmatrix} = \frac{\mu_0 c J J a_w j_1(0)}{4\gamma_R} \mathbf{A}^{-1} \begin{pmatrix} 0 \\ -1 \\ 2ik_w\eta \end{pmatrix} \tag{B.73}$$

where $\mathbf{A}^{-1}$ is that of Eq. (B.51). Starting from a pre-bunched beam, $b_1 \neq 0$, we may neglect the second and third terms of Eq. (B.49), obtaining the coherent spontaneous emitted field [27, 34]

$$a(\tau) = -2\pi g_0 b_1 \frac{1 - e^{-i\nu_0\tau}}{\nu_0} \tag{B.74}$$

which is the main difference with respect to the seeded case. Assuming the system to be tuned at the resonance ($\nu_0 = 0$), the power evolves as

$$P_{coh}(z) = \frac{1}{3}\rho |b_1|^2 P_{beam} \left(\frac{z}{L_g}\right)^2 \tag{B.75}$$

It is evident that, in absence of an external seed, the natural evolution of the instability is a quadratic growth, according to Eq. (B.75) in the first part. When the seed strength becomes larger than the bunching source term, the FEL enters the exponential gain regime. In the second, the evolution is thus obtained calculating the exponentially growing eigenvalue of Eq. (B.72) [27]

$$c_1 = \frac{\mu_0 J J c a_w j_1(0)}{12\gamma_R} \left[\frac{-(\sqrt{3} - i)}{2\Gamma} + (2ik_w\eta) \frac{1 - i\sqrt{3}}{2\Gamma^2} \right]$$

At z increasing, the exponential regime for an FEL with a pre-bunched electron beam is expressed by

$$|E_x(z)| \approx \frac{\mu_0 c J J a_w |J_1(0)|}{12\gamma_R \Gamma} \exp\left[\frac{\sqrt{3}\Gamma z}{2}\right] \tag{B.76}$$

to be compared with Eq. (B.63). The seeding strength that gives equivalent strength to a pre-bunched FEL is [72]

$$E_{equiv} = \frac{\mu_0 c J J a_w |j_1|}{4\gamma_R \Gamma} \tag{B.77}$$

In terms of the formalism used in Eq. (B.49), the transition between the two regimes happens when the pre-bunching source gets smaller than the self-induced field growth [**?**, 27]

$$\left| -2\pi g_0 b_1 e^{-i\nu_0\tau} \right| < \left| i\pi g_0 \int_0^\tau \tau' e^{-i\nu_0\tau'} a(\tau - \tau') \mathrm{d}\tau' \right| \tag{B.78}$$

Inserting Eq. (B.75) in (B.78), the threshold value of the coordinate along the undulator is $z_{th} = \sqrt{3}L_g$. At the transition, where the functional behaviour of the solution changes from quadratic to exponential, the power depends on the electron beam modulation at the undulator entrance

$$P_{th} = \rho|b_1|^2 P_{beam} \simeq 0.8 P_{fin}|b_1|^2 \tag{B.79}$$

Superimposing the functions (B.75) and (B.66), it is possible to write a function describing the power growth in the FEL amplifier starting from a pre-bunched beam with bunching factor b_1 [27]

$$P(z) = P_{th}\left[\frac{\frac{1}{3}\left(\frac{z}{L_g}\right)^2}{1+\frac{1}{3}\left(\frac{z}{L_g}\right)^2} + \frac{\frac{1}{2}\exp\left[\frac{z}{L_g}-\sqrt{3}\right]}{1+\frac{P_{th}}{2P^*_{fin}}\exp\left[\frac{z}{L_g}-\sqrt{3}\right]}\right] \tag{B.80}$$

with $P^*_{fin} = P_{fin} - P_{th}$.

B.4.3 SASE

In a SASE FEL, the source term triggering the exponential power growth is proportional to the harmonic current of the beam current in the amplification bandwidth, which is given by the Fourier coefficient $b_1 = \langle\exp(-i\theta_0)\rangle$ (see Eq. (B.48)), where for any integer n, we define b_n as [27]

$$b_n = \frac{1}{\lambda}\int_0^\lambda \rho_e(\theta)e^{-i2\pi n\theta/\lambda}\mathrm{d}\theta \tag{B.81}$$

In the previous expression, θ is the longitudinal coordinate along the electron bunch, and $\rho_e(\theta)$ the normalized electron beam longitudinal current density, with λ the resonant wavelength.

A SASE FEL is seeded from the random noise that comes from the discrete nature of the electrons. The seed signal can either be thought of as broadband electron bunching or as broadband synchrotron radiation. The FEL amplifies a narrowband portion of the signal, which is a complicated function of the distance along the undulator [72].
Discreteness of electrons leads to random fluctuations in current, which by Fourier Transform show frequency dependent random bunching.

$$\tilde{I}(t) = i(\omega) = \int_{-T/2}^{T/2} I(t)e^{i\omega t}\mathrm{d}t$$

The total power in the signal can be written as

$$P = \frac{1}{2\pi T}\int_{-\infty}^{\infty}|i(\omega)|^2\mathrm{d}\omega = \frac{1}{\pi T}\int_0^\infty |i(\omega)|^2\mathrm{d}\omega$$

from which we define the average amount of AC current within the frequency range $[\omega, \omega + d\omega]$

$$S(\omega) = \frac{1}{\pi} \left\langle |i(\omega)|^2 \right\rangle$$

In a SASE FEL the AC current is represented by the shot noise due to the discrete locations of electrons. In this case, the current can be described by a sum of Dirac delta functions

$$I(t) = e \sum_{j=1}^{N} \delta(t - t_j) \rightarrow i(\omega) = e \sum_{j=1}^{N} ei\omega t_j$$

so that the spectral density function becomes

$$\begin{aligned} S(\omega) &= \frac{e^2}{\pi T} \left\langle \sum_{j=1}^{N} \exp(i\omega t_j - i\omega t_j) + \sum_{j=1}^{N} \sum_{k \neq j}^{N} \exp[i\omega(t_j - t_k] \right\rangle \\ &= \frac{e^2 N}{\pi T} = \frac{eI_0}{\pi} \end{aligned}$$

The initial SASE current is determined by calculating the total AC current from random noise in the FEL bandwidth $\Delta\omega$

$$I_{rms}^2 = S(\omega)\Delta\omega = \frac{eI_0}{\pi}\Delta\omega \rightarrow |j_1| = \frac{\sqrt{I_{rms}^2}}{A_b} = \frac{1}{A_b}\sqrt{\frac{eI_0}{\Delta\omega}} \tag{B.82}$$

The randomness of the initial bunching is reflected in the amplified FEL power (see the results regarding SASE operation in Chapter 4).

B.5 3D effects

So far in this Appendix only the model of the one dimensional FEL has been discussed, without considering the transverse motion of the electrons nor the limited size of the radiation field. This section presents the basic limits due to the beam parameters that were not considered above.

The resonance condition (B.19) depends on the transverse position via the undulator parameter: a dispersion in angle and transverse position, as well as a dispersion in the beam energy, causes a dispersion in the emitted wavelength. Another factor affecting the FEL gain is associated to the natural diffraction of the radiation field, which sets a lower limit to the optical mode's transverse size. Including all these factors, there is a reduction of the gain, a growth of the gain length, and a reduction of the final output power.

These effects have been extensively studied [35, 110, 121]. First, space charge acts as a counterforce against bunching, and cam be assumed negligible if $k_p \ll \Gamma$ (see Eq. (B.43)).
Another effect is that of optical diffraction. The rms radius of a focused electron

beam is determined by its normalized emittance $\epsilon_n = \gamma\epsilon_x$ (with the geometric emittance $\epsilon_g = \epsilon_x$) and the average β function of the focusing optics [35]

$$\bar{\beta} = \frac{\sigma_{beam}^2}{\epsilon_g} \tag{B.83}$$

With $j = 1, .., N$ the index representing the single electrons in the beam, one has

$$\begin{aligned} \sigma_x^2 = \langle x^2 \rangle = \frac{1}{N}\sum_j x_j^2 &\rightarrow \text{ Beam rms size} \\ \sigma_{\dot{x}}^2 = \langle \dot{x}^2 \rangle = \frac{1}{N}\sum_j \dot{x}_j^2 &\rightarrow \text{ Beam rms divergence} \\ \langle x\dot{x} \rangle = \frac{1}{N}\sum_j x_j \dot{x}_j &\rightarrow \text{ Correlation coefficient} \end{aligned} \tag{B.84}$$

and the same for y. The beam rms emittance is defined as

$$\epsilon_x = \sqrt{\langle x^2 \rangle \langle \dot{x}^2 \rangle - \langle x\dot{x} \rangle^2} \tag{B.85}$$

and it is not a constant of motion in case of accelerated beams, so that one tipically introduces the normalized emittance

$$\epsilon_{n,x} = \beta\gamma\epsilon_x \approx \gamma\epsilon_x \tag{B.86}$$

Optical diffraction is measured by the radiation Rayleigh length z_R, which is given by the square of the electron beam's rms radius in the undulator divided by the photon beam's emittance $\lambda/4\pi$

$$z_R = \frac{4\pi\sigma_{beam}^2}{\lambda} \tag{B.87}$$

In order to neglect diffraction 3D effecs, the gain length must be shorter than the Rayleigh length

$$L_g \leq z_R \tag{B.88}$$

Betatron motion slows down the electrons and adds spread in v_z, thus leading to a violation of the resonance condition. For emittance 3D effects to be small, the electron beam's geometric emittance must be smaller than the photon beam emittance

$$\epsilon_g < \frac{\bar{\beta}}{2\sqrt{2}\gamma_R^2}\rho \rightarrow \epsilon_n \leq \frac{\gamma\lambda}{4\pi} \tag{B.89}$$

There exists another constraint on the electron beam's energy spread, because particles far from resonance condition have low gain. Electrons must maintain the same axial velocity during the coherence length $l_c = N_c\lambda$, where $N_c = 1/4\pi\rho$ is the number of wavelengths in a coherence length (equal to $\sqrt{3}$ times the number of periods in one gain length) [121].

In order to neglect 3D effects due to energy spread, the relative rms energy spread must be less than ρ

$$\frac{\sigma_\gamma}{\gamma} \leq \rho \sim \frac{1}{4\pi N_c} \tag{B.90}$$

The Ming Xie relations are widely used in the design of FEL amplifiers [35, 121], where three parameters account for diffraction effects, emittance (beam divergence) effects, and energy spread related effects

$$\begin{cases} L_{g,1d} \leq z_R & \text{Diffraction} \rightarrow X_d = \frac{L_{g,1d}}{z_R} \\ \epsilon_g \leq \frac{\lambda}{4\pi} & \text{Emittance} \rightarrow X_\epsilon = \frac{L_{g,1d}}{\beta}\frac{4\pi\epsilon_g}{\lambda} \\ \frac{\sigma_\gamma}{\gamma} \leq \frac{1}{4\pi N_c} & \text{Energy spread} \rightarrow X_\gamma = \frac{4\pi L_{g,1d}}{\lambda_w}\frac{\sigma_\gamma}{\gamma} \end{cases} \tag{B.91}$$

Ming Xie parameters should be less than 1 to minimize 3D effects. The gain deterioration due to non ideal electron beam qualities can be described by introducing a three dimensional gain length $L_{g,3d}$ [121]. $L_{g,3d}$ cannot be studied with the 1D FEL theory but relies on fits to simulations

$$L_{g,3d} = (1 + \Delta) L_{g,1d} \tag{B.92}$$

where $\Delta = 1 + a_1 X_d^{a_2} + a_3 X_\epsilon^{a_4} + a_5 X_\gamma^{a_6} + a_7 X_\epsilon^{a_8} X_\gamma^{a_9} + a_{10} X_d^{a_{11}} X_\gamma^{a_{12}} + a_{13} X_d^{a_{14}} X_\epsilon^{a_{15}} + a_{16} X_d^{a_{17}} X_\epsilon^{a_{18}} X_\gamma^{a_{19}}$ with a_{ij} fitted coefficients, which are not reported here.

Appendix C

GENESIS 1.3

The FEL simulations, whose results are reported and discussed in Chapter 4, have been carried out with the three dimensional code GENESIS 1.3 in the time dependent mode, based on the self-consistent FEL equations in Appendix B.3 with no further approximations or assumptions. The code was written by Sven Reiche as a part of the Ph.D. thesis at DESY [110], Germany, and then further extended at UCLA and DESY.
It bears its origin in the steady-state 2D code TDA3D, although they only share some naming convention and the memory efficient 4th order Runge-Kutta integration of the macro particle differential equations. GENESIS 1.3 is focused to simulate single-pass free-electron lasers, both FEL amplifier and SASE FEL, although the flexible input can be used to easily extend the capacity of GENESIS 1.3 to cover FEL oscillators or multistage set-ups [110, 122].

It is an unvaluable tool to simulate an FEL performance or to compare theoretical and experimental results.
Any FEL code has to solve four major problems [110]:

- Generating the initial phase space distribution of the electron beam,
- Solving ordinary differential equations of the electron beam variables,
- Solving partial differential equations of the radiation and electrostatic field,
- Bookkeeping of the radiation field and electron beam parameters and efficient use of the computer resources for time-dependent simulations.

If the simulation runs under certain assumptions, some of these problems may not occur. For instance, for one dimensional steady-state FEL simulations, operating in the linear regime, only the second problem remains, namely to solve an ordinary third order differential equation.
The next sections will show some important parameters of the code.

C.1 The Particle Equations

Macro particles represent the electron beam in all dimension of the 6D phase space. For convenience, the longitudinal position is replaced by the ponderomotive phase $\theta = (k + k_w)z - kct$ of the particle (as already assumed in sections B.2 and B.3) and the transverse momenta are normalized to mc. The independent variable is the longitudinal position z within the undulator, and the equations of motion for the longitudinal and transverse space are

$$
\begin{aligned}
\frac{\mathrm{d}\theta}{\mathrm{d}z} &= k\left(1 - \frac{1}{\beta_z}\right) + k_w, \\
\frac{\mathrm{d}\gamma}{\mathrm{d}z} &= -\frac{k f_c a_r a_w}{\beta_z \gamma} \sin(\theta + \Phi) - E_z \\
\frac{\mathrm{d}x}{\mathrm{d}z} &= \frac{p_x}{\beta_z \gamma} \\
\frac{\mathrm{d}p_x}{\mathrm{d}z} &= -q_x x + b_x + \frac{s}{\gamma} p_y \\
\frac{\mathrm{d}y}{\mathrm{d}z} &= \frac{p_y}{\beta_z \gamma} \\
\frac{\mathrm{d}p_y}{\mathrm{d}z} &= -q_y y + b_y - \frac{s}{\gamma} p_x
\end{aligned}
$$

where β_z is the electron velocity in z normalized to the speed of light, k and k_w the radiation and undulator wave number, f_c the coupling factor (=JJ for a planar undulator), a_r and a_w are the scalar normalized amplitudes of the radiation and undulator field, Φ is the phase of the radiation field, E_z is the electrostatic field, b_x and b_y are the normalized dipole strengths in x and y, q_x and q_y are the quadrupole field strengths in x and y and s is the solenoid field strength.

The differential equations for energy and phase are solved by a 4th order Runge-Kutta solver, where the field amplitude of the discretized radiation field and electrostatic field is interpolated to the particle position. Distinct to the main undulator field a_w, the quadrupole and dipole fields combine many field sources such as the natural focusing of the undulator, strong focusing quadrupoles, undulator field errors and corrector magnets (steering magnets. Per integration step their strength is fixed and the differential equations for the transverse motion is solved analytically.

C.2 The Field Equations

Electro-static and electro-magnetic fields are discretized within GENESIS 1.3. The radiation field is described in the paraxial approximation, where the field is separated into a dominant, fast oscillating term and an amplitude, which slowly varies in magnitude and phase. The partial differential equation

$$\left[\triangle_\perp + 2ik\frac{\partial}{\partial z}\right] u = i\frac{e^2\mu_0}{m}\sum_j \delta(r - r_j)\frac{f_c a_w}{\gamma_j} e^{-i\theta_j}$$

is of parabolic type, where $u = -ia_r \exp(i\Phi)$ is the complex representation of the radiation field. Note that there is no explicit dependence on t in the differential equation. Time-dependence effects are discussed below. The transverse profile of the field is discretized on a Cartesian grid with uniform spacing.
Only the longitudinal component of the electro-static field is taken into account within GENESIS 1.3, because it acts as a repulsive force during the formation of the micro-bunching. On the scope of a single radiation wavelength, the field can be assumed to be periodic in the ponderomotive phase of the electrons. In the Fourier series expansion of the longitudinal field the partial different equation of the l coefficient is

$$\left[\triangle_\perp + \frac{l^2k^2(1 + a_w^2)}{\gamma_R^2}\right] E_{z,l} = i\frac{ec^2\mu_0 lk(1 + a_w^2)}{\gamma_R^2}\sum_j \delta(r - r_j)\frac{f_c a_w}{\gamma_j} e^{-i\theta_j}$$

where the resonant energy is defined as (B.20). With a radial grid centered to the electron beam centroid position and the azimuthal decomposition of the Fourier coefficients, the matrix representation of the partial differential equation is reduced to a tridiagonal matrix, where a fast and memory-efficient solver is applied to. Long-term electro-static fields (e.g. wake fields) must be calculated externally. They can be imported into GENESIS 1.3 and applied to equations of motion for the macro particles.

C.3 Time-Dependent Effects

GENESIS 1.3 supports two modes of calculations: steady-state and time-dependent simulations. Steady-state simulations are based on the assumption of an infinite long electron bunch and radiation field with no longitudinal variation of any parameter. The partial derivative with respect to the time drops out of the field equations resulting in the parabolic equation shown above. The longitudinal description can be reduced to a single wavelength (bucket) with periodic boundary condition in the ponderomotive phase of the macro particles.

In the time-dependent mode, it has to keep the entire radiation field and electron bunch at whole in memory, which easily exceeds the capability of todays best single processor machines. GENESIS 1.3 discretizes the radiation field and electron beam in t, with the minimum temporal interval which is called *slice*. Information on the local electron distribution is carried by the radiation field only in the forward direction (slippage): thus, time-dependent simulations roll over the electron bunch starting from the back (see Figure C.1).

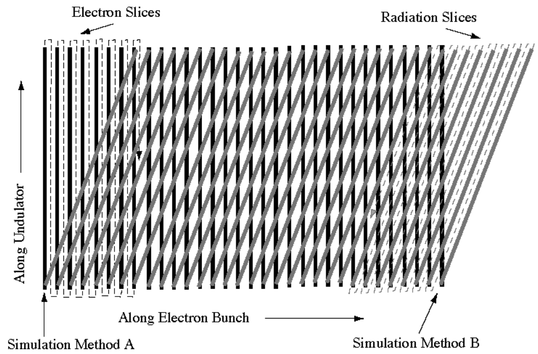

Figure C.1: Schematic order for time-dependent simulations. Due to the slippage the radiation field slices (tilted grey bars) propagate in the forward direction with respect to the electron beam slices (black bars). The integration can either be performed by starting from the end of the bunch and keeping one electron beam slice in memory or from the bunch head with a radiation slice in memory (Method A and B, respectively), from [110]

Advancing, the radiation field is split into two parts: solving the steady-state field equation and copying the field to the next slice. By so doing, only a single slice of an electron beam and the radiation field over the total slippage length, which can be significantly shorter than the bunch length, needs to be kept in memory. Although the spacing of the slices can freely be chosen with GENESIS 1.3, some conditions have to be fulfilled for a valid time-dependent simulation.

The propagation of the radiation field has to be done frequently to avoid collective instabilities of the steady-state field solver per integration step within a single slice. Therefore the integration step size has to be much smaller than the typical FEL gain length

$$\Delta z \ll \frac{1}{2k_w\rho}$$

where ρ is given by Eq. (2.2). Similar arguments are valid for the separation t of the slices, which is related to the integration step size by the inequity $c\Delta t \gg (k_w/k)\Delta z$. The constraint for the t-discretization is therefore

$$\Delta t \ll \frac{1}{2ck\rho}$$

It thus follows that time for simulations with shorter wavelengths to finish is longer. On the other hand each slice has a thickness of one radiation wavelength. The time discretization must be $c\Delta t \gg \lambda$ to avoid overlapping slices. Conflicts might arise if ρ approaches unity. Anyhow in this case, the entire FEL model, on which GENESIS 1.3 is based, is not valid anymore and other simulation tools need to be used to solve this problem.

Very often the time-window ΔT, which is spawn by all slices, covers only a subsection of the electron beam. Because GENESIS 1.3 does not know anything about the field, which slips through the back of the time-window, it suppresses the output over the first slippage length. To obtain valid output, the time window must be at least as long as the slippage length ΔT_s, yielding the constraint

$$\Delta T \geq \Delta T_s = \frac{k_w}{k}\frac{L_w}{c}$$

where L_w is the length of the undulator. In practice the time-window should be significantly larger than the limit given above to allow a frequency analysis of the radiation. As already said in Section , the typical width of the FEL spectrum is ρ. To resolve the spectrum, the time-window must fulfill the more stringent constraint

$$\Delta T \gg \frac{\lambda}{c\rho} + \Delta T_s$$

Once GENESIS 1.3 has allocated enough memory to hold the radiation field over one slippage length, there is no computational limitation imposed on the maximum size of the time-window.

C.4 Simulation Input Parameters and Files

The user has the option to generate the initial distribution of the radiation field and macro particles as well as the magnetic field of the undulator internally, or to supply the explicit description of these parameters by additional input files. This feature can easily be extended to an interface to codes tracking the electron beam through the linear accelerator to the entrance of the undulator [122]. In addition complicated undulator designs such as an arbitrary tapering of the undulator field or non-periodic focusing structures can be covered.

In total, GENESIS 1.3 depends on up to 14 files including such files containing the magnetic field or a sample phase space distribution of the electron beam. For all runs, the main input file, containing the vast majority of the information needed to run the simulation, is mandatory. Besides the main output file, which is always created, the main input file defines whether additional input and output files are read or written. All output files, except for the magnetic output file, uses the filename of the main output file as the root for their filenames and appends a three letter filename extension. Input files can have independent filenames, which are defined in the main input.

The main input file of GENESIS 1.3 is controlled by roughly 100 parameters, regarding the undulator and quadrupoles magnetic field, the main features of the electron beam and few initial conditions of the radiation field. Some of them become obsolete if additional input files are used, and if not included in the input file they fall back on their default values.

In this section the main parameters are listed and Figure C.2 shows the basic flow chart.

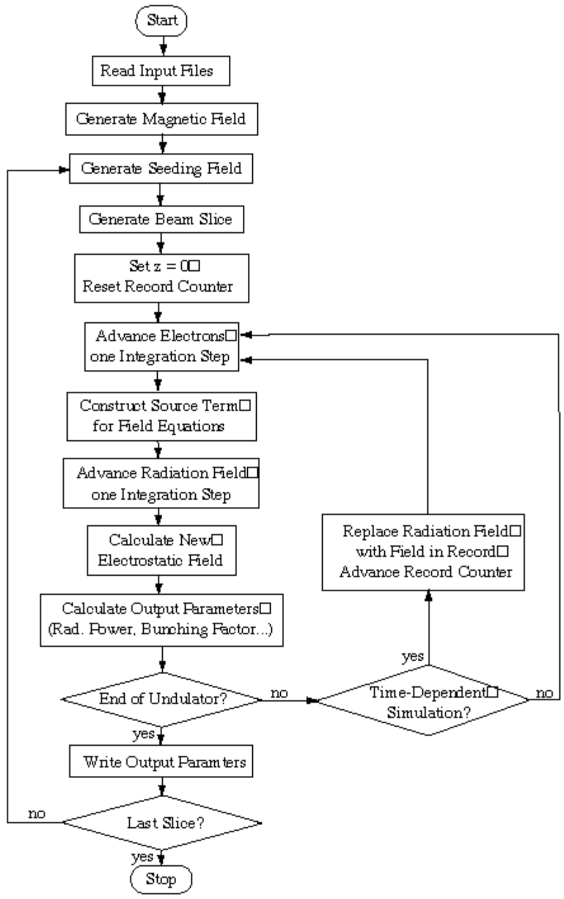

Figure C.2: Basic flow chart of GENESIS 1.3, from [110]

C.4.1 Magnetic Field

Length and strength of both the undulator modules and the quadrupoles are specified in an external file. The length is given in measure of the undulator period length λ_w, specified by the parameter XLAMD in the main input file. The intensity of the undulator field is given by the parameter AW (AWO in the main input file), repressing the normalized, dimensionless rms undulator parameter

$$AW = \frac{eB}{mck_w}$$

with $B = B_p/2$ for a planar undulator and $B = B_p$ for a helical undulator, where B_p is the on-axis peak field, while the parameter QF represents the quadrupoles' gradient q=dB/dz.

In the main input file, it is possible to specify the type of undulator through the flag IWITYP (=0 for a planar undulator, $\neq 0$ for an helical undulator). The parameters XKX and XKY permit to take the normalized natural focusing of the undulator in the transverse directions into account, and the fundamental relation between them is given by

$$XKX + XKY = 1$$

Common values are XKX=0, XKY=1 for a planar undulator or XKX=XKY =0.5 for a helical undulator, but might vary if focusing by curved pole faces is simulated.

C.4.2 Electron Beam

The electron beam is represented by macro particles and the radiation field is discretized on a Cartesian mesh. The electrostatic field is evaluated on a secondary, radial mesh, centered on the electron beam. If an external PARTFILE or DISTFILE specifying the whole phase space distribution of the electron beam is not given. the electron parameters have to be specified by means of few parameters within the main input file.

The electron beam is first defined by the number of macroparticles per slice (NPART, which should be at least 2048 and higher for simulations of wavelengths below 10nm to exclude numerical noise), its average energy and energy spread (GAMMA0 and DELGAM) and its rrms normalized emittances (EMITX and EMITY). A good value for the rms transverse beam size (RXBEAM and RYBEAM) and the Twiss parameters ALPHAX, ALPHAY are critical for a good performance. Moreover, GENESIS1.3 does not support matching, so that these values have to be found by means of external programs. However, in case the FODO lattice starts with half a quadrupole or the field strength of all quadrupoles is set to zero, than the beam goes through a waist at the undulator entrance for best matching (ALPHAX, ALPHAY=0) and the code allows for an iterative method to find the right values for the beam size while ignoring the radiation results [122].

In order to load the particles' phase, energetic and phase space distributions, GENESIS1.3 uses the Hammersely sequences, which indicate an ordered set of n points within a unitary square

$$p_i = (x_i, y_i) = \left[\frac{1}{i}, \Phi_2(i)\right]$$

where $\Phi_2(i)$ is the reflection of the binary representation of i around the decimal point. As an example, for i=3 one obtains

$$x_3 = 1/3 = 0.33 \rightarrow i = 3 = 11_2 \Rightarrow y_3 = .11_2 = \frac{1}{2} + \frac{1}{4} = 0.75$$

The ITGAUS parameter allows to define the transverse distribution profile of the particles, while the ISEED parameter is the seed for the random numbers generator to initialize the phase fluctuations (this parameter is changed to analyze a sequence of uncorrelated pulses). Finally, NBINS (≥ 4) is the number of subsets of the particles' phase.

C.4.3 Radiation

In FEL amplifiers and SASE FELs, the radiation parameters tipically need to be optimized. A SASE simulation significantly reduces the impact of the waist position ZWAIST and the Rayleigh length ZRAYL parameters, but it is recommended as a pre-optimization step to run steady-state simulation (ITDP=0).
A good estimate of the radiation wavelength is given by the resonant formula (2.1), with λ=XLAMDS, γ=GAMMA0, λ_w=XLAMD and a_w=AW0, even if diffraction and emittance effects (considered in section B.5) might slightly change the resonant wavelength.
The Rayleigh length z_r should be chosen so that the initial beam size is similar to the one of gain-guided radiation field in the exponential amplification regime. If the radiation waist is at the undulator entrance (ZWAIST=0), the initial beam size is simply given by $\sqrt{z_r\lambda/\pi}$ with z_r=ZRAYL. The input radiation power is set by the parameter PRAD0 for an FEL amplifier, while it is zero for a SASE FEL. The input power is proportional to the FEL parameter ρ, dependent on the coupling coefficient f_c (FBESSO), σ_b=(RXBEAM+RYBEAM)/2, I_p=CURPEAK.
If the results of a steady-state simulation are satisfying, the input deck can be used for more advanced simulations (field errors, time-dependent simulations). Otherwise, further optimization of the input parameters is needed. In order to estimate the accuracy of a simulated result, special runs have to be performed to check the results against either the theoretical analysis, other existing codes or experimental results.

Some parameters are then used to specify the structure of the transverse grids for the particles and the radiation. DGRID represents the dimension of the transverse section for the simulation, while NCAR defines the number of points to separate each dimension of the transverse section used to discretize the radiation (an even number guarantees the presence of a central point on the undulator axis).
LBC sets the contour condition used to solve the field (=1 for the Dirichlet condition, otherwise for the Neumann condition).
As regards the longitudinal grid, the parameter DELZ defines the minimum integration step (expressed in terms of the undulator period XLAMD).

C.4.4 Temporal parameters

Time-dependent simulates are enabled by setting the parameter ITDP to one. An important parameter is given by the required number of slices NSLICE, which depends on the time-window of the simulation. Scaling 'time' by the speed of light (s=ct) abd assuming a time-window starting at the tail s_0 and ending at the head s_1 of the beam, the required number of slices is NSLICE=$(s_1 - s_0)$/(ZSEP*XLAMDS) and the first slice has the position s_0 (NTAIL=s_0/(ZSEP*XLAMDS) and it must be $s_0 < s_1$). ZSEP is the separation between two consecutive slices and it has to be a multiple of the integration step DELZ: it is important to note that, for ZSEP larger, the analized spectral window by the simulation is smaller and it is more and more difficult to find the resonance condition (2.1). This last situation gets more complicated at short wavelengths.

The parameter IOTAIL is an indication for GENESIS 1.3 whether radiation is generated outside the time-window, but if only a subsection of the electron beam is simulated it might slip at s_0 into it while the beam propagates. A rather wild guess about the radiation field which slips into the time-window is made, so that the tail part of the time-window is physically incorrect and by setting IOTAIL=0 these slices in the output are excluded. The number of suppressed slices is simply the number of the undulator periods divided by ZSEP.

The CURLEN parameter allows to define the rms length of the electron beam having a Gaussian current distribution, while if CURLEN is null or negative the current distribution is assumed to be uniform.
As an example we can assume a Gaussian beam profile with an rms length of 1mm (CURLEN=0.001) and a radiation wavelength of $5\mu m$ for an undulator with N_w =200 periods and with ZSEP=2. The output should be between -2mm and 2mm, which cuts a part of the bunch out (IOTAIL=0). The total number of simulated slices is 400, plus 100 suppressed slices (NSLICE=500). The first simulated slice is NTAIL=-300 which is equivalent to $s_0 = -3$mm. In the example the time window is very close to the entire beam, and with $s_0 = -3$mm the local beam current amounts to 1% of the peak current: with good approximation, the tail $s < s_0$ will not significantly amplify any radiation and with 100 more slices the entire bunch can be simulated.